Jessica Johnson

Decision Framework for the Design and Construction of Autonomous Artificial Reefs

UNIVERSIDADE DO ALGARVE
FACULDADE DE CIÊNCIAS E TECNOLOGIA
2018

Jessica Johnson

Decision Framework for the Design and Construction of Autonomous Artificial Reefs

Master in Marine and Coastal Sciences

Work performed under the supervision of:
Duarte Duarte - University of Algarve
Eduardo Pereira - University of Minho

UNIVERSIDADE DO ALGARVE
FACULDADE DE CIÊNCIAS E TECNOLOGIA
2018

Declaration

Declaração de autoria de trabalho

Declaro ser a autora deste trabalho, que é original e inédito. Autores e trabalhos consultados estão devidamente citados no texto e constam da listagem de referências incluída.

Jessica Johnson, September 2018

Declaration of authorship of work

I declare to be the author of this [O2] work, which is original and unpublished. Authors and works consulted are duly cited in the text and are included in the list of references.

Jessica Johnson, September 2018

Copyright Notice

Acknowledgements and Dedication

This research would not have been possible without the diligent guidance of my supervisors, Professor Duarte Duarte and Professor Eduardo Pereira. I would also like to thank Professor Manuela Lima and Mr. Rui Oliveira for their support and collaboration in the experimental tests with the Hydraulic Flume. A big thank you to Professor Vitor Cunha, who brought to life the computer designs through 3D printing. Last but not least, I'd like to thank Marisa Pinheiro, Dmytro Maslov and Fabio Cruz for their technical support and patience, dealing with my many questions and requests throughout this process. The corporation between University of Algarve and University of Minho was instrumental in the completion of this research, and I hope that the relationships made over the last year can be continued into the future.

Next, I'd like to thank the many friends I made while studying abroad in Portugal. My university classmates provided immeasurable support and motivation throughout the program. I was fortunate enough to experience two different cities while studying, and the connections I made in both Faro and Guimaraes truly made the experience. I will always cherish the last two years as a very influential part of my life and I look forward to our paths crossing again in the future.

Finally, I would like to dedicate this work to Rens Jonker, whose passion for SCUBA and marine conservation has motivated me to pursue higher education in these fields. His unwavering support throughout this program has allowed me to push beyond what I thought was possible.

Abstract

Keywords: Artificial Reef, Sustainability, Hydraulic Flume, Digital Elevation Model, orthomosaic

This thesis focused on the testing and design of an innovative Artificial Reef geometry, as part of the decision framework for the planning, design, construction, placement and subsequent monitoring of a Modular Artificial Reef (MAR). The MAR will be installed off the west coast of Portugal to promote fish biodiversity, increase biomass and to serve as a SCUBA diving point of interest for tourists. Through physical hydraulic flume testing, the Prototype Modular Artificial Reef (PMAR) underwent environmental scenarios to evaluate the current design. These environmental scenarios were designed to imitate both constant flow and wave energy environments. An Acoustic Doppler Velocimeter (ADV) was used to measure flow velocities both upstream and downstream the PMAR to quantify the impact of the PMAR on water flow. After testing, digital photographs were used to create Digital Elevation Models which were overlaid on the original photographs to create an Orthomosaic image. This orthomosaic illustrated the sediment transportation changes in and around the PMAR throughout various testing scenarios. By studying areas of scour and erosion, it was possible to see the impact of the PMAR on sediment transportation. Through testing, sediment was transported along the water flow direction. Overall erosion and scoring increased when wave energy was added to the system. In general, there was erosion around the front end of the PMAR and deposition around the back end. This led to a sinking effect of the entire PMAR with a slight rotation in the same direction as the water flow. It is recommended that a baseplate be added to the design to ensure stability, minimize sinking and prevent the PMAR from overturning in high energy wave conditions. In addition, further testing with multiple modular pieces linked together is required to ensure that the modular design can withstand these environmental strains.

Resumo

Palavras-chave: Recife Artificial, Sustentabilidade, Canal Hidráulico, Modelo Digital de Elevação, ortomosaico

Esta tese teve como tema a idealização e ensaio de uma geometria inovadora de Recife Artificial, no contexto do desenvolvimento de um modelo de apoio à decisão para o planeamento, projeto, construção, colocação e monitorização subsequente de um Recife Artificial Modular (MAR). O MAR será instalado ao largo da costa oeste de Portugal para promover a biodiversidade de organismos marinhos, aumentar a biomassa e servir de ponto de interesse para o mergulho de mergulho recreativo e científico. Através do ensaio em canal hidráulico, o Protótipo Modular de Recife Artificial (PMRA) foi submetido a cenários ambientais para avaliar o seu comportamento estrutural e hidrodinâmico, assim como o desempenho do seu desenho atual. Esses cenários ambientais de teste foram idealizados para imitar tanto o fluxo constante quanto os ambientes de energia das ondas. Um Velocímetro Doppler Acústico (ADV) foi usado para medir as velocidades de fluxo antes e depois do PMRA para quantificar o seu impacto no fluxo de água. Fotografias digitais pós-teste foram usadas para criar modelos de elevação digital que foram sobrepostos nas fotografias originais para criar uma imagem ortomosaica. Este ortomosaico ilustrou as mudanças no transporte de sedimentos no local e em volta do PMRA ao longo de vários cenários de testes. Ao estudar áreas de deposição e erosão, foi possível estudar o impacto do PMRA no transporte de sedimentos. Os sedimentos foram transportados ao longo da direção do fluxo de água. A erosão geral e a deposição aumentaram quando a energia das ondas foi adicionada ao sistema. Em geral, houve erosão dianteira a montante do PMRA e deposição a jusante. Isso levou a um efeito de afundamento de todo o PMAR com uma ligeira rotação do mesmo na direção do fluxo de água. Recomenda-se adicionar uma placa de base ao conceito inicial para garantir a estabilidade, minimizar o afundamento e evitar que o PMAR seja derrubado em condições de ondas de alta energia. Além disso, são necessários testes adicionais com várias peças modulares ligadas entre si para garantir que o projeto modular possa suportar essas ações ambientais.

Resumo

Esta tese teve como tema a idealização e ensaio de uma geometria inovadora de Recife Artificial, no contexto do desenvolvimento de um modelo de apoio à decisão para o planeamento, projeto, construção, colocação e monitorização subsequente de um Recife Artificial Modular (MAR). O MAR será instalado ao largo da costa oeste de Portugal, dentro do Parque Natural do Litoral Norte (PNLN). O objetivo deste projeto é o de promover a biodiversidade de organismos marinhos, aumentar a biomassa e servir como um ponto de interesse para mergulho de recreio ou científico. O trabalho realizado insere-se no contexto do trabalho em curso no âmbito de dois projetos separados, o NEXT-SEA e o projeto OMARE. O NEXT-SEA é um projecto de investigação financiado pela Universidade do Minho e pela Comissão de Coordenação e Desenvolvimento Regional do Norte de Portugal (CCDNR). O projeto OMARE é patrocinado pelo Município de Esposende, pela Universidade do Minho e pelo Programa Operacional de Sustentabilidade e Uso Eficiente de Recursos (POSEUR). O protótipo finalizado está planeado para instalação em março de 2019.

Através do ensaio em canal hidráulico, o Protótipo Modular de Recife Artificial (PMRA) foi submetido a cenários ambientais para avaliar o seu comportamento estrutural e hidrodinâmico, assim como o desempenho do seu desenho atual. O Canal Hidráulico está localizada no Laboratório de Hidráulica e Recursos Hídricos do Departamento de Engenharia Civil da Universidade do Minho. O canal mede 14 m de comprimento, dos quais 10 m fornecem a área de teste. Esta área de teste tem uma seção transversal com uma largura de 30 cm e uma altura de 45 cm. Dentro desta câmara, uma caixa de areia foi construída medindo 2,5 m de comprimento, 10 cm de altura e com uma largura igual à do canal. Há uma pequena rampa (1,5 m de comprimento) que leva à caixa de areia com um ângulo de 5 ° com a horizontal. A rampa e a plataforma são constituídas por acrílico. O caudal de água de 43,74 m^3/h foi selecionado de modo a refletir as condições mias desfavoráveis estimadas para as zonas entre-marés na costa de Esposende.

Um protótipo em pequena escala do recife artificial modular (PMAR) foi criado usando uma impressora 3D. Este modelo foi impresso em uma escala de 1:20 do desenho final planeado. Usando um Velocímetro Doppler Acústico (ADV), quatro tipos de medidas foram registadas: (i) perfis verticais da velocidade do fluxo sem e (ii) com PMAR instalado, (iii) séries temporais e (iv) perfis horizontais de velocidade do fluxo. O objetivo do estudo foi ilustrar e documentar o efeito que o PMAR tem sobre o movimento de água e sedimentos, para entender seu funcionamento e impacto ambiental uma vez implementado.

Os ensaios foram realizados considerando dois cenários de teste. O primeiro cenário modelou um ambiente de fluxo constante. O segundo cenário modelou um ambiente de alta energia das ondas. Cada cenário exigiu três estágios de teste diferentes, durante os quais os dados foram recolhidos. O primeiro estágio mediu as velocidades de fluxo sem a presença do PMAR. Já com a presença do PMAR no canal de teste, o segundo estágio mediu as velocidades de fluxo a montante do PMAR, e o terceiro estágio mediu as velocidades de fluxo a jusante do PMAR. Cada teste envolveu um tempo de ensaio de, pelo menos, duas horas. Após a conclusão do tempo de ensaio, o tanque era drenado para que a forma final da superfície do fundo de areia pudesse ser documentado, recorrendo a fotogrametria. Deste modo, após a conclusão de cada teste, foi realizado o levantamento fotográfico do fundo recorrendo a fotografias de alta resolução. Estas fotos foram tiradas de uma posição a 90 ° do plano horizontal, 40 cm acima da superfície do fundo de areia. As fotos foram tiradas a cada 5 cm, garantindo pelo menos 60% a 80% de sobreposição entre fotos consecutivas. É importante garantir que cada área surja documentada em pelo menos 3 fotografias consecutivas. Essas fotografias foram posteriormente processadas utilizando o software Photoscan da Agisoft, gerando-se as nuvens de pontos 3D. estes resultados foram utilizados para gerar modelos de elevação digital que foram sobrepostos nas fotografias originais para criar ortomosaicos digitais. Estes modelos ilustraram as mudanças no transporte de sedimentos no interior e ao redor do PMAR em vários cenários de testes.

Após a análise dos modelos obtidos constatou-s que, em geral, o sedimento aparentou ser transportado desde a parte a montante do PMAR e depositado a jusante, resultando num efeito de rotação de corpo rígido do PMAR na direção da ondulação. Este resultado levanta duas questões, que deverão ser clarificadas antes de se proceder à conclusão do desenho dos PMAR. A primeira é se a quantidade de sedimentos transportada seria excessiva, fazendo com que o PMAR afundasse o suficiente para anular os efeitos benéficos da sua instalação. A segunda é se existe um risco significativo de o PMAR derrubar, potencialmente danificando a estrutura ou a flora e a fauna que o rodeiam. Uma solução possível seria instalar uma placa de base na qual a estrutura do PMAR poderia ser construída. Isso eliminaria a erosão e o desgaste nas proximidades da estrutura e minimizaria a possibilidade da ocorrência de derrube.

Além disso, a análise dos Modelos Digitais de Elevação ilustra o efeito resultante de considerar a ação das ondas, quando comparados com os resultados que foram obtidos sem ondas. Nos ensaios que foram realizados com ondas verificou-se que ocorreu maior quantidade de transporte de areia. Além disso, foi demonstrado que maiores amplitudes de onda, ao gerarem mais energia, conduziram a um maior transporte de areia dentro do sistema.

Outros fatores de teste, como saturação de areia, foram destacados a partir da análise desses modelos. Observou-se que quando a areia ficou totalmente saturada durante a noite, a formação das dunas tipicamente resultantes da deposição de sedimentos a jusante da estrutura sofreu alterações com o tempo, não tendo mantido a sua estrutura e geometria tal como se encontravam imediatamente após a conclusão dos ensaios. Nos casos dos ensaios em que foi permitida a secagem da areia, verificou-se que as geometrias e estruturas finais das dunas podiam ser visualizadas claramente e mantinham a sua configuração inicial, mesmo quando fotografadas no dia seguinte.

Em geral, os ensaios realizados permitiram validar e aferir a contribuição que todo o protocolo de ensaio desenvolvido pode dar para o estudo de geometrias inovadoras de recifes artificiais. O fluxo de trabalho desenvolvido durante este projeto pode ser adotado para o desenvolvimento e teste de estruturas de recife artificial similarmente inovadoras, especialmente numa fase inicial do seu desenvolvimento ou quando os testes em campo não são possíveis. Além disso, estes ensaios serviram também para ilustrar o atual impacto do PMAR no transporte de sedimentos em várias condições ambientais. No momento em que haja maior quantidade de dados de campo disponíveis, os protocolos de ensaio podem ser alterados e aprimorados para refletir com maior aproximação o ambiente de instalação. A principal preocupação destacada pelos resultados obtidos envolve a possível rotação e o afundamento do PMAR, o que poderia ser mitigado através do uso de uma placa de base. Testes futuros devem incluir dados de campo atualizados e quaisquer alterações de geometria que atendam a estas questões. Além disso, poderá ser interessante realizar testes adicionais com várias peças modulares ligadas entre si para aferir a capacidade do conceito modular em desenvolvimento para suportar as ações ambientais.

Table of Contents

Index of Figures

.

List of Abbreviations

AR	Artificial Reef
CCDRN	North Portugal Regional Coordination and Development Commission
DEM	Digital Elevation Model
DOM	Digital Orthomosaic Model
EUNIS	European Union Nature Information System
IPCC	Intergovernmental Panel on Climate Change
ISISE	Institute for Sustainability and Innovation in Structural Engineering
MAR	Modular Artificial Reef
NFRM	Natural Frequency Response Monitoring
OMARE	Marine Observatory of Esposende
POSEUR	Program of Operational Sustainability and Resource Efficiency
PMAR	Prototype Modular Artificial Reef
PNLN	Northern Littoral Natural Park
SCUBA	Self Contained Underwater Breathing Apparatus
SHM	Structural Health Monitoring

1. Introduction

The Northern Littoral Natural Park (PNLN), is a national park located on the west coast of Portugal. What were once long sandy beaches of the PNLN have now been reduced to small pebbles due to high energy waves which have caused significant erosion to the beaches (Granja et al., 2015). Additionally, an increase in global temperatures is contributing to the acidification of the ocean, sea level rise, and eutrophication, all of which are leading to mass coral die off (IPCC, 2014). Coral reefs systems are an important part of the oceanic ecosystem as they serve as shelter, food and breeding grounds for a wide variety of organisms, as well as, a way for storm wave energy to dissipate before hitting the coast, preventing erosion and coastal morphodynamic alterations (NOAA, 2017). Rocky bottoms or hard substrates also provide important structure and support to natural habitats. A new challenge will be to find a way to extend or enhance all natural environments to protect against the negative impacts due to climate change.

Fishing is an important industry around the world, especially for the country of Portugal. Trawlers, illegal fishing and destruction of natural reefs has caused an overall decrease in the availability of fish (Reef Resilience Network, 2018). Between the negative environmental impacts of global warming and the stresses placed from overfishing, many of the fish stocks of the world's oceans are being depleted at an unsupported rate (IPCC, 2014).

Through the work of two separate projects, the Institute for Sustainability and Innovation in Structural Engineering (ISISE) of the University of Minho, Department of Civil Engineering, is working to help mitigate these challenges. A team has been assembled to plan, design, construct and evaluate building a modular reef system which could be implemented to promote biodiversity, increase fish biomass and provide a tourist destination for SCUBA divers to explore. This reef will be constructed out of concrete and will have the ability to be built in modular sections to allow expansion and evolution of design.

This Modular Artificial Reef (MAR) is being designed under the research project NEXT-SEA, funded by the University of Minho and North Portugal Regional Coordination and Development Commission (CCDRN). This project has a dual approach to its focus: biological and structural design. Since this design will be used to promote biodiversity and increase biomass, it is important that the reef can provide effective shelter and protection for native species (biological). Secondly, as this reef will be placed off the coast, it is important that the reef is designed to withstand the various environments it could encounter (structural design). It is important that the modular design is robust enough to withstand areas of high current, tidal changes or storm surges.

Once the MAR is designed, the construction and installation will be supported through the Marine Observatory of Esposende (OMARE) project, sponsored by Esposende Municipality, the University of Minho and the Program of Operational Sustainability and Resource Efficiency (POSEUR) for installation within the PNLN. This park has been a protected area since 1987 and was officially designated a national park in 2005 (Visit Esposende, 2018). This national park covers 16 km between the mouth of the Neiva River in the north to the town of Apúlia to the south (Turismo de Portugal, 2013), Figure 1.1.

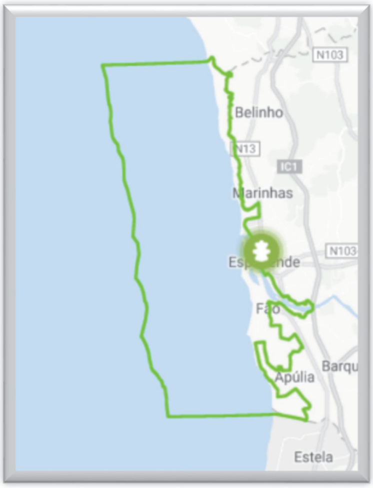

Figure 1.1: Map of the Northern Littoral National Park (PNLN, 2018)

PNLN has vast touristic and commercial value as it is a popular vacation destination, as well as, home to a busy commercial port in Esposende located in the center of the park. Placement of the reef off the coast of Esposende could simultaneously provide the environmental benefits by promoting biodiversity and increasing biomass, as well as, to serve as a point of interest for tourists through fishing and SCUBA diving.

This thesis worked in conjunction with ongoing research to better understand the interactions between the MAR and its environment. The objective was to study a new design concept for MAR by measuring its interactions with water flow and sediment transportation. Through physical hydraulic flume testing, a Prototype Modular Artificial Reef (PMAR) was fabricated and tested using a variety of environmental scenarios. These scenarios were chosen to represent some of the potential environments off the Esposende coast. These tests served as the first physical experimental tests for the PMAR and provided useful feedback to the design and construction of the final MAR to be installed. The first real scale prototype is expected to be ready for installation by March of 2019.

2. Literature Review

Artificial reefs can be made in a variety of different shapes, from mimicking local seafloor structures, to deliberate geometric features aimed at providing a specific benefit such as wave energy dissipation, protection from high currents or tourism attraction such as statues or shipwrecks (Yaakob, 2016). Artificial reefs can also be made of a variety of different materials including, but not limited to: concrete, wood, metal and glass. To date, concrete is the most commonly used material in the construction of artificial reefs (Yaakob, 2016).

This literature review has been divided into three subcategories; which deal with the topics explored in the conducted research: importance of artificial reefs, current research and photogrammetry. Understanding how artificial reefs may contribute in these areas will be crucial in understanding the design and testing of the artificial reef within the scope of this project.

2.1 Importance of Artificial Reefs

2.1.1 Increase Biomass

Within the study of artificial reefs, there is a debate concerning whether these installations actually promote the increase of fish biomass by encouraging production and increased survival rates of organisms, or, do they merely serve to attract organisms which would otherwise be spread throughout the local environment. Some argue that artificial reefs only attract local fish, and therefore can serve as detriment to the environment as the populations are now congregated in a smaller area allowing for increased fishing or predation (Bohnsack,1989). On the other hand, others argue that an important benefit of an artificial reef is its ability to increase fish biomass. They are able to do this by providing a safe shelter for organisms to breed and live. It has been demonstrated that artificial reefs can provide an area of increased survival rates when compared to more open environments (Liu, 2011).

In a study conducted by Cresson et al. (2014) an experiment using isotopic tracers was conducted to provide insight into this debate. In this experiment, samples were taken from species near a series of artificial reefs off the southern coast of France. Here species ranging from primary producers to apex predators were collected. By measuring the isotopic signatures of carbon and nitrogen, the trophic relationship of the environment could be traced and measured. Through this experiment they found similar isotopic signatures throughout the trophic levels, proving that the artificial reef was in fact contributing to the increase in fish biomass, not simply attracting fish from the local environment. Isotopic ratios measures for all fish species, including pelagic piscivores with low site fidelity in reef structure, collected on these particular artificial reefs demonstrated that both primary and secondary production of the artificial reef supported the increase in fish biomass observed since their deployment.

2.1.2 Tourism

Artificial Reefs can create economic value for an area in many ways. If designed to be interesting to divers, these reefs become a SCUBA diving destination in and of themselves. By increasing biomass in an area, this gives divers increased probability of seeing interesting marine life. This increase in biomass can also contribute to an influx of fishing, allowing commercial and recreational fishermen alike to benefit from these reefs. Additionally, these reefs can alter wave patterns and breaking points along a coast allowing surf destinations to be artificially created to further provide an economic incentive to installing a MAR along the coast.

After World War II, the Japanese begun using artificial reefs to improve local fish stocks to increase fish catch. This was later adopted in the Mediterranean in the late 1900s, and now is common practice all around the world (Fabi et al, 2005). In a study conducted in 1987, artificial reefs were used to determine the influence of habitat structure of the fish population to determine the role artificial reefs played in fish recruitment, and habitat enhancement (Bohnsack et al, 1994). Here they found that the artificial reefs experienced fast colonization of many different species and experienced fish and biomass densities higher than neighboring sand or natural reef areas. It was also determined that a major portion of the artificial reef population was considered “economically important”, with a case of few “high economic important” fish traveling through, mostly to use the reef as a location for reproduction and protection during its juvenile stage. Fishermen often seek out artificial reefs as areas of high catch success rate, especially when they’ve experienced less successful fishing rates on natural reefs (Polovina and Sakai, 1989).

SCUBA diving has been increasing in popularity since the mid-1940s, when the first set of recreational diving equipment became available to the general population (Dimmock, 2009). Each year, the number of SCUBA divers continues to expand, leading to increase in environmental pressure on natural coral reefs visited by these divers. As coral reef tourism continues to be in high demand, this increased traffic coupled with inexperienced divers physically damaging the reefs, has led to the world-wide deterioration of popular diving locations (Hawkins et al, 2005). One way to help ease this pressure off the natural reefs is to provide an artificial reef alternative to allow divers to still experience the underwater world without damaging the native reefs.

It has become widely accepted, that the implementation of artificial reefs in areas commonly visited by SCUBA divers is an effective way to divert pressure from that natural reefs to help preserve and encourage coral rehabilitation (Polak & Shashar, 2005). Aside from the previously mentioned environmental benefits afforded by artificial reefs, there is also a significant economic benefit. The allure of particular artificial reefs, such as a ship wreck or underwater museum, can lead to an increase in tourism. In a study conducted in 2013, 200 divers were surveyed, and 96% of the participants stated that they were familiar with the term artificial reef (Kirkbride-Smith et al., 2013). Furthermore, when asked to fill out a questionnaire about their diving experience on artificial reefs, 90% answered that they were either very satisfied (54%) or satisfied (36%), while no divers reported being very dissatisfied. Additionally, divers in this study stated that they enjoyed artificial reefs due to the concentration of marine life and the ability to try something new while SCUBA diving.

Surfing has become an increasingly popular sport, as well, with countries like Portugal reporting a near constant rate of increase over the last 30 years (Bicudo and Horta, 2009). Artificial Reefs have been found to create great standing waves popular among surfers. Although popularity of the sport continues to increase, coastal engineering projects work to lessen wave impact on the coast, leading to an overall decrease in surfing locations around the world (Bicudo and Horta, 2009). Artificial reef projects have had success in recreating these coveted waves in areas such as São Pedro´s beach in Portugal (Bicudo and Horta, 2009), Cables Station in Western Australia (Pattiaratchi, 2003) and Narrowneck Reef in Australia (Jackson et al., 2007). In cases such as Cables Station in Western Australia, an area which had previously been unsurfable, is now providing surfers an average of over 150 days of surfable waves each year (Pattiaratchi, 2003). Engineering these reefs is not an easy task, all environmental factors must be considered to ensure that altering wave break locations and angle of incidence does not negatively impact the surrounding areas. There are cases, such as Bay of Plenty, New Zealand, where dreams of the perfect wave were never realized. In fact, this coastal engineering project has led to the creation of a large scour hole which altered waves and currents, causing an increase in the intensity and frequency of rip currents (Mull, 2014). When designed appropriately, artificial reefs can work to enhance a natural wave, increasing its appeal to surfers. However, hard lessons learned, such as the Bay of Plenty help illustrate how quickly a poorly engineered artificial reef can cause negative impacts and serve as a danger to visitors.

2.2 Current Research

2.2.1 Hydraulic Flume Testing

Hydraulic flume testing allows for environmental scenarios to be recreated in a laboratory space. This becomes important when it is desired for one or more critical variable to be controlled, which might not be possible in situ. In a 2015 study conducted by the Department of Ocean Engineering, of Pukyong National University, Busan, Korea, a hydraulic flume was used to test the resettling rates of sediment around an artificial reef (Ha et al, 2015). In this study, a mesh grid was laid under the artificial reef in an attempt to stabilize the surrounding sediment. It was found, in cases where the grid was in place, less sediment transportation occurred. It is important to minimize erosion and scouring effects of artificial reefs as this can lead to an overall sinking or over turning of the design structure. This study highlighted how variations in the design structural of a reef can lead to significant changes in sediment transportation (Ha et al, 2015).

Another test, conducted in 1994, worked to characterize the local scouring of cylindrical artificial reefs (Kimura, et al., 1994). These tests used a hydraulic flume to characterize the local scour to understand the sinking phenomenon experienced by artificial reefs placed in sandy environments. In this study, two definitions of scour were used, clear water scour, where sediment is removed from the scour hole and is not replaced, and live bed scour, where the sediment is removed and replaced continuously (Chabert and Engedinger, 1956). The channel used was 10 m long, 0.7 m wide, and 0.9 m deep and the sand grain size of 0.035 mm. Throughout the testing, scouring was experienced, causing the artificial reef to slide into the hole which led to an overall sinking and rotation of the structure. They also noted the formation of a sand dune which was created behind the structure. This study established a relationship between scour hole depth and water flow velocities, where faster velocities led to deeper scour hole depths. Furthermore, in a different study, it was found that the shape and material of the artificial reef reflected different sinking rates, with cylindrical reefs sinking at a faster rate than a cubic block reef (Sunthong, 1988).

2.2.2 Structural Health Monitoring of Artificial Reefs

Understanding the hydrodynamics around an artificial reef is an important factor when considering an appropriate design. In particular, when geometrical complexity and shape bio mimicking are to be integrated in the reef concept, the level of structural demand is high and structural design needs to be carefully conducted. Firstly, it is important to understand the stresses and strains which will be applied to the reef during extreme events. If allowed to reach a critical value, these stresses could contribute to the physical failure of the reef, and could ultimately lead to structural damages. In a previous study conducted by Liu (2009), a variety of different artificial reef shapes were tested using a combination of numerical models and wind tunnel experiments. In this study, the authors tested the flow fields around many common shapes found within artificial reefs such as cubes, pyramids and tunnels. In their follow-on research in 2011, they found that artificial reef shape, especially height, played an important role in flow dynamics and habitat suitability within the reef. Along with size and shape, other factors can contribute to the hydrodynamic stresses observed in the artificial reefs (Liu et al, 2011). These factors include surface roughness, relative angle to flow, and water flow velocity.

In a study conducted by Yaakob et al. (2016), engineers worked to understand the differences in shear stress of a traditional hollow cube artificial reefs and a newly developed and streamlined "helmet-shaped" design which included rounded edges to increase its hydrodynamic properties. Here they found that a design which incorporated more rounded edges experienced lower wave, inertial and drag forces than the more traditional cubic design. An image of this can be seen in Figure 2.1. An artificial reef with low flow dynamics would improve fish and marine organism's ability to shelter, reproduce and even hunt in and around the artificial reef (Yaakob, 2016).

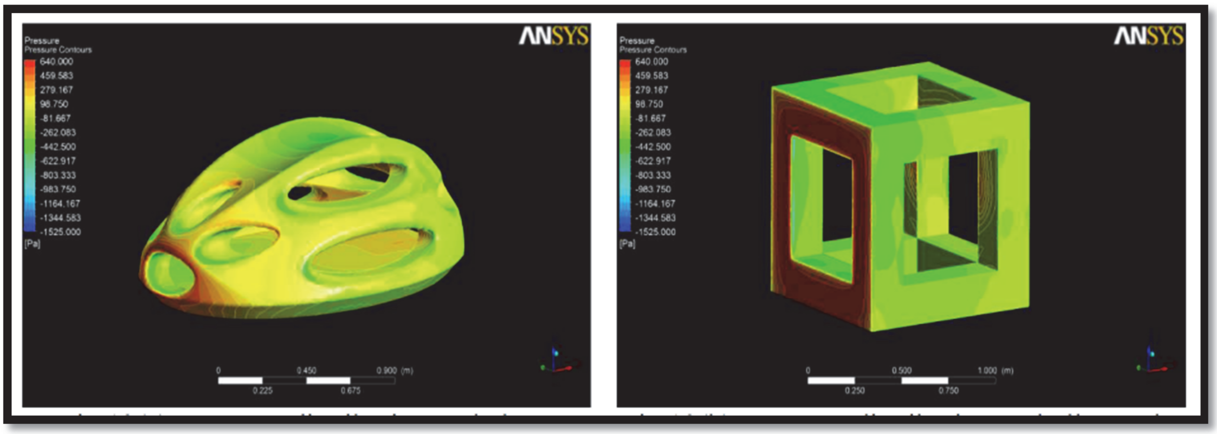

Figure 2.1: Pressure distribution of artificial reef for a flow direction of 0 degrees (Yaakob, 2016).

2.3 Photogrammetry

Photogrammetry is a technique which uses dense overlapping photographs of 3dimensional geometric objects to generate detailed digital renderings (SBL, 2015). Using photographs taken from at least two different angles, data can be mathematically reproduced to generate a 3D image. The use of photogrammetry is especially useful when an object is difficult to measure or access. This process provides an alternative technique to manual processes and allows large quantities of information to be obtained quickly. Furthermore, it allows accurate records of objects shapes, irregularities and imperfections which arise during construction and installation (Dezen-Kempter et al., 2015). Using photogrammetry to solve spatial position problems requires the use of various different mathematical functions, the shape of which must reflect the nature of the observations of both the flat (2D) and the threedimensional (3D) images. Therefore, concepts such as triangulation, rotation matrix and collinearity equations must be carefully considered when rendering the 3D image (Geospatial Services, 2015).

There are two types of photogrammetry, metric and interpretive. Metric photogrammetry involves measuring the images and other sources of information to determine the relative position of points which results in the calculation of distances, angles, areas and volumes of objects. Interpretative photogrammetry allows the recognition and identification of objects based on physical characteristics such as size, shape, shadow to add value to the information presented in a photograph (Geospatial Services, 2015).

Photogrammetry has become an increasingly popular way to generate 3D images and contour maps of areas which would otherwise be difficult to measure. In a 2018 study conducted off the coast of Miami, USA, a researcher used a library of photographs along with Agisoft's software to generate 3D maps of six different natural and artificial reefs to document the differences in complexity and to work to quantify differences in reef recruitment (Johnson-Sapp, 2018). Through photogrammetry, researchers were able to use high resolution photographs to generate 3D models which were used to demonstrate successful and unsuccessful recruitment sites on both types of reefs.

In another study, photogrammetry was used to establish a relationship between fish population and reef structure. Using 3D imagery, data was collected concerning three factors; visual exposure to competitors and predators, density of safe areas to hide from predators and substrate-related food availability (González-Rivero et al, 2017). Fish surveys were conducted concerning three species of territorial damselfish, and by comparing resident fish populations against the three physical factors, connections could be made concerning controlling factors of these population densities. This is considered an improvement over a previous method, known as the rugosity index (González-Rivero et al, 2017).

In one final example, photogrammetry is also being used to monitor an ecological restoration project off the south coast of France in Cortiou Calanque. The Marseille sewage treatment plan has caused significant environmental issues which have led to a significant loss of marine life off the coast. REXCOR is an engineering project, involving the use of artificial reefs to try to rehabilitate local biodiversity and biomass. This project uses photogrammetry to monitor changes as a way to show changes over time (Bianchimani, 2017).

3. Methods

3.1 Testing Equipment

To better understand the hydrodynamic effects associated with the Prototype Modular Artificial Reef (PMAR) a series of tests were run in a hydraulic flume. This flume is located in the Laboratory of Hydraulics and Water Resources of the University of Minho's Department of Civil Engineering. The flume measures 14 m in length, of which 10 m provides the testing area. This testing area has a cross section with a width of 30 cm and a height of 45 cm. The longitudinal slope varies between -1/200 and 1/50. The channel allows the transport of a maximum water flow of 150 m^3/h, monitored through a magnetic flow meter (resolution class: 0.3). Within this flume, a sandbox was constructed measuring 2.5 m long, 10 cm tall and with a width equal to that of the channel. There is a small ramp (1.5 m long) leading up to the sandbox at an angle of 5° to the horizontal. The ramp and platform are made of acrylic glass. Figures 3.1 and 3.2 represents a diagram of the hydraulic flume (not to scale) and a photograph of the same flume.

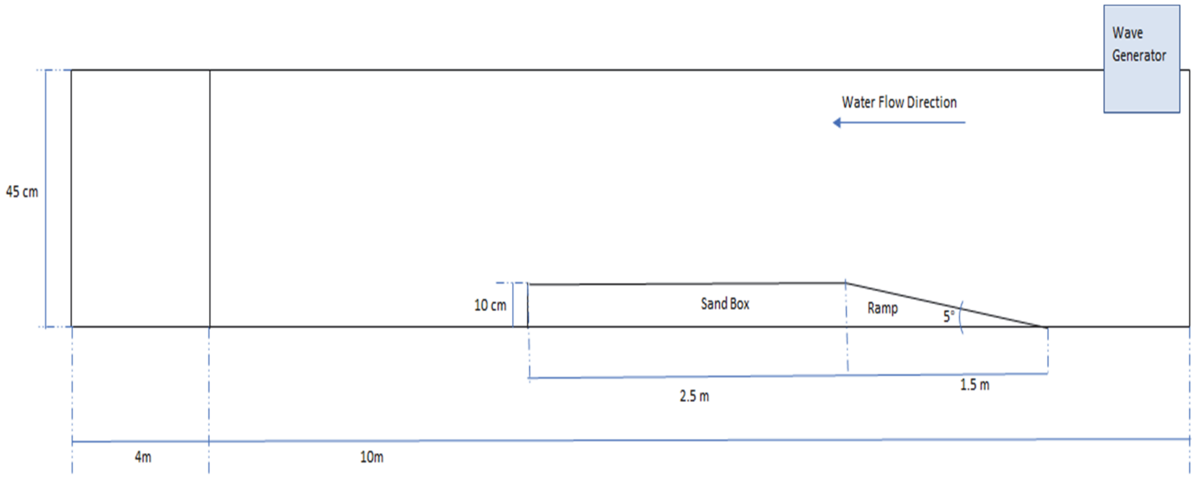

Figure 3.1: Representative diagram of hydraulic flume (not to scale)

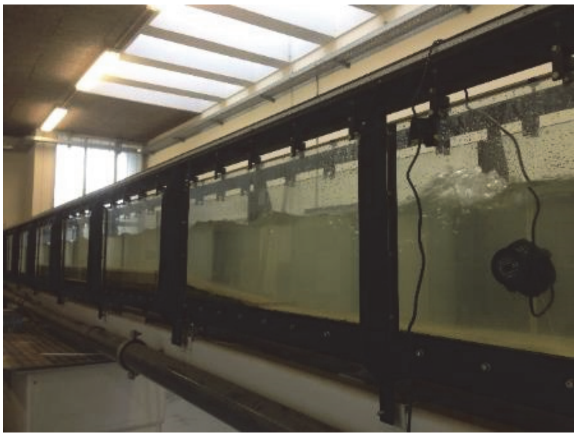

Figure 3.2: Photograph of Testing Flume

The vertical and horizontal flow velocity profiles were taken using an Acoustic Doppler Velocimeter (ADV) by Sontek Triton. To determine the minimum distance from the sampling volume to the interface of the ADV a beam check operation was conducted. Through these checks, it was determined that this particular ADV should be used avoiding to be closer from interfaces than 4 cm. Additionally, the ADV had a blind zone of 10 cm, which was taken into consideration during testing.

A small-scale printed prototype of the modular artificial reef (PMAR) was created using a 3D printer. The prototype was designed using the computer program Rhino, and manufactured using a Creality 3D printer. With a layer size of 0.15 mm, each unit was built using a PLA (poly lactic acid) filament, which is a biodegradable plastic commonly used in this capacity (Ramon, 2013). The model was built to a ratio of 1:20 to the final planned design. Due to concerns the material would be too buoyant, thin pieces of metal were inserted after production to increase its weight, this can be seen in Figure 3.3.

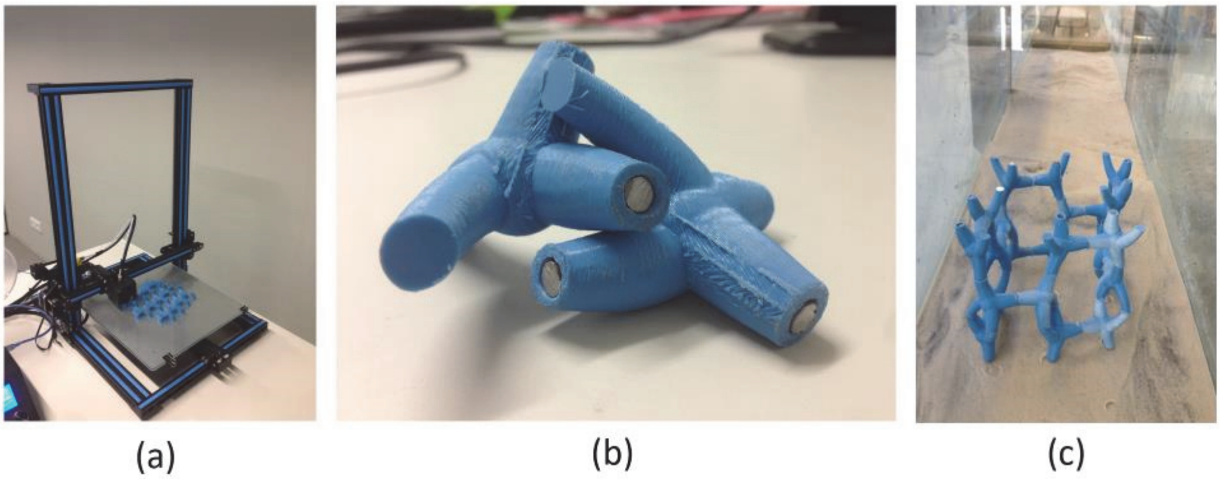

Figure 3.3: Photos of (a) 3D printer (b) individual prototype piece (c) assembled prototype of PMAR

Ideally, the grain size used during testing would be selected to reflect the natural grain size associated to the environment. Due to material availability and physical limitations of the testing facilities, the grain size used during testing was the available one which had an average diameter of 0.328 mm. The impacts of this will be discussed later.

Water depth and flow velocity were selected in a way to most closely resemble actual environmental conditions while staying within the physical limitations of the testing facility. A water depth of 25 cm was selected in order to allow complete submersion of the PMAR during high wave conditions. Next, water flow velocity was calculated using the formula to maximum average velocity without contributing to sand erosion, Richardson and Davis (2001):

$$U_c = \frac{\sqrt{\Psi_c \times (s-1) \times D_{50} \times h^{\frac{1}{3}}}}{0.041 \times {D_{50}}^{\frac{1}{6}}}$$

Where U_c represents maximum average velocity, ψ_c is the shields coefficient, s is the density of the bottom material, h is the water flow height, D_{50} average sediment diameter. Furthermore, localized erosion occurs in the presence of an obstacle for $U / U_c > 0.5$, and for $U / U_c > 0.9$ generalized erosion occurs and the obstacle effect is camouflaged by a layer of sand trying to move naturally. A U / U_c of 0.6 was selected to reflect intertidal current regions off the coast of Esposende, this accounts for a volumetric flow rate of 43.74 m^3/h. A full table with these calculations has been provided in Table 3.1.

Table 3.1: Hydraulic variables used throughout testing

U/UC	U (m/s)	h (cm)	Q (m^3/s)	Q (m^3/h)
0.9	0.243	5	0.00365	13.122
		10	0.00729	26.244
		15	0.01094	39.366
		20	0.01458	52.488
		25	0.01823	65.61
		30	0.02187	78.732
0.5	0.135	5	0.00203	7.29
		10	0.00405	14.58
		15	0.00608	21.87
		20	0.00810	29.16
		25	0.01013	36.45
		30	0.01215	43.74
0.6	0.162	5	0.00243	8.748
		10	0.00486	17.496
		15	0.00729	26.244
		20	0.00972	34.992
		25	0.01215	43.74
		30	0.01458	52.488

The waves were initially generated using an IKA® dual-speed mixer, and later using a flap paddle with the rotating axis fixed at 1/3 of the water column height. The waves were set an wave amplitude to minimize destructive interference along the side of the chamber. An amplitude of 2.8 cm was used for the first test, and 6.3 cm used for the three following wave tests.

3.2 Testing Procedures

The hydraulic chamber was filled to a water depth of 25 cm above the sandbox where the PMAR will be placed. Once water depth reached steady state, a water volumetric flow rate of 43.74 m^3/h was maintained. A series of eight tests were run to measure both vertical and horizontal water velocities in three dimensions.

During each of these eight tests, one of two scenarios were used. The first scenario modeled a constant flow environment. The second scenario modeled a high wave energy environment. Each scenario required three different testing stages where data was collected. The first stage measured the flow velocities without the PMAR. The second stage measured flow velocities upstream of the PMAR. The third stage measured flow velocities downstream of the PMAR. A single test consisted of one scenario and three stages. Figure 3.4 illustrates the testing breakdown structure.

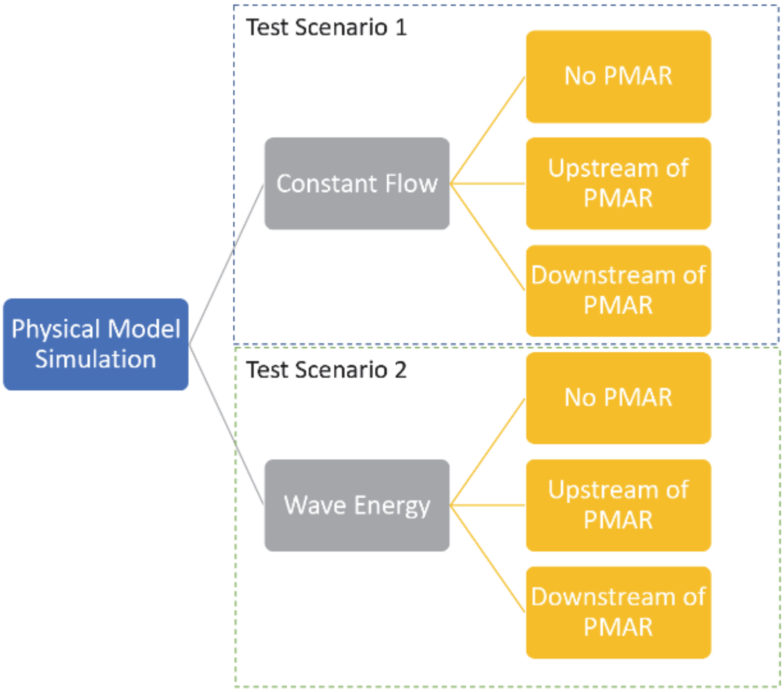

Figure 3.4: Visualization of testing breakdown structure

ADV testing locations for each of the tests can be seen in Figures 3.5. Figure 3.5a represents the testing configuration without the PMAR. Figures 3.5b and 3.5c show the vertical profile testing configuration both upstream and downstream from the PMAR. In all three configurations that ADV is attached to an ADV sensor rod, which is then attached to the hydraulic flume structure through the ADV sensor stand.

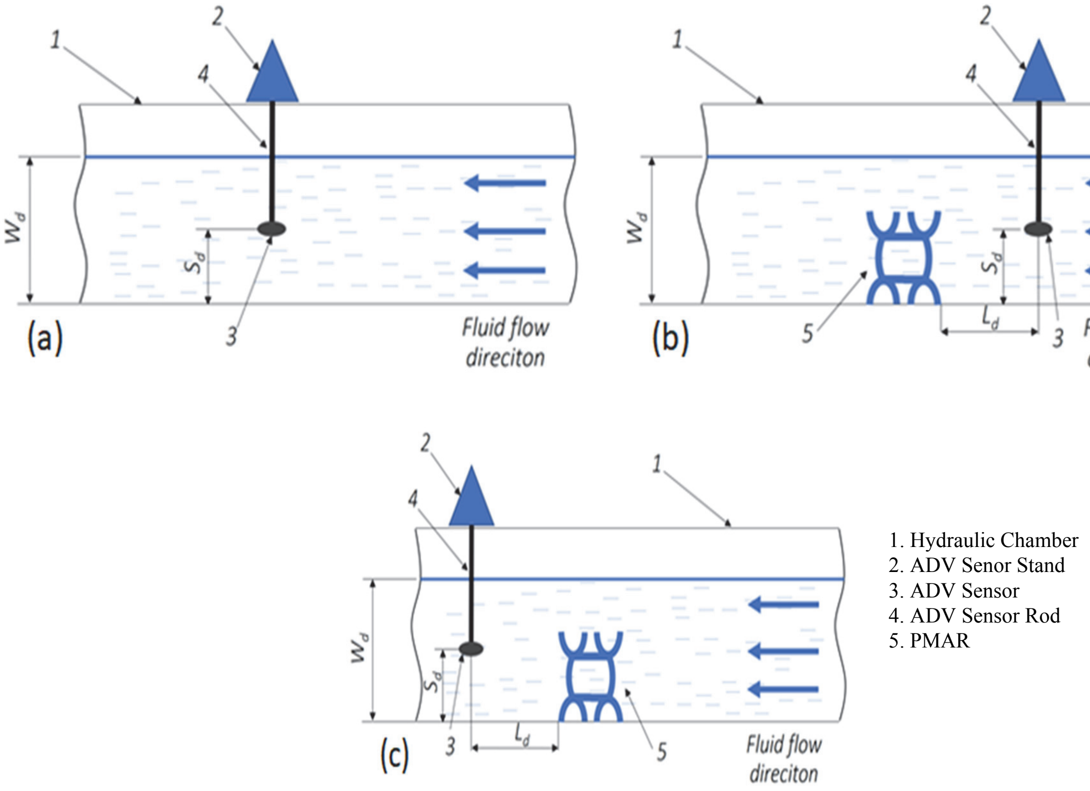

1. Hydraulic Chamber
2. ADV Senor Stand
3. ADV Sensor
4. ADV Sensor Rod
5. PMAR

Figure 3.5: ADV testing locations for the three stages of testing without the PMAR (a), before PMAR (b), after PMAR (c) .

To serve as a reference, the testing area within the sandbox was marked every 10 cm with a reference number. These reference numbers will be used throughout the results to establish positioning of ADV. Each of these position numbers therefore represented 10 cm, an object placed at marker 9 would be 90 cm from the start of the sandbox.

Testing depth locations for each of the tests can be seen in Figures 3.6. The ADV had a blind zone of 10 cm which accounts for the length of the sensor, therefore, no data was collected within 10 cm from the water's surface. The vertical profiles were taken at a depth of 5cm and 15cm, measured from the bottom. The horizontal profiles were taken at a depth of 10cm from the bottom. Furthermore, each of these profiles were taken from two locations. First location measured the water velocity in both the horizontal and vertical planes of the flow channel (without interference of the PMAR) at location 9. The second location measured the velocity of both the horizontal and vertical planes of the upwelling and downwelling zones in the presence of the PMAR, at location 17.

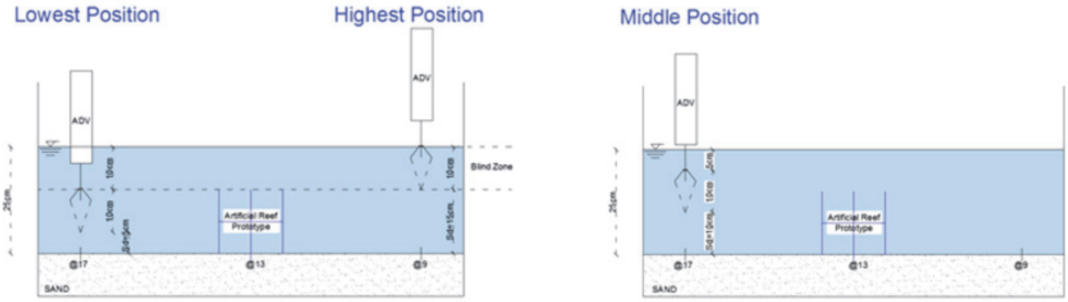

Figure 3.6: Extreme Positions (left) and Middle positions (right) for vertical testing locations

For each test, once the flow reached a steady state, vertical or horizontal flow velocities were measured without the influence of the PMAR. After this data was collected, the system was left to run for a minimum of two hours with the PMAR in place. The specific time for each test can be seen in Table 4.1. After the completion of the test, the vertical and horizontal flow velocities were measured again, both upstream and downstream from the PMAR.

During stage 1 the PMAR was removed. The ADV was installed on the pole on the rack of the hydraulic chamber. The measurement sensor was submerged to the depth (S_d) of 4 cm at a distance from the PMAR installation point (L_d) of 30cm. The ADV collected data at a sampling rate of 3 seconds for 5 minutes. After 5 minutes, the sensor was raised an additional 1 cm until a depth of 15 cm, from the bottom, was reached. This data was recorded on the data logger and downloaded onto a computer for interpretation.

During stage 2, PMAR was put into place, and measurements were taken upstream from the PMAR. The tests were run for a minimum of two hours to allow time for erosion/scouring to occur. For these tests, the ADV was placed at marker 9 at a depth (S_d) of 10 cm. The velocity profile was measured at a fixed point to serve as the control data. The procedures for stage 1 were repeated.

Stage 3 measurements were taken downstream from the PMAR, from position 17 (L_d) of 30cm. The procedures were then repeated as they were in stage 1.

3.3 Photogrammetric Survey

Upon the completion of each test, a series of high-resolution photographs were taken that ran the span of the hydraulic chamber. These photos were taken from a position 90° from the horizontal plane 40 cm above the sand. These photos were then loaded into Agisoft's Photoscan software and 3D images were generated.

To ensure high quality images were collected it was imperative that the photos be captured in high resolution. Through this process, it was important to minimize movements or vibrations in the lab, as any movement captured could cause distortions in the reconstructed model. The photos were taken every 5 cm, ensuring at least 60-80% overlap between consecutive pictures. It was important to capture each area at least three times in different photographs.

Control points were places along the testing area to serve as reference locations used when reconstructing the 3D image. The higher number of control points used, the more accurate the final product would be. For this system, reference tape was placed every 10 cm along the outside of the glass, additionally, specific points along the PMAR were used when applicable.

A small camera stand was constructed to allow a Nikon D800E, 36.3 MP resolution, camera to glide along the top of the hydraulic chamber. An ISO250 and TIF format were chosen to maximize resolution while using Agisoft's Photoscan® software. This software compares all the features of the photographs and generates a 3D model in the form of a point cloud or three-dimensional mesh (Agisoft LLC, 2011). From this point cloud a 3D model with sand texture, a digital elevation model (DEM), orthomosaic model, and general contour map with an equidistance between lines equal to 0.002 m were created. These models could be overlaid on the photographs to generate an orthomosaic image of resulting sediment patterns after each of the tests were run.

4. Results

During testing, four types of measurements were taken: (i) vertical flow velocity profiles without and (ii) with PMAR in place, (iii) time series and (iv) horizontal flow velocity profiles. For each measurement, the ADV recorded several types of files. Each file was labeled “VPAnnn”, where nnn is the specific number for each file. Next to each file name, the position and purpose of the test is listed. For the purpose (V) indicates a vertical profile, (H) indicates a horizontal profile and (TS) indicates this test was used to establish a time series, Table 4.1. It should be noted that all depths are measured from the bottom of the tank upwards. This allowed consistency in measurements even in high wave energy environments.

Table 4.1: Summary of all completed tests

Test	Conditions	VPAxxx File - Position - Purpose
Test 1	Average Volumetric Flow Rate = 43.74m3/h	VPA030@17 (V) VPA032 @9 (V) VPA033 @17 (TS VPA034 @17 (V) VPA034 @9 (V)
Test 2	Average Volumetric Flow Rate = 43.74 m^3/h Average Wave Amplitude: 2.8 cm Test duration: 1h36min	VPA036@17 (V) VPA037@17(TS) VPA038@17 (V)
Test 3	Average Volumetric Flow Rate = 43.74 m^3/h Test duration 4h2min	VPA039@17 (V) VPA041@9 (V) VPA043@17(TS) VPA044@17 (V) VPA045@9 (V)
Test 4	Average Volumetric Flow Rate = 43.74 m^3/h Average Wave Amplitude = 6.3 cm Test Duration: 3h52min	VPA048@17 (V) VPA049@9 (V) VPA050@17 (TS) VPA051@17 (V) VPA052@9 (V)
Test 5	Average Volumetric Flow Rate = 43.74 m^3/h Average Wave Amplitude = 6.3 cm Test Duration: 2h47min	VPA057@17 (V) VPA058@9 (V) VPA059@17 (TS)
Test 6	Average Volumetric Flow Rate = 43.74 m^3/h Test Duration: 4h40min	VPA061@17 (V) VPA062 (H)
Test 7	Average Volumetric Flow Rate = 43.74 m^3/h Average Wave Amplitude = 6.3 cm Test Duration: 4h	VPA064@17 (TS) VPA065@17 (V) VPA066@9 (V)
Test 8	Average Volumetric Flow Rate = 43.74 m^3/h	VPA068@17 (TS) VPA069 (H) VPA070@17 (V) VPA071@9 (V) VPA072@13(V) VPA073@12 (V) VPA074@14 (V) VPA075@19 (V)

4.1 Velocity Profiles

4.1.1 Measurements without PMAR

The results in this section represent reference conditions with and without waves without the PMAR in place. In each test, a volumetric flow rate of 43.74 m^3/h was used. For all tests, measurements were taken from position 17 or 9, which corresponds to 30 cm behind or in front of the proposed PMAR location respectively. Figure 4.1 represents the testing set up.

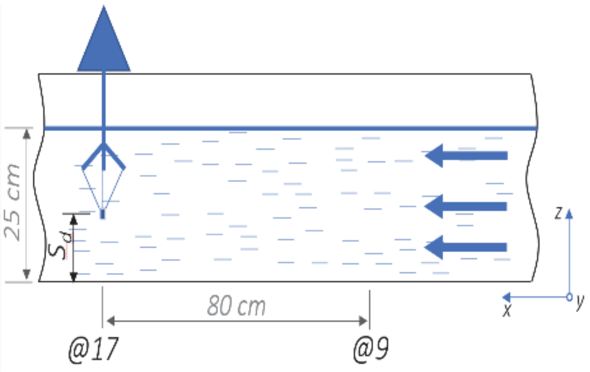

Figure 4.1: Testing set up without PMAR

The results in this section correspond to tests VPA032 and VPA041, tests 1 and 3 respectively. For these tests, the water flow was held constant, and **no waves** were present. Measurements were taken from depths varying between 4 and 11 cm from the bottom. The ADV was placed in **position 9,** which is 30 cm in front of the proposed PMAR location. The results can be seen in Figures 4.2 and 4.3.

It is important to remark that preliminary tests have been conducted to define what was the minimum working distance between the ADV sampling point and the bottom, in order to avoid interference in the measurements. These tests have shown that the distance of 4 cm from the bottom was the minimum to guarantee low interference of the bottom with the measurements. However it should be remarked that only at 5 cm distance from the bottom it was always possible to obtain consistent measurements. However the 4 cm measurements were also shown for all tests, for reference (although these should be cautiously analysed).

For both cases, velocity in the x-direction was maintained at around 18 cm/s with a slight decrease to around 17 cm/s near the bottom. Velocities in the y-direction were fairly consistent, around 1 cm/s with a slight decrease near the bottom. In both cases there was a very slight velocity increase between 5-6 cm in depth. The z-direction velocities in VPA032 were very low, and reached a negative value around 8 cm depth, and slightly increased near the bottom. The z-direction velocities in VPA041 were held steady at around 0.4 cm/s and decreased to 0 at the bottom.

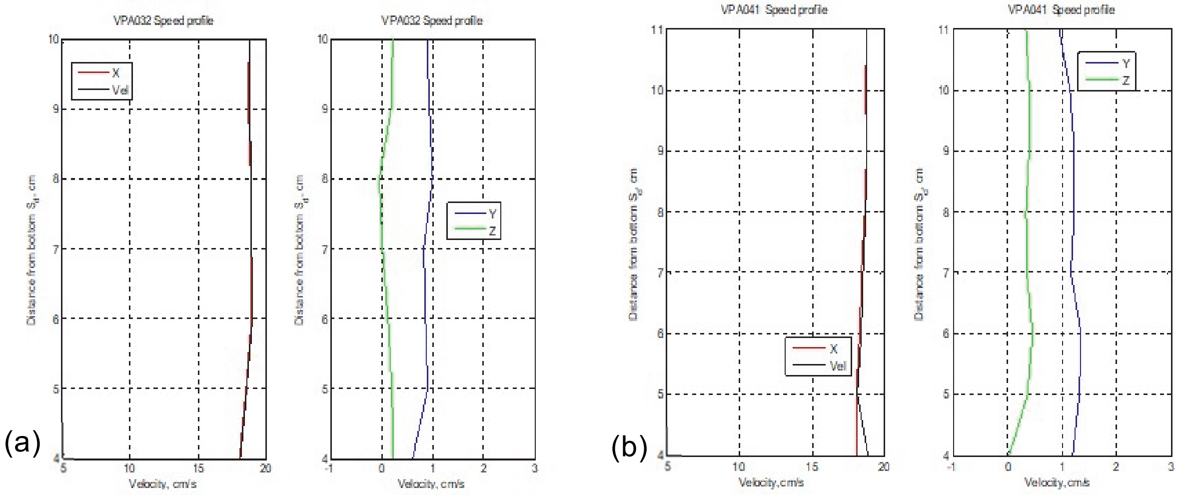

Figure 4.2: Velocity profiles in the x, y and z directions for VPA032 (a), VPA041(b) from position 9.

The statistical data concerning deviation from the mean and coefficient of variation can be seen in Figure 4.3.

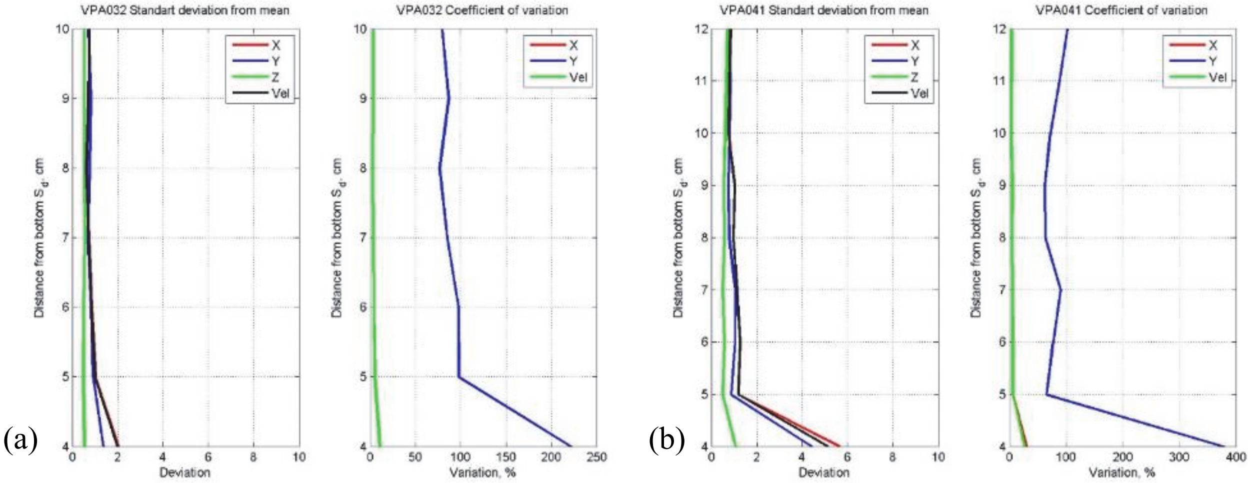

Figure 4.3: Statistical data for VPA032 (a), VPA041(b) from position 9

Next, measurements were taken with the addition of **waves**. For each test, a vertical profile was measured with the ADV depth varying between 4 and 11 cm from the bottom. The results have shown that the minimum distance was 4 cm, however fully consistent measurements were obtained in all cases starting at a distance 5 cm. The ADV was placed at **position 9**. Figure 4.4 concerned tests VPA049 and VPA058 which correspond to tests 4 and 5 respectively. For these tests, an average wave amplitude of 6.3 cm was used. The results can be seen in Figures 4.4 and 4.5.

X-direction flow velocities for VPA049 were maintained around 17 cm/s at every depth. VPA058 experiences similar x-direction velocities until a depth of 5 cm, at which point velocities linearly decreased to 5 cm/s near the bottom (however these results should be analysed with caution, due to bottom interference). Y-direction flow velocities were fairly consistent for VPA049, being just under 1 cm/s. In VPA058, the y-direction velocities were also just under 1 cm/s until a depth of 5 cm at which point decreased linearly to 0 near the bottom. Z-direction velocities for VPA049 were slightly positive reaching a max velocity of around 0.5 cm/s at a depth of 8 cm. For VPA058, the z-direction velocities started off slightly negative until reaching a peak just above zero at 9 cm depth and then quickly decreasing to -0.5 cm/s between the depths of 5 cm and the bottom.

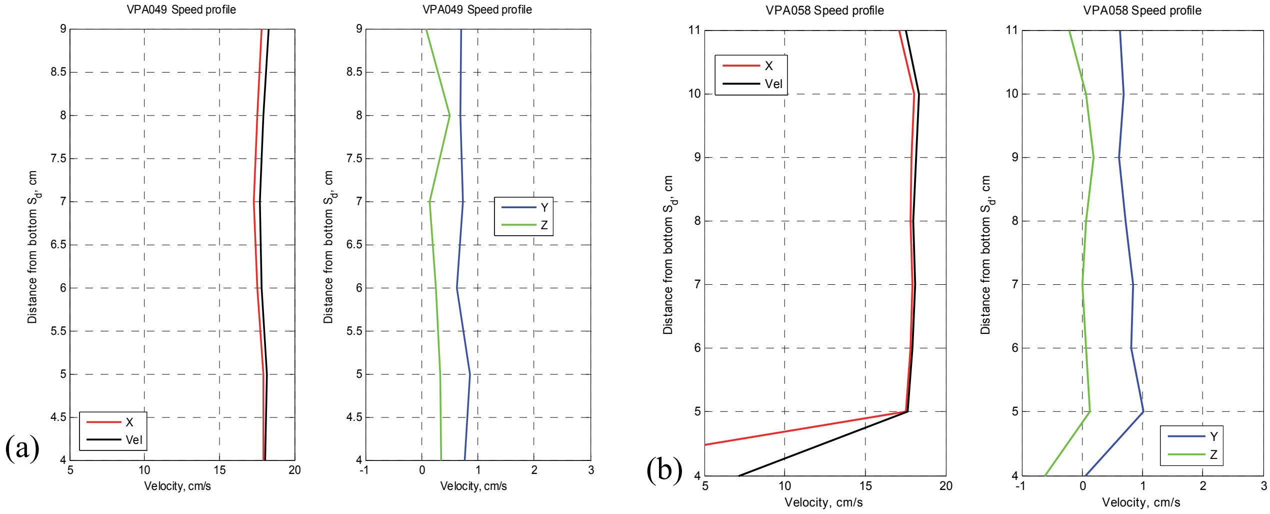

Figure 4.4: Velocity profiles in the x, y and z directions for VPA049(a), VPA058(b) tests from position 9.

The statistical data concerning deviation from the mean and coefficient of variation can be seen in Figure 4.5.

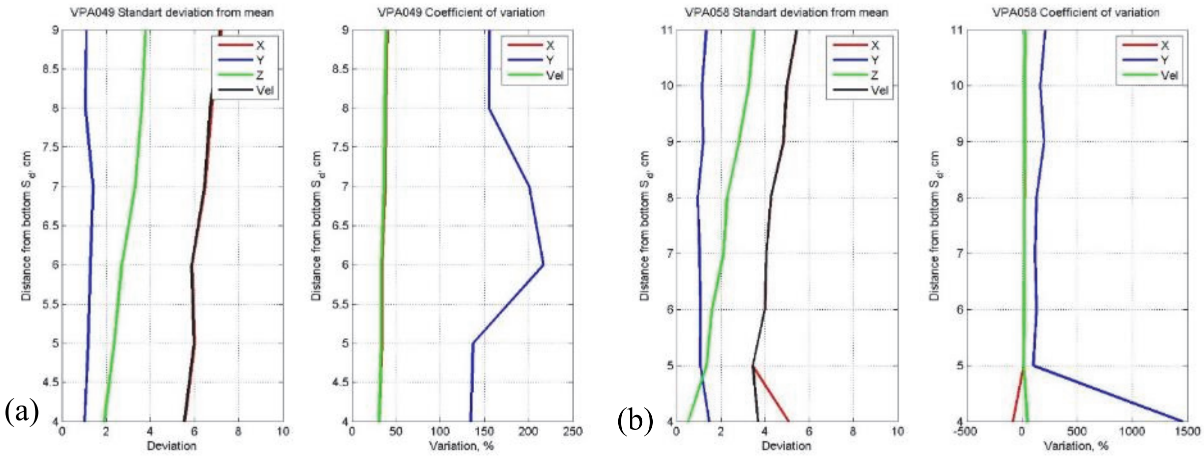

Figure 4.5 : Statistical data for tests VPA049 (a) and VPA058 (b)

The data in Figure 4.6 contain the results for the constant flow, **no wave,** no PMAR scenario. For each test, the ADV depth varied between 4 and 12 cm from the bottom to collect a vertical profile. The ADV was placed at **position 17**. There were two tests that were conducted with these parameters. The tests were VPA030 and VPA039 which corresponds to the first and third tests respectively. The results can be seen in Figures 4.6 and 4.7.

X-direction velocities for both tests ranged from around 19 cm/s to 17 cm/s showing a steady decrease in velocities with depth. Y-direction velocities for both tests hovered around 1 cm/s. Z-direction flow measured just slight above zero, and in the case of VPA039, registered as a negative flow at the very bottom.

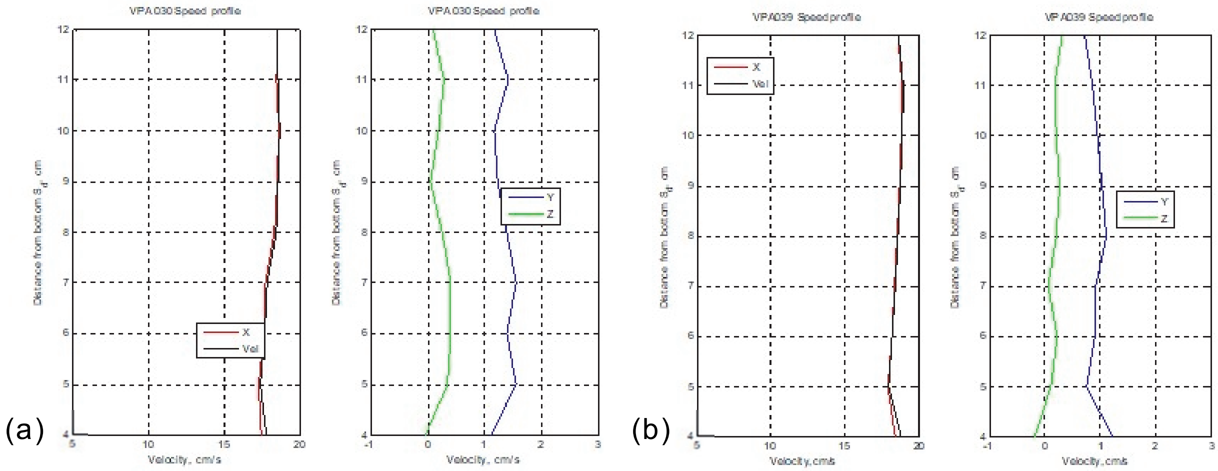

Figure 4.6: Velocity profiles in the x, y and z directions for VPA030 (a) and VPA039 (b) tests, position 17

The statistical data concerning deviation from the mean and coefficient of variation can be seen in Figure 4.7.

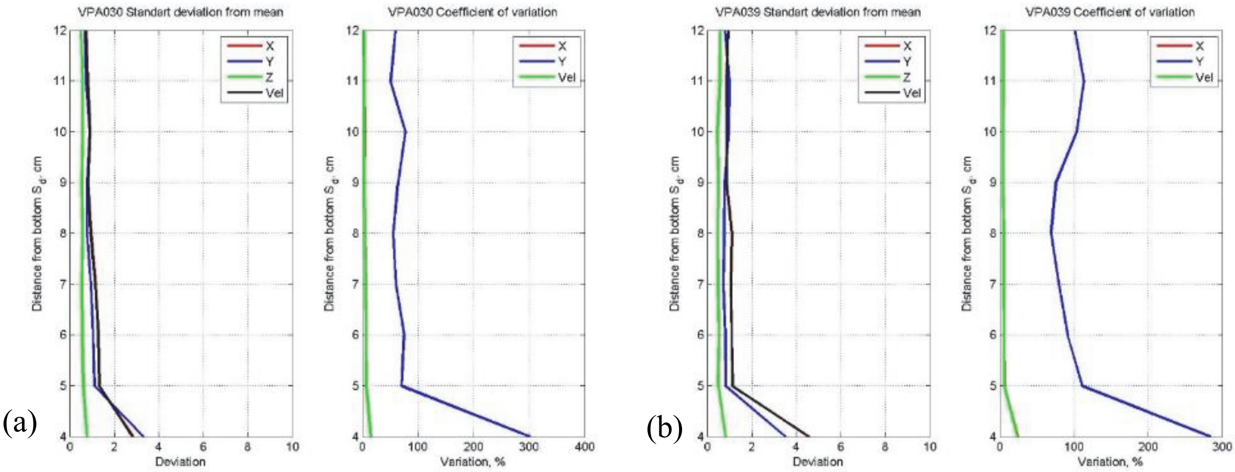

Figure 4.7: Statistical data from VPA030(a) and VPA039(b)

Next, measurements were taken with the addition of **waves**. For each test, a vertical profile was taken with the ADV depth varying between 4 and 11 cm from the bottom. The ADV was placed at **position 17**. The results seen in Figure 4.8 concerned tests VPA036, VPA048 and VPA057 which correspond to tests 2, 4 and 5 respectively. For these tests, an average wave amplitude of 6.3 cm was used, except for test 2, which used a wave amplitude of 2.8 cm. The results can be seen in Figures 4.8 and 4.9.

The x-direction velocities were maintained fairly consistently at 17 cm/s for all tests. For VPA036, x-direction velocity was maintained at about 17 cm/s across all depths, slightly decreasing with depth. In the case of VPA057, there was a slight velocity increase to 20 cm/s near the bottom. The y-direction velocities for VPA036 and VPA048 showed a very slight increase with depth, having a maximum velocity right near the bottom. In VPA057, y-direction velocities showed a slight decrease with depth, until 5 cm, at which point the velocities started increasing from about 1 cm/s to 2.5 cm/s near the bottom. Z-direction velocities were about 0 for all tests, although they were slightly positive in the cases of VPA036 and VPA048 and slightly negative for VPA057.

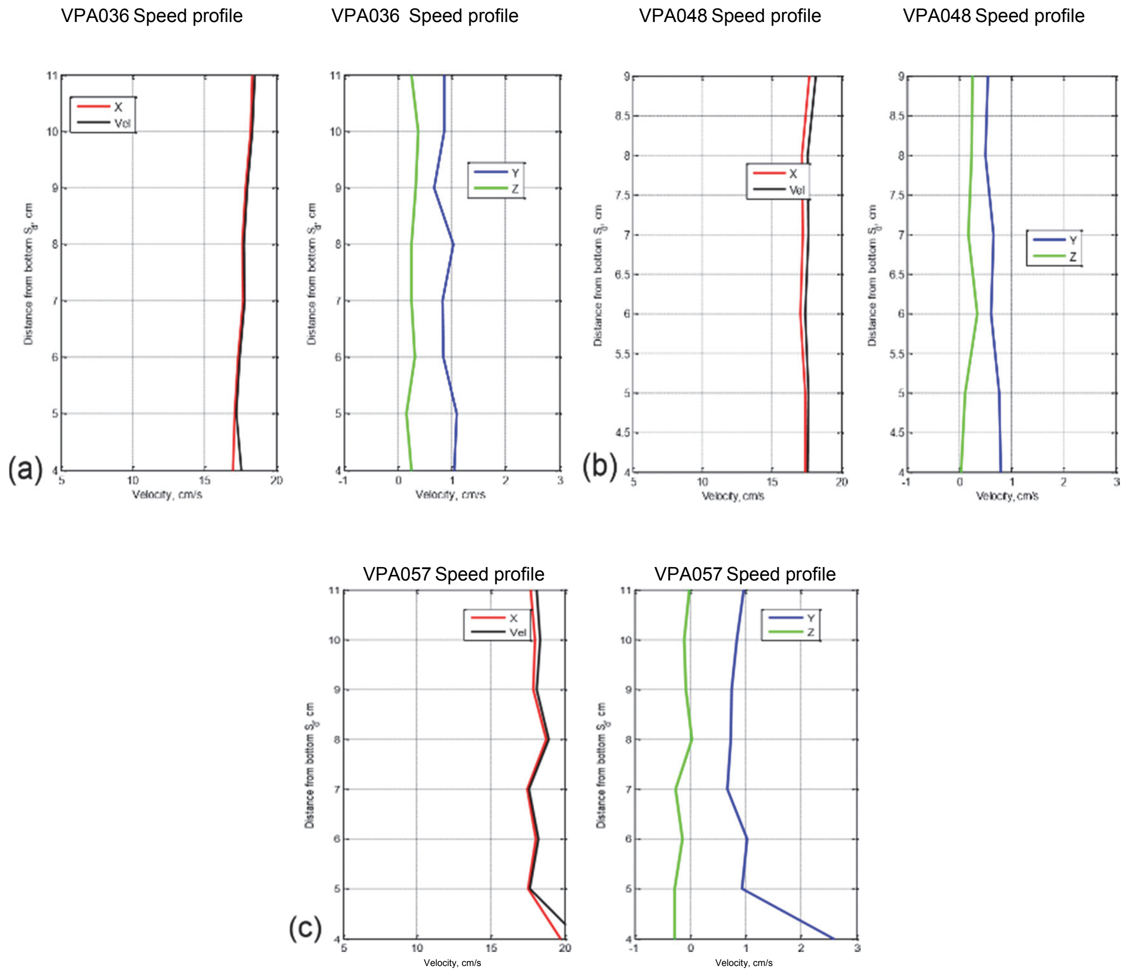

Figure 4.8: Velocity profiles in the x, y and z directions for VPA036(a), VPA048(b) and VPA057(c) from position 17

The statistical data concerning deviation from the mean and coefficient of variantion can be seen in Figure 4.9.

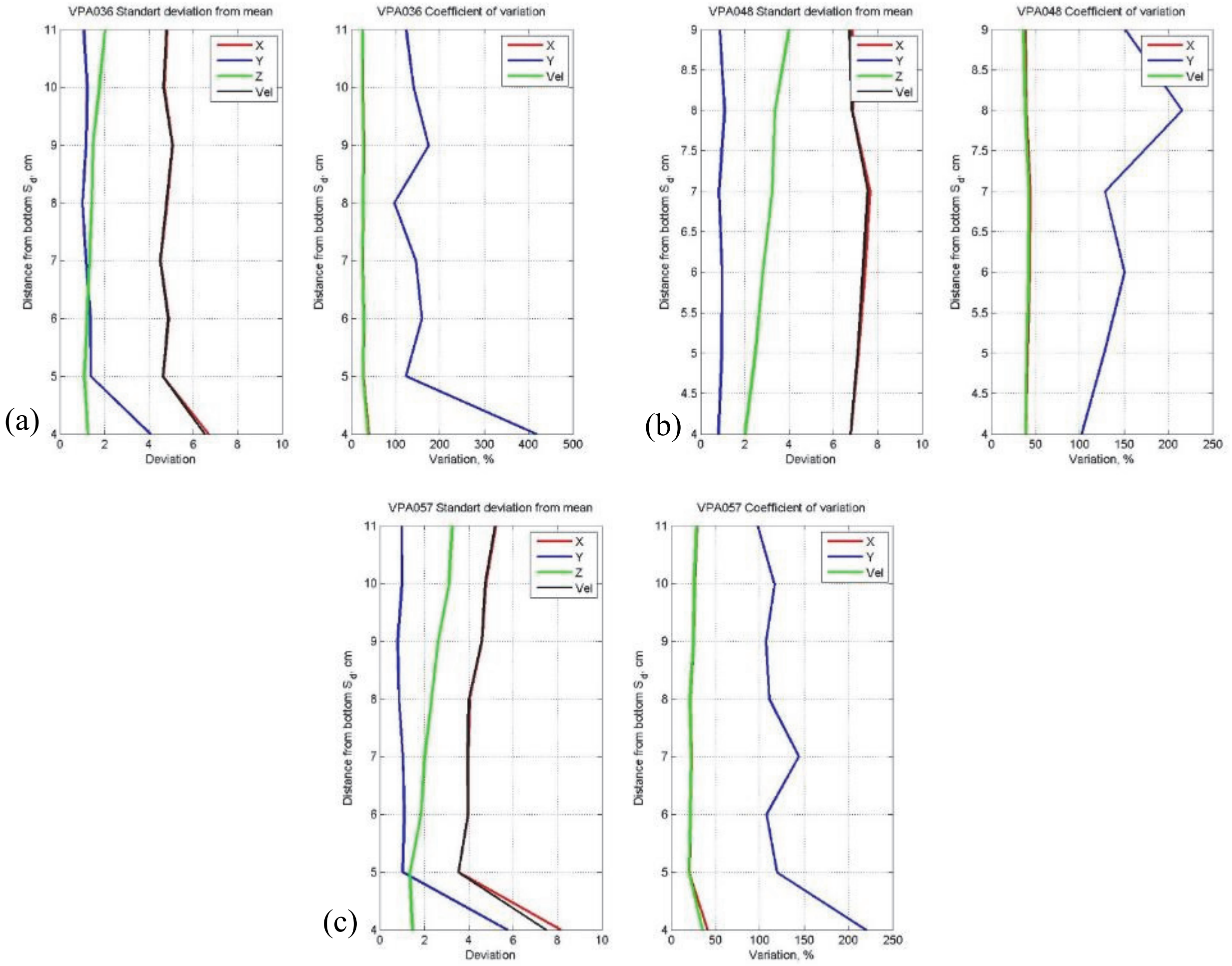

Figure 4.9: Statistical data from tests VPA036(a), VPA048(b) and VPA057(c)

4.1.2 Measurements with PMAR

The results of this section represent conditions with and without waves with the PMAR in place. In each test, a flow rate of 43.74 m^3/h was used. For all tests, measurements were taken from position 9 or 17, which corresponds to 30 cm in front of or behind proposed PMAR location respectively. Figure 4.10 represents the testing set up.

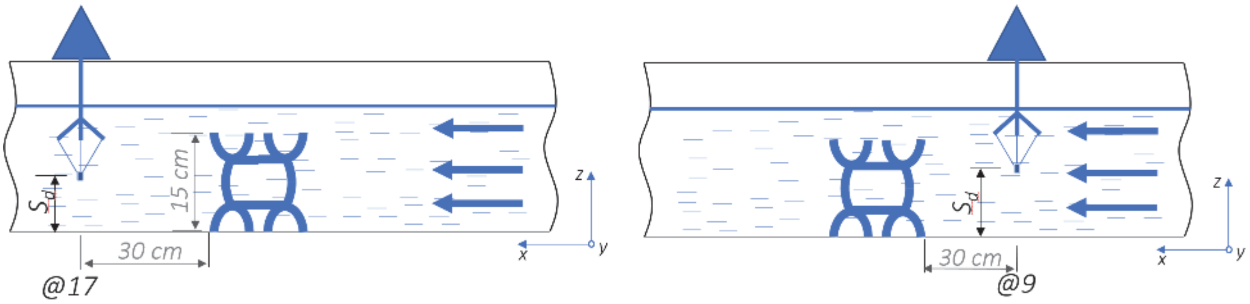

Figure 4.10: Testing set up with PMAR

The results seen in Figure 4.11 correspond to the scenario of constant flow, **no wave,** with PMAR in place. For each test a vertical velocity profile was measured by varying the ADV depth between 4 and 13 cm from the bottom. The ADV was placed at **position 9**. There were three different tests that were conducted with these parameters. The tests were VPA034, VPA045, and VPA071 which corresponds to the first, third and eighth tests respectively. The results can be seen in Figures 4.11 and 4.12.

In all three tests, x-direction velocity maintained fairly consistent values between 18 and 19 cm/s between the depths of 12 and 4 cm. In the case of VPA071, there was a rapid decrease in velocity to 5 cm/s between the depths of 5 and 4 cm, which could be an indication of increased interference of the bottom in the measurements. Y-direction flow velocities varied between the three tests. In the case of VPA034, flow velocities steadily increased with depth, experiencing a flow velocity just about 0 at a depth of 12, and a flow velocity near 2.5 cm/s at a depth of 4 cm. In the case of VPA045, y-direction flow velocities maintained a consistent value just about 1 cm/s between the depths of 12 and 4 cm. VPA071 experienced an increase in y-direction flow velocities between the depths of 13 and 11 cm, at which point the velocities plateaued at just about 1 cm/s between 11 and 5. The z-direction flow velocities were about the same in all three tests. Between the depths of 12 and 4 cm, the z-direction flow velocity slightly fluctuated between 0 and 1 cm/s.

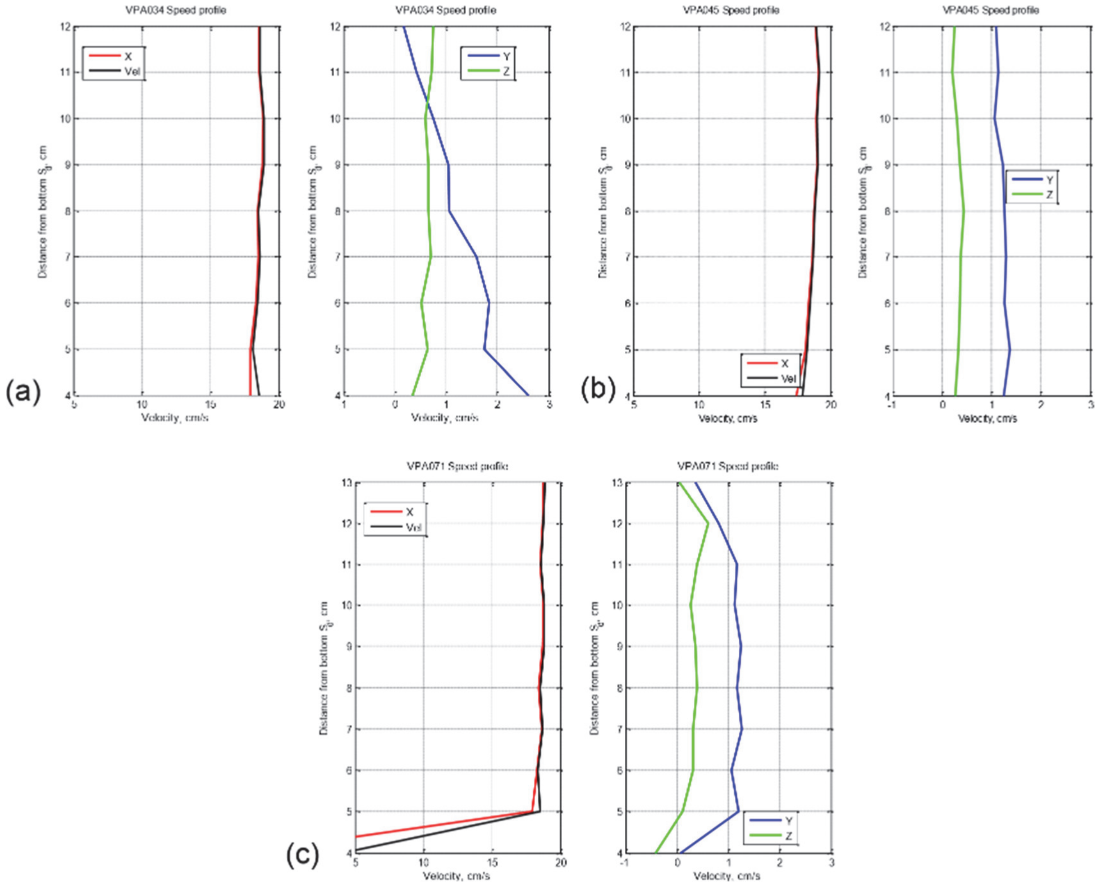

Figure 4.11: Velocity profiles in the x, y and z directions for VPA034(a), VPA045(b) and VPA071 tests from position 9

The statistical data concerning deviation from the mean and coefficient of variation can be seen in Figure 4.12.

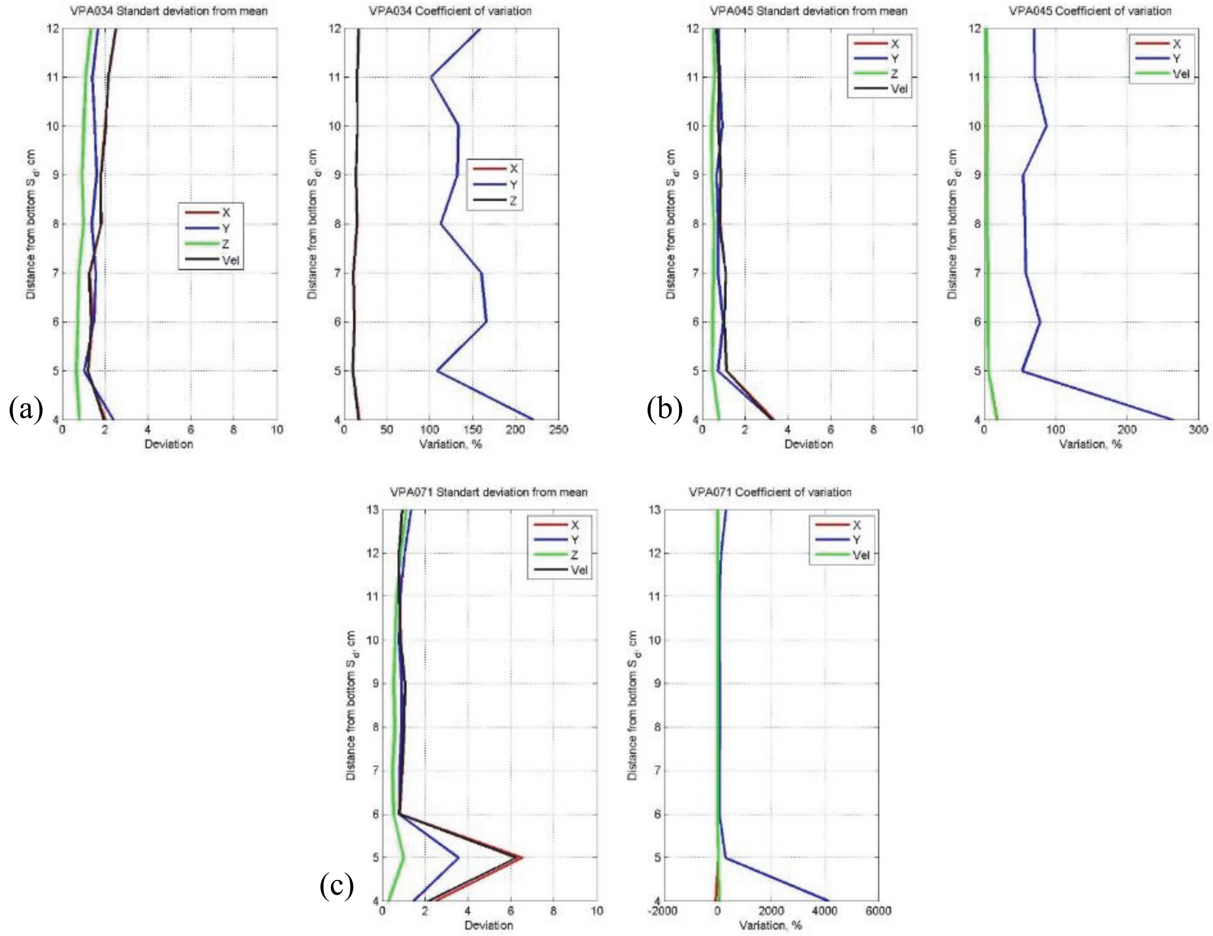

Figure 4.12: Statistical data for VPA034(a), VPA045(b) and VPA071 tests from position 9

The results of this section correspond to the scenario of constant flow, **wave action**, with PMAR in place. For each test a vertical velocity profile was measured by varying the ADV depth between 4 and 11 cm from the bottom. The ADV was placed at **position 9.** An average wave amplitude of 6.3 cm was used. There were two different tests that were conducted with these parameters. The tests were VPA052 and VPA066 which correspond to the fourth and seventh tests respectively. The results can be seen in Figures 4.13 and 4.14.

X-direction flow velocities in both tests were maintained at about 17 cm/s across all depths. In the case of VPA066, the x-direction flow velocity rapidly decreased at 5 cm depth to reach a value of around 6 cm/s at 4 cm depth. Y-direction flow velocities were also consistent between the two tests, registering just below 1 cm/s across the depths, with the exception of VPA066, which experienced a rapid decrease in velocity between 5 and 4 cm, at which point it reached a velocity of -1 cm/s. Z-direction flow velocities registered just about 0, across all depths in both tests. For test VPA066, z-direction flow velocity decreased and reached negative value between the depths of 5 and 4 cm. However this result should be considered with caution.

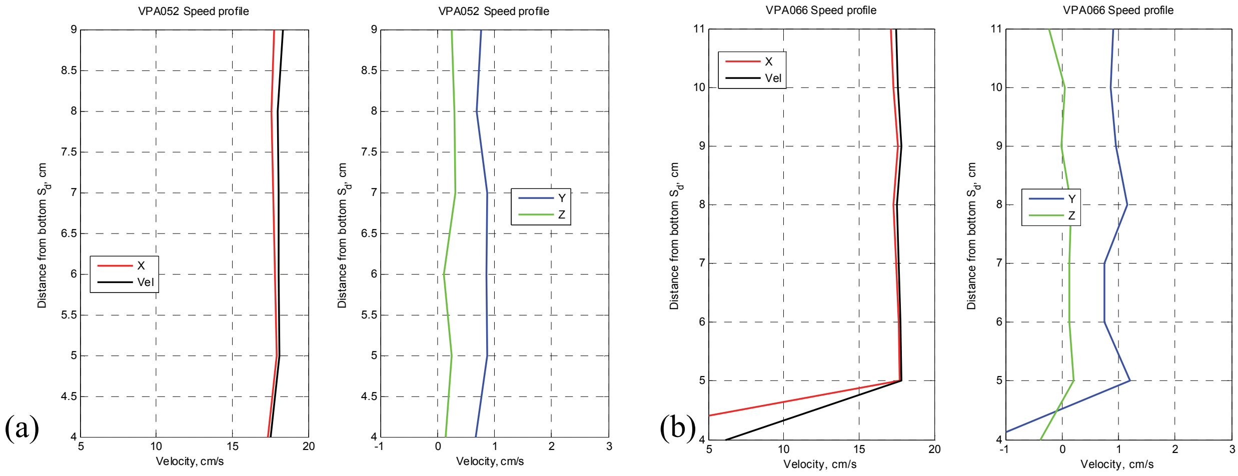

Figure 4.13: Velocity profiles in the x, y and z directions for VPA052(a) and VPA066(b) tests from position 9

The statistical data concerning deviation from the mean and coefficient of variation can be seen in Fiugre 4.14.

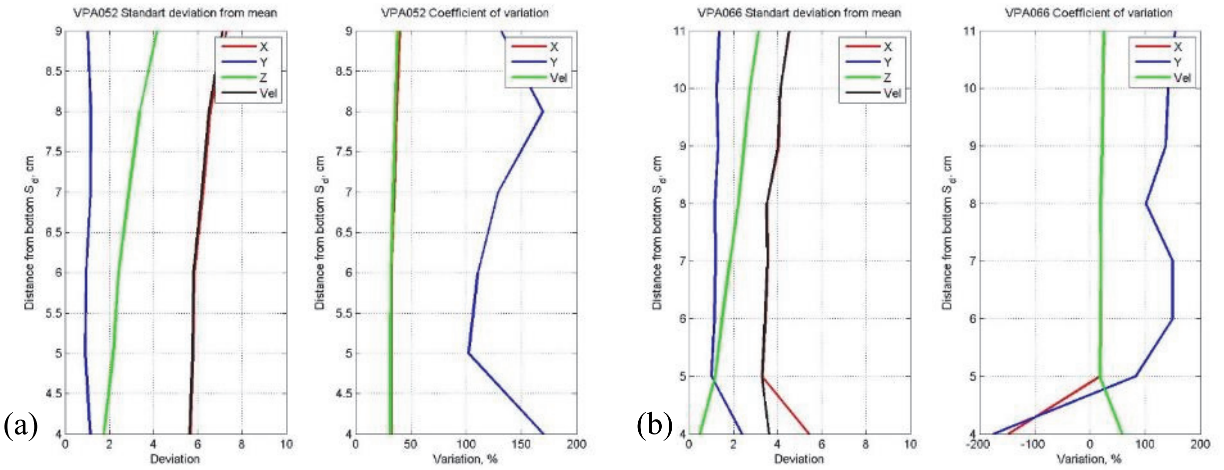

Figure 4.14: Statistical data for VPA052(a) and VPA066(b) tests from position 9

The results of this section correspond to the scenario of constant flow, **no wave**, with the PMAR in place. For each test, a vertical profile was measured by positioning the ADV at depth varying between 4 and 12 cm from the bottom. The ADV was placed at **position 17.** There were three different tests that were conducted with these parameters. The tests VPA034, VPA044, and VPA070 corresponds to the first, third and eighth tests respectively. The results can be seen in Figures 4.15 and 4.16.

X-direction flow velocities in all three tests decreased with depth, in VPA034, the velocity ranged between 15 cm/s to around 11 cm/s whereas the velocities in VPA044 and VPA070 ranged from 17 cm/s to 11 cm/s. Y-direction flow had slightly different characteristics in each of the three tests. For VPA034, velocity hovered near 1 cm/s across all depths with a slight increase to around 1.3 cm/s near 11 cm depth. In VPA044, y-direction velocity decreased between depths of 12 and 9 cm, and then steadily increased from 0.3 cm/s to 1.5 cm/s near the bottom. Finally, VPA070 showed a decrease from 1 to 0.2 cm/s between the depths of 11 and 7 cm, a slight plateau between 7 and 6 cm, and then a steady increase to around 2.3 cm/s at the bottom. Z direction flow in VPA034 steadily decreased from 1 cm/s to -0.2 cm/s with depth. In VPA044 z-direction flow velocity saw a slight increase from -0.2 to 0.5 cm/s between the depths of 12 and 9 cm, and then a steady decrease back to -0.2 cm/s until the bottom. Similarly, VPA070 z-direction flow velocity showed a slight increase in velocities between depths 11 to 7 cm (-0.2 cm/s to 0.8 cm/s) and then a steady decrease from 7 cm to the bottom, returning to the velocity -0.2 cm/s.

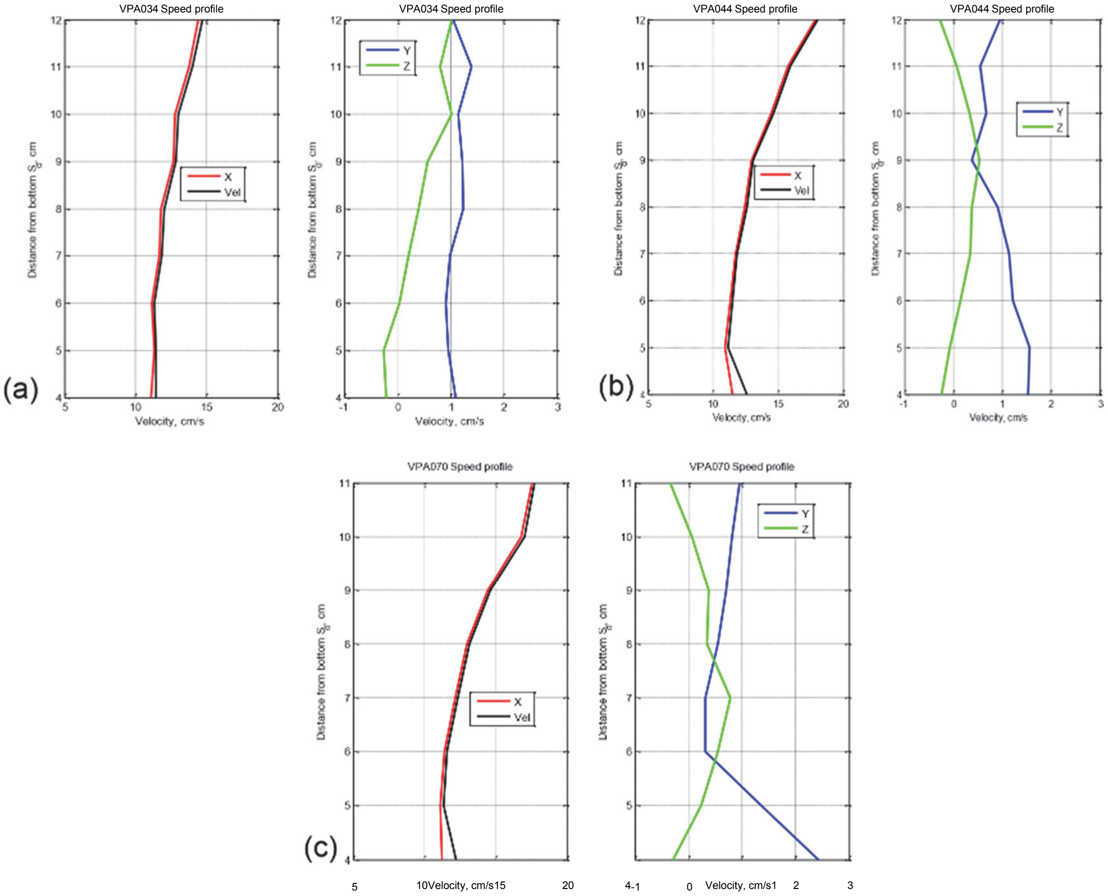

Figure 4.15: Velocity profiles in the x, y and z directions for VPA034(a), VPA044(b) and VPA070(d) tests from position 17

The statistical data concerning deviation from the mean and coefficient of variation can be seen in Figure 4.16.

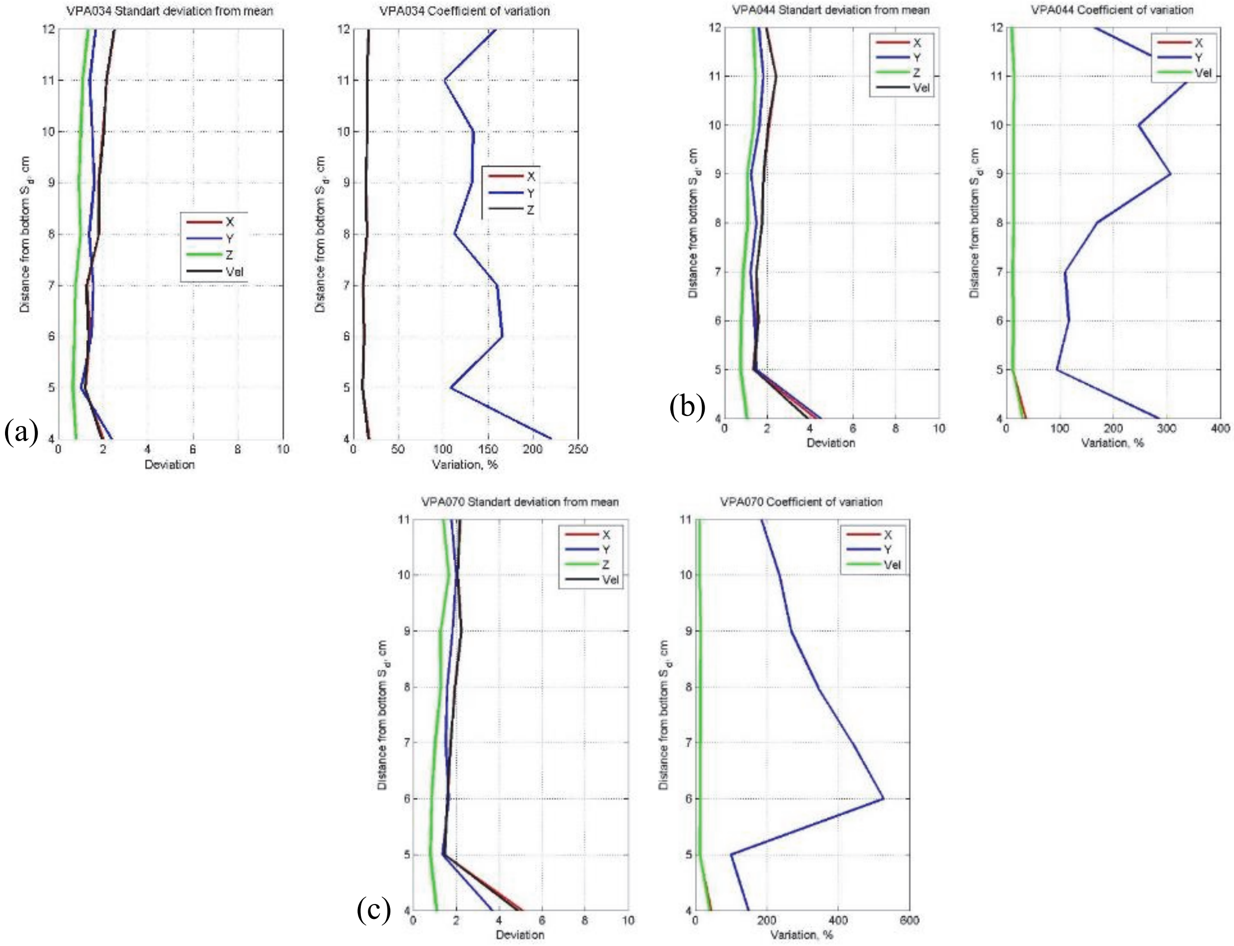

Figure 4.16: Statistical data for VPA034(a), VPA044(b) and VPA070(c) tests from position 17

The results of this section correspond to the scenario of constant flow, with **waves**, and with PMAR in place. For each test a vertical velocity profile was measured by varying the ADV depth between 4 and 12 cm from the bottom. The ADV was placed at **position 17**. An average wave amplitude of 6.3 cm was used during this test. There were three different tests that were conducted with these parameters. The tests were VPA051 and VPA065 which corresponds to the fourth and seventh tests respectively. The results can be seen in Figures 4.17 and 4.18.

In both cases, there was a decrease in x-direction velocity with depth. In the case of VPA051 x-direction velocity decreased from 14 cm/s at a depth of 10 cm to about 10 cm/s at a depth of 7 cm at which point the velocity plateaued and stayed about the same until the bottom measurement of 4 cm. VPA065 also experienced a decreasing velocity profile, however, the velocity at 11 cm depth was about 13 cm/s and it started to plateau at 8 cm depth at a velocity of about 10.5 cm/s until a depth of 5 cm. Y-direction flow varied between the two tests. In the case of VPA051, the y-direction velocity started at about 0 at 10 cm depth and then slowly increased as distance from the bottom decreased, reaching a maximum value near the bottom (4 cm depth) at a rate of 1 cm/s. In the case of VPA065, the velocity was over 1 cm/s at 11 cm depth and then slightly fluctuated around 1 cm/s until 5 cm depth at which point it rapidly decreased, reaching nearly -1 cm/s at 4 cm depth. Z-direction flow also varied between the tests. In the case of VPA051, z-direction velocity fluctuated slightly with depth but centered around 0 cm/s. There were slightly negative flow values at the top and bottom of the testing region, and it reached a maximum positive velocity at a depth of 7 cm of about 0.5 cm/s. For test VPA064, the z direction velocity was positive, at about 0.6 cm/s at a depth of 11 cm and negative (~0.3 cm/s) at a depth of 4 cm.

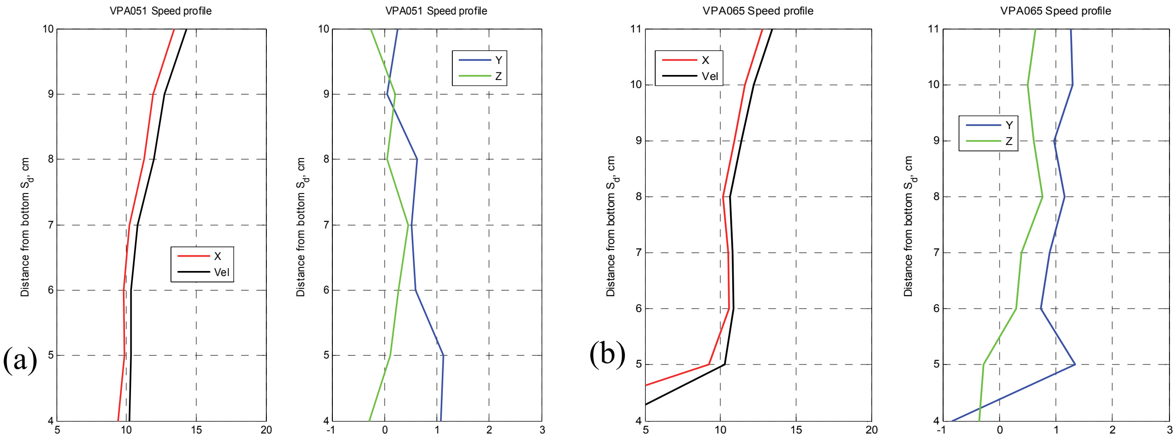

Figure 4.17: Velocity profiles in the x, y and z directions for VPA051(a) and VPA065(b) tests from position 17

The statistical data concerning deviation from the mean and coefficient of variation can be seen in Figure 4.18.

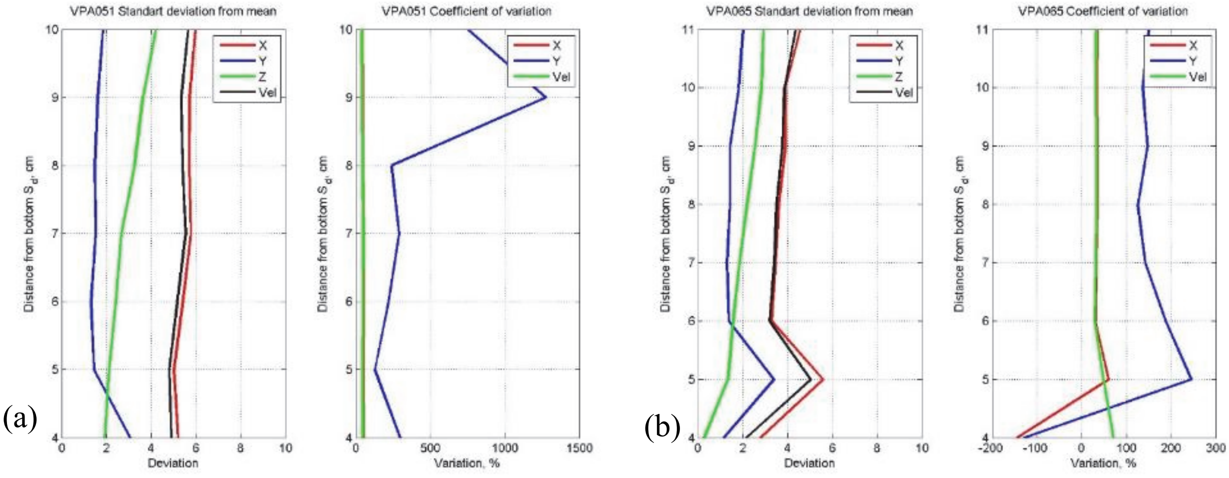

Figure 4.18: Statistical Data from VPA051(a) and VPA065(b)

4.2 Velocity Time Series

The next series of tests were conducted to quantify the variations in flow velocities in the presence of the PMAR. These tests serve to establish a time series to show how the velocity changes throughout the tests. For each test, the ADV was put in place and measurements were taken every 3 seconds. The measurements were taken from position 17 at a central depth of 8 cm from the bottom.

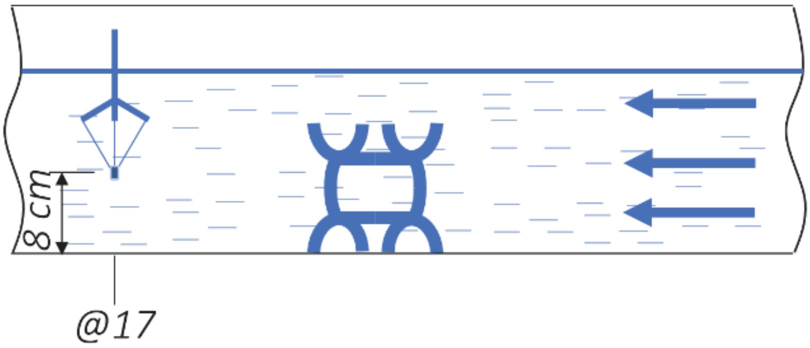

Figure 4.19 Testing set up, Velocity Time Series

The results in this section correspond to the constant flow, **no wave** scenario. The tests were VPA033, VPA037, VPA043, VPA061and VPA068 which correspond to tests one, two, three, six and seven respectively. The tests times varied between 3.5 hours (VPA033) and 27 minutes (VPA037), with most of the tests being run for 2.3 hours (VPA043, VPA 061 and VPA 068). The results can be seen in Figures 4.20 and 4.21.

X-direction flow velocities maintained a fairly consistent value, varying between 10 and 15 cm/s for all tests except VPA033. VPA033 experienced similar flow velocities until just over an hour into the test, at which point the flow velocities started fluctuating between 20 and 6 cm/s until the end of the test. These results may indicate a problem in the hydraulic pump of the water flume, most likely there was air entrapped in the pump. This may actually be corroborated by the fact that excessive microbubbles were visible in the water during this test, and also accumulated at the surface of the instruments. In the subsequent tests this probem no longer happened. Test VPA061 experienced the highest flow velocities of all of the tests, which fluctuated between 2 and 1.5 cm/s throughout the test. Finally, VPA068 experienced ydirection flow velocities which ranged from 2 cm/s at the start of the test, to just below 1 cm/s at the end. The flow velocities decreased from 2 to 1 cm/s within the first 1000 seconds of the tests, and then continued to fluctuate around 1 cm/s until the completion of the test. Z-direction flow velocities were pretty similar across all tests except VPA033 and VPA037. For these tests, the flow velocities slightly fluctuated between 0 and 1 cm/s always maintaining positive values. For VPA037, the velocity fluctuated around 0 cm/s being sometimes slightly positive and sometimes slightly negative. In the case of VPA033, the z-direction flow velocity fluctuated between 0 and 2.5 cm/s reaching a maximum value twice at around 7000 and 9500 seconds.

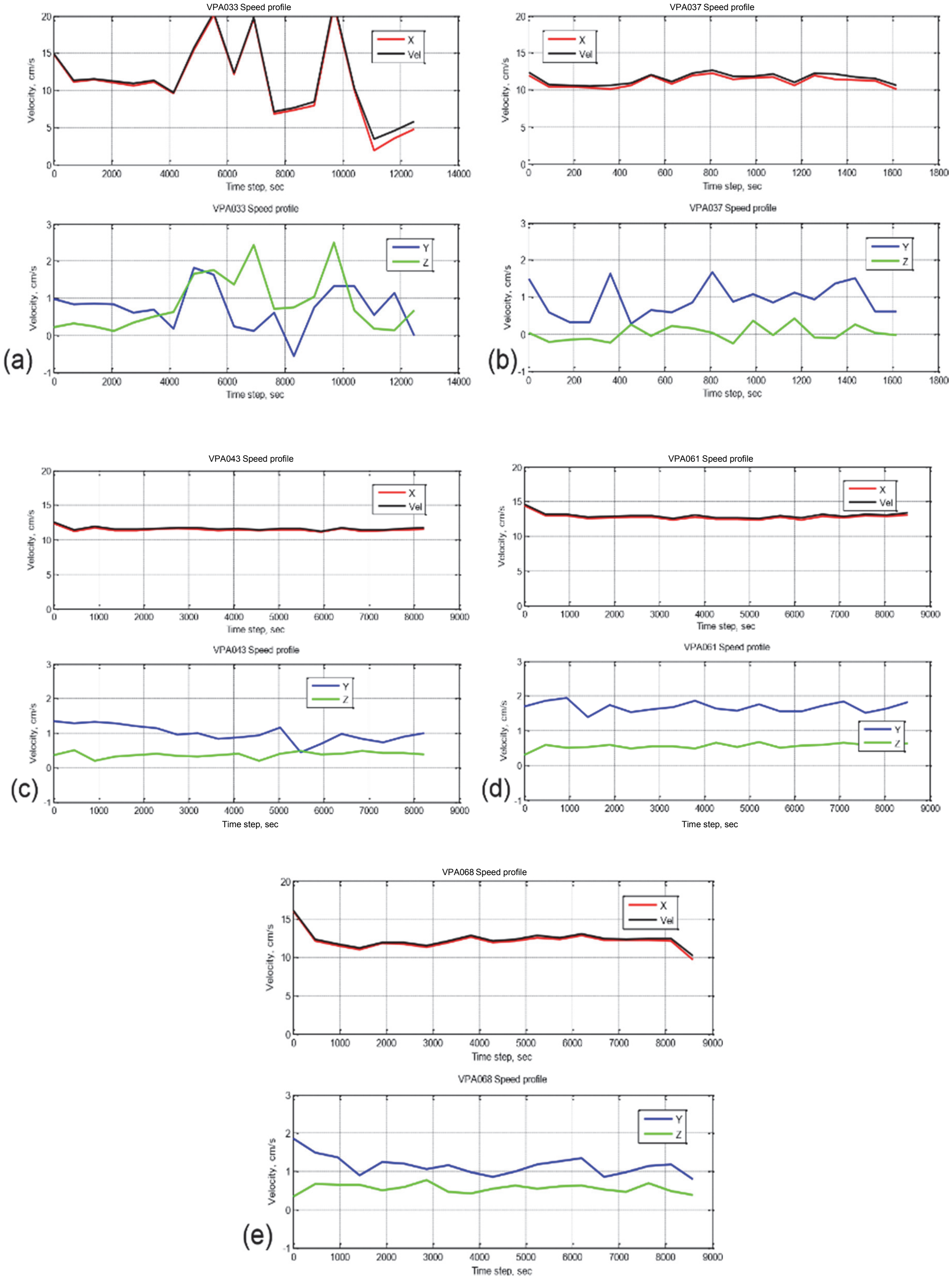

Figure 4.20: Time Series Data for tests VPA033(a), VPA037(b), VPA043(c), VPA061(d) and VPA068(e)

The statistical data concerning deviation from the mean and coefficient of variation can be seen

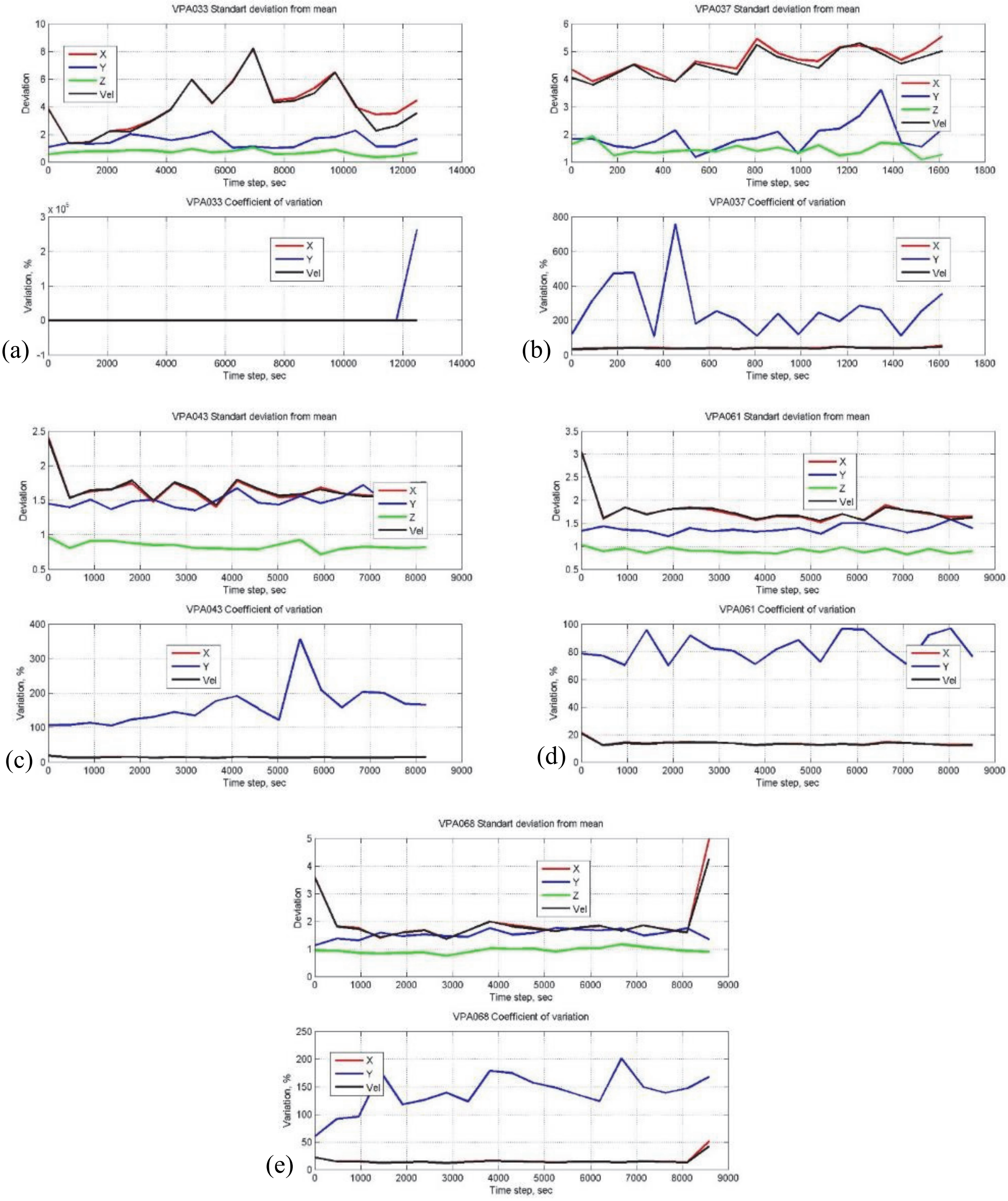

Figure 4.21: Statistical Data for tests VPA033(a), VPA037(b), VPA043(c), VPA061(d) and VPA068(e)

The results in this section correspond to the constant flow, **wave** scenario. An average wave amplitude of 6.3 cm was used. The tests were VPA050, VPA059 and VPA064 which correspond to tests four, five and seven respectively. For each test, the ADV was put in place and measurements were taken every 33 seconds. The tests times varied between 2.8 hours (VPA 064) and 2.3 hours (VPA050 and VPA059). The results can be seen in Figures 4.22 and 4.23.

In all three tests x-direction flow velocity fluctuate slightly between 10 and 13 cm/s throughout the tests. Y-direction flow was fairly consistent throughout all three tests. In the case of VPA050 it fluctuated between 1 and 0.3 cm/s, for VPA059 it fluctuated between 1.3 and 1.8 cm/s and for VPA064 its fluctuations were centered on 1 cm/s. Z-direction flow velocities fluctuated between 0 and 1 cm/s for all three tests.

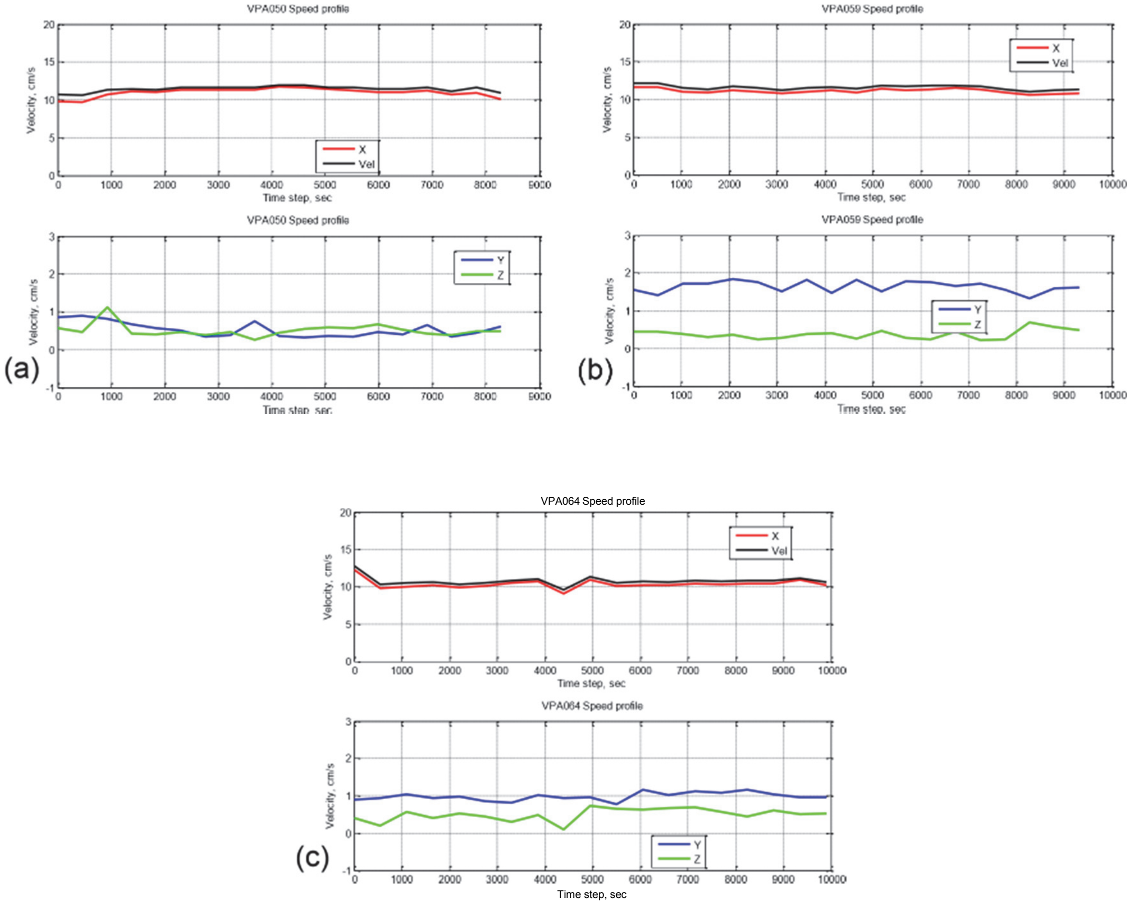

Figure 4.22: Time Series Data for tests VPA050(a), VPA059(b) and VPA064(c)

The statistical data concerning deviation from the mean and coefficient of variation can be seen in Figure 4.23.

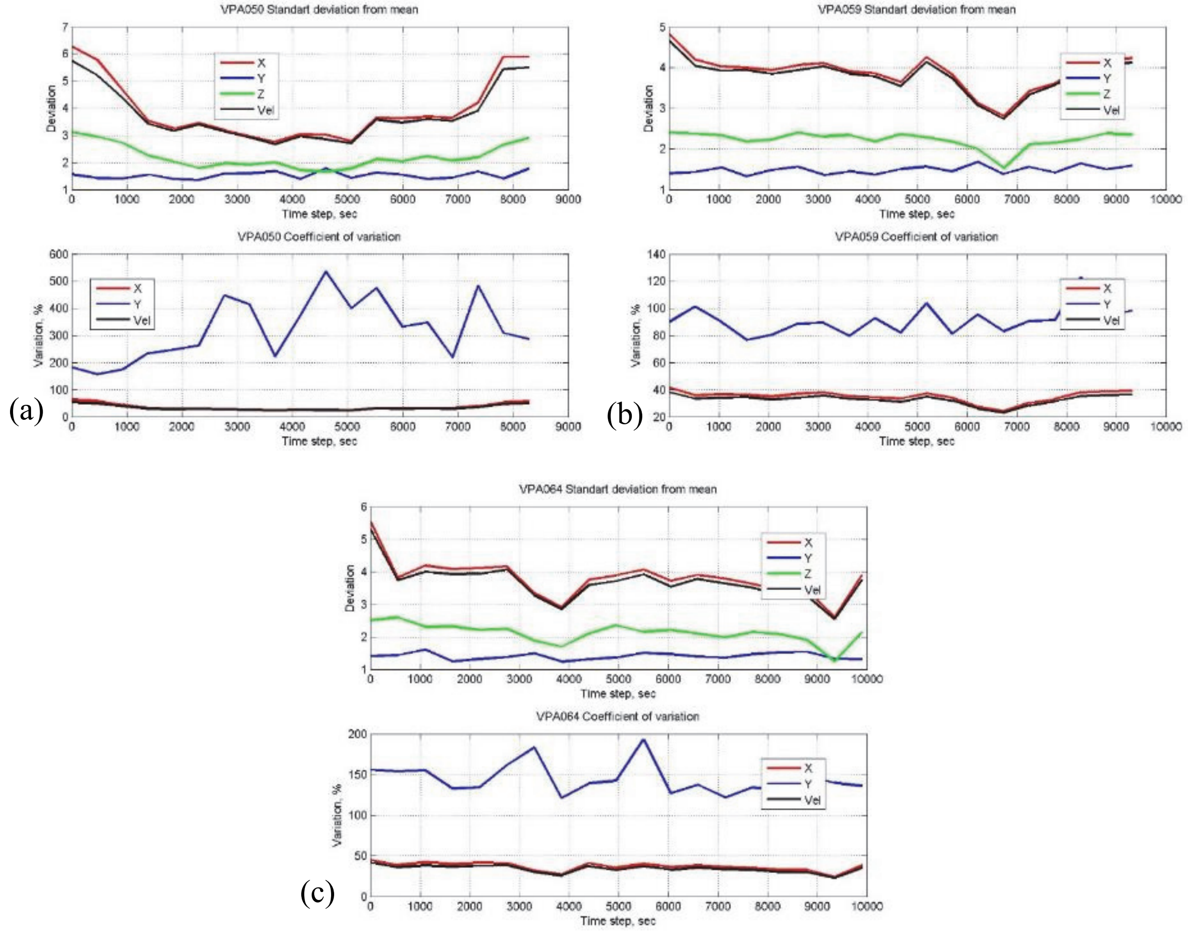

Figure 4.23: Statistical Data for tests VPA050(a), VPA059(b) and VPA064(c)

4.3 Horizontal Profile

Understanding the horizontal profile is important for understanding the overall hydrodynamics of the PMAR. For the following tests the same vertical position was maintained, and measurements were taken at various horizontal positions. Measurements were taken from position 9 to position 17, covering a span of 80 cm. Figure 4.24 shows the testing schematic for the horizontal velocity tests.

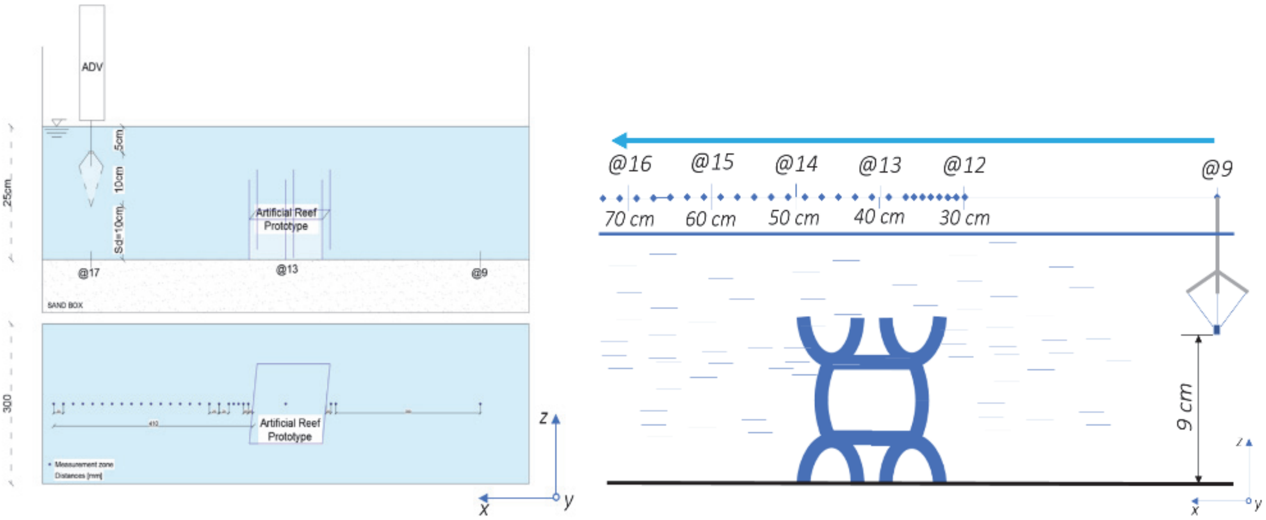

Figure 4.24: ADV fixed in the z direction and travelling along x direction for measurements

The results in this section correspond to tests VPA062 and VPA069, or tests six and eight respectively, Figures 4.25 and 4.26. For both tests, x-direction flow velocities held a constant value until 30 cm from point 9 (which represents the start of the PMAR). VPA062 experienced velocities just under 15 cm/s and VPA069 experienced velocities at around 11 cm/s. After 30 cm from point 9, x-direction flow velocity steadily decreased between 30 and 65 cm, at which point VPA062 x-direction flow velocities steadily decreased (between 15 and 7 cm/s) and VPA069 also experienced a decrease in velocities (between 14 and 8 cm/s) until a distance of 68 cm. Y-direction flow velocities for VPA062 were stable at around 3 cm/s until 30 cm from point 9, at which point it fluctuated with a decreasing tendency (from 3 to 2 cm/s) until just before the 70 cm. The flow velocities fell to 0 at the 70 cm mark and then returned to 2 cm/s right after. For VPA069, y-direction flow velocities steadily increased from 1 to 1.5 cm/s between 0 and 30 cm. After which point the velocities fluctuated around 1 cm/s until 55 cm, when it started to decline until reaching a negative value (-0.8) at 65 cm. Between 65 and 70 cm, velocities increased to 1.5 cm/s. Z-direction flow velocities had similar characteristics between both tests. In each test, the z-direction velocities were steady until 30 cm (VPA062 at 0 cm/s and VPA069 at 0.4 cm/s). After 30 cm, both tests experienced slightly higher velocities, peaking at 1 cm/s for VPA062 and 1.4 cm/s for VPA069. VPA062 maintained velocities between 0 and 1 cm/s until 70 cm, at which point velocities fell to reach -1.7 cm/s at 71 cm before rebounding to just below 1 cm/s at 74 cm. For test VPA069, velocities steadily increased until 58 cm, at which point velocities steadily decreased until the end of the test, finishing just about 0 at 74 cm.

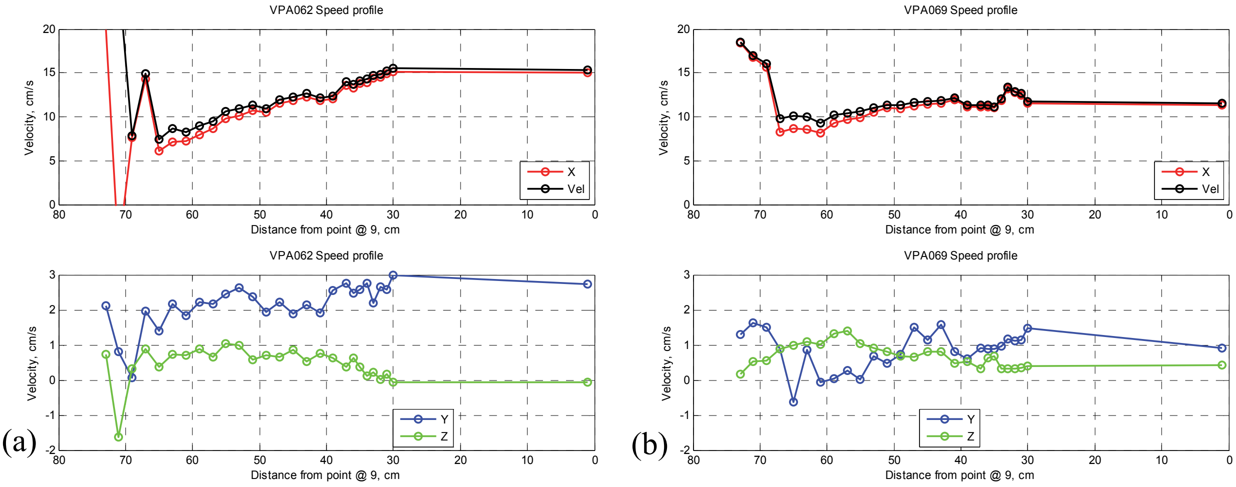

(a) (b)

Figure 4.25: Time Series Data for tests VPA062(a), and VPA069(b)

The statistical data concerning deviation from the mean and coefficient of variation can be seen in Figure 4.26.

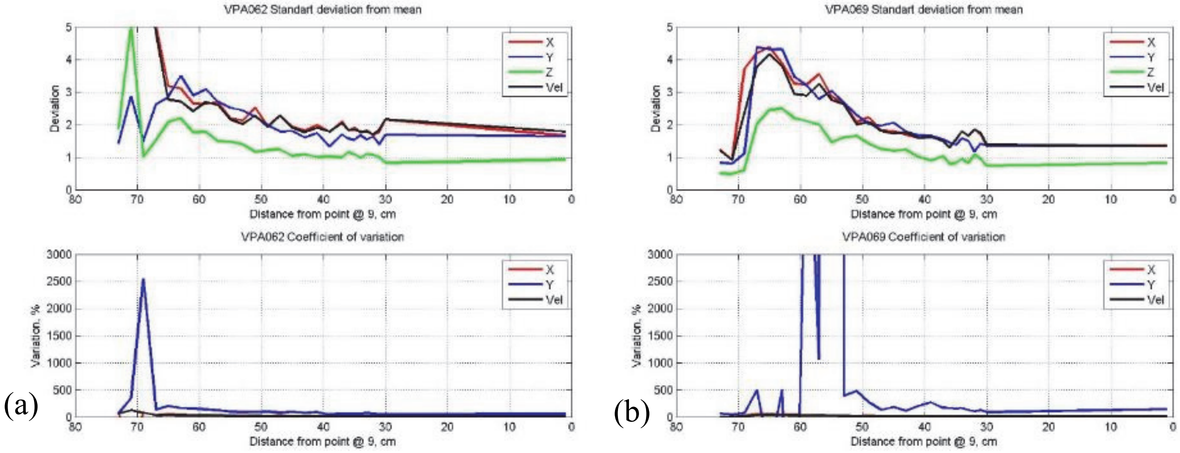

(a) (b)

Figure 4.26: Statistical data for tests VPA062(a), and VPA069(b)

4.4 Photogrammetric Survey

The following results represent the photogrammetric surveys conducted at the completion of each test. For each test three images were created: a 3D model, reconstructed digital elevation model (DEM) and a reconstructed digital orthomosaic model (DOM). In all images, red arrows indicate the direction of water flow.

4.4.1 Test 1

There were not enough photos taken after the first tests to accurately reconstruct the elevation model. A rough 3D image was generated and can be seen in Figure 4.27.

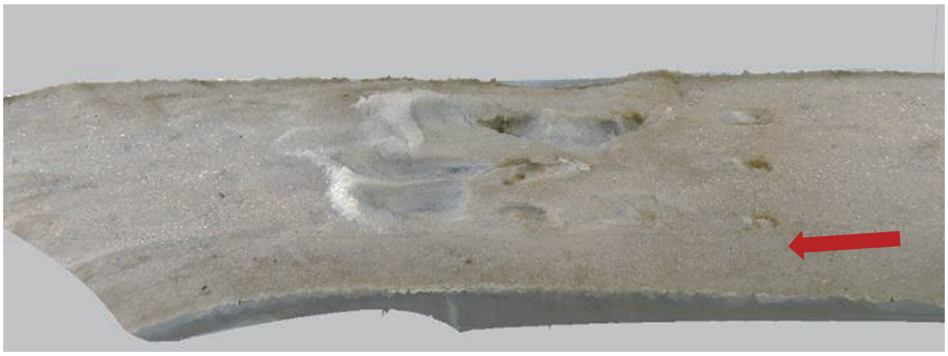

Figure 4.27: 3D image generated from Test 1. Red arrow indicates direction of water flow.

4.4.2 Test 2

Through stitching together, the individual photos taken after the completion of test 2, the following images were recreated, Figure 4.28. A reconstructed digital model, as seen from the top and side, show the erosion and scouring patterns from the test.

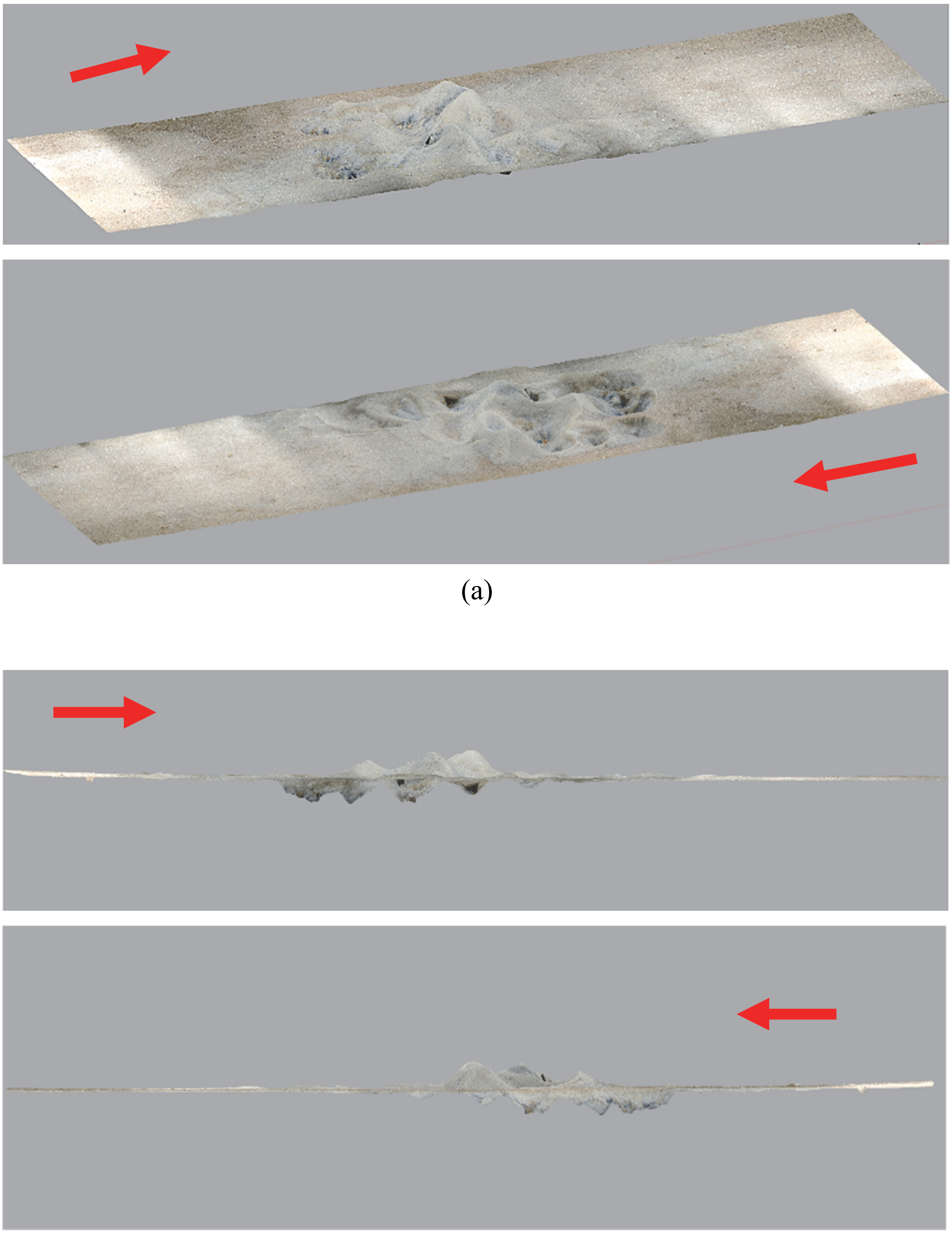

(a)

(B)

Figure 4.28: Reconstructed digital 3D model from test 2: perspective (a) and side view (b). Red arrow indicates direction of water flow.

Reconstructed digital elevation maps were then generated out of this 3D model, Figure 4.29. For test 2, the elevation varied between -0.042 and 0.009 m. Contour lines were added to images b and c representing elevation difference of 0.002 m. In these maps, negative values indicate areas of erosion and positive values indicate areas of accretion. Figure 4.29c shows the track line for depth measurements taken. These values can be found in the Appendix, Figure 1.

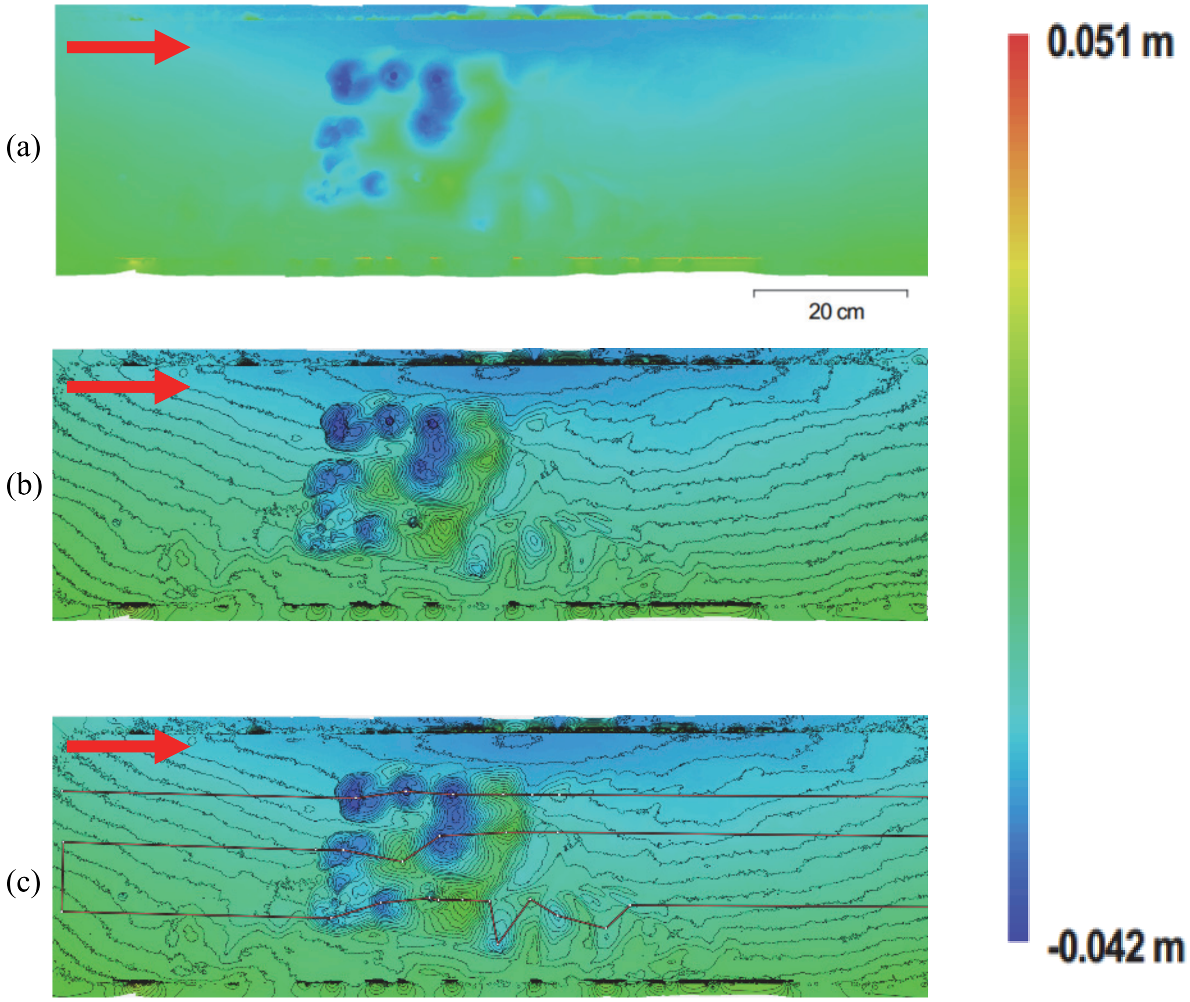

Figure 4.29: Reconstructed digital elevation model from test 2: without contours line (a) and with contours line (b, c). Red arrow indicates direction of water flow.

The reconstructed digital elevation model was then overlaid on the orthogonal image to create the digital orthomosaic model, Figure 4.30.

Figure 4.30: Reconstructed digital orthomosaic model from test 2: without (a) and with contours line (b). Red arrow indicates direction of water flow.

4.4.3 Test 3

Through stitching together, the individual photos taken after the completion of test 3, the following images were recreated, Figure 4.31. A reconstructed digital model, as seen from the top and side, show the erosion and scouring patterns from the test.

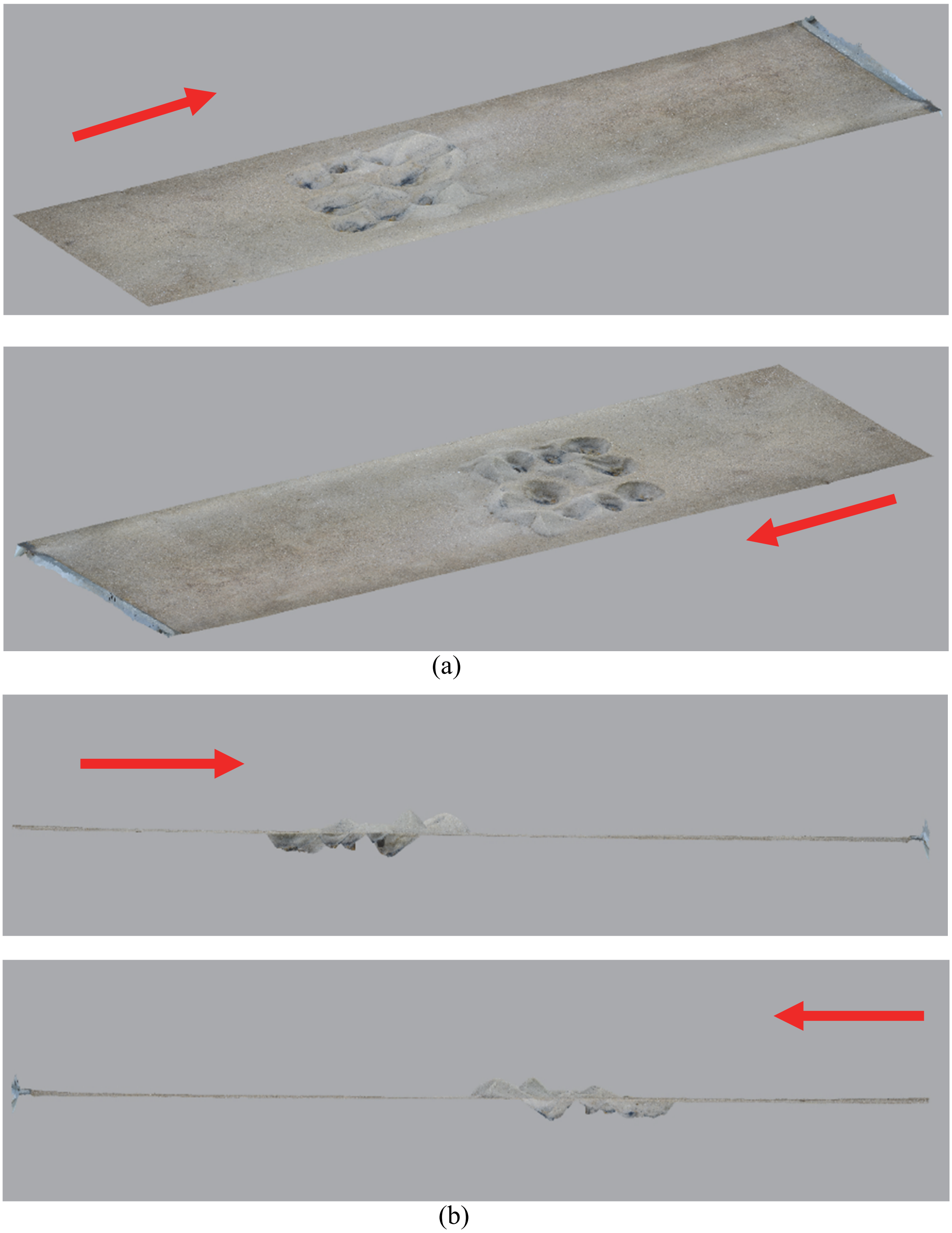

Figure 4.31: Reconstructed digital 3D model from test 3: perspective (a) and side view (b). Red arrow indicates direction of water flow.

Reconstructed digital elevation maps were then generated out of this 3D model, Figure 4.32. For test 3, the elevation ranged from -0.063 to 0.052 m with contours at an interval of 0.002m. Figure 4.32c shows the track line for depth measurements taken. Only after processing the images it was possible to realise that the processing yelded an elevaton map as seen if observed from the bottom, and not from the top as in the other cases. Therefore, in these maps negative values indicate areas of accretion and positive values indicate areas of erosion. These values can be found in the Appendix, Figure 2.

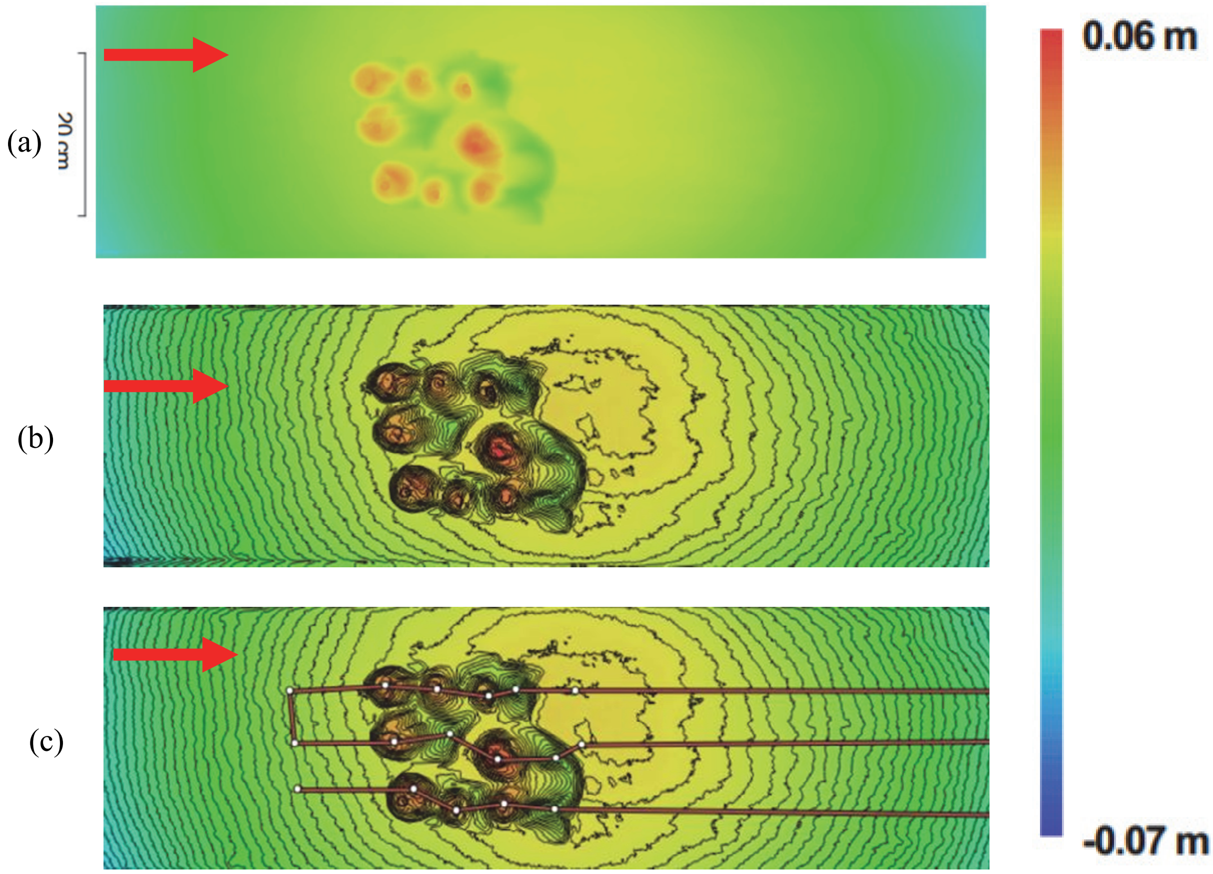

Figure 4.32: Reconstructed digital elevation model from test 3: without (a) and with contours line (b, c). Red arrow indicates direction of water flow.

The reconstructed digital elevation model was then overlaid on the orthogonal image to create the digital orthomosaic model, Figure 4.33. Note, this image of the DEM model is viewed from the bottom plane, and this is why a different camera positioning seems to have been adopted.

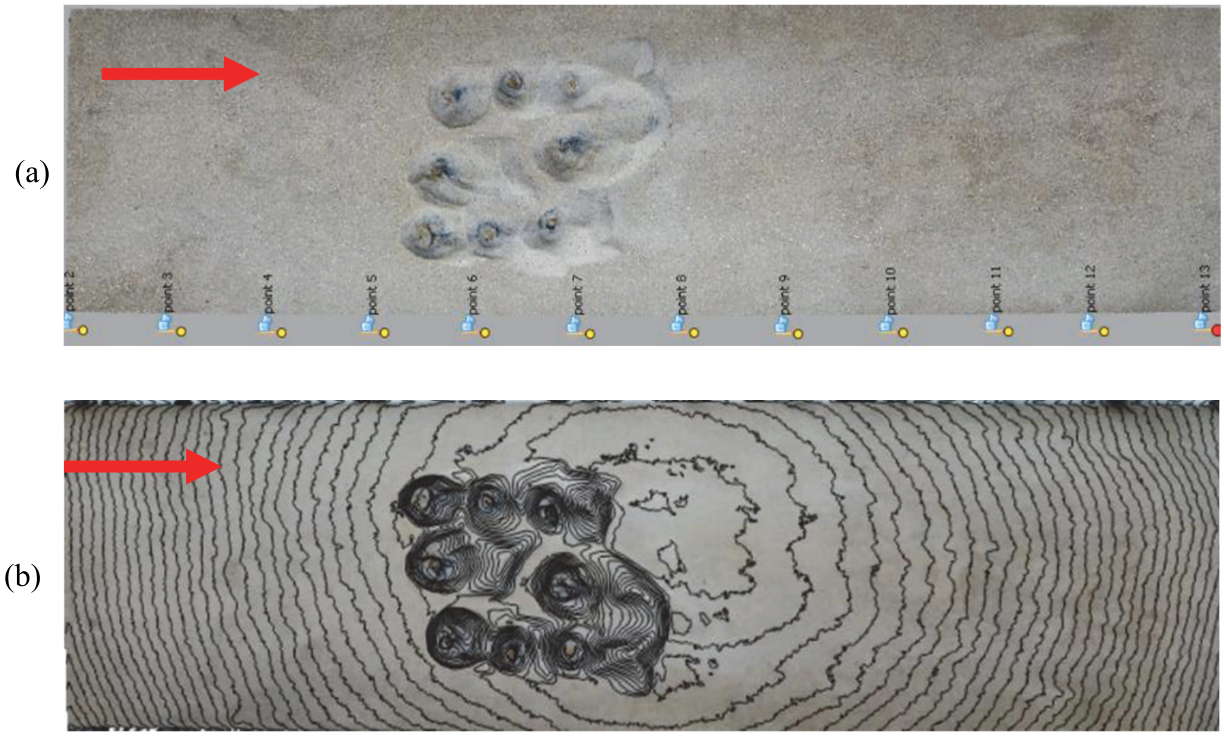

Figure 4.33: Reconstructed digital orthomosaic model from test 3: without (a) and with contours line (b). Red arrow indicates direction of water flow.

4.4.4 Test 4

Through stitching together, the individual photos taken after the completion of test 4, the following images were recreated, Figure 4.34. A reconstructed digital model, as seen from the top and side, shows the erosion and scouring patterns from the test.

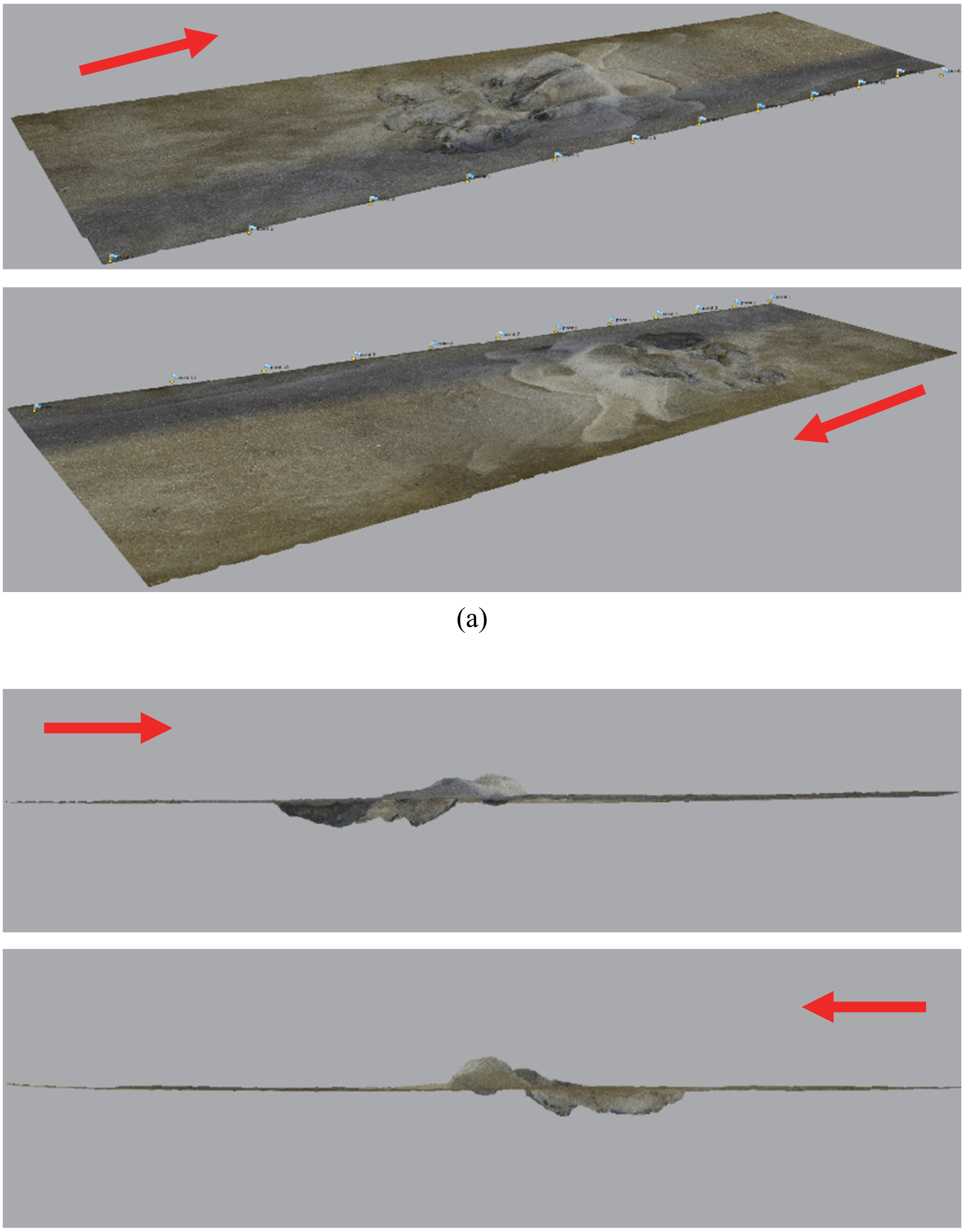

(a)

(b)

Figure 4.34: Reconstructed digital 3D model from test 4: perspective (a) and side view (b). Red arrow indicates direction of water flow.

Reconstructed digital elevation maps were then generated out of this 3D model, Figure 4.35. For test 2, the elevation varied between -0.017 and 0.025 m. Contour lines were added to images b and c at a space of 0.002 m. Figure 4.35c shows the track line for depth measurements taken. Again, and similarly to the previous case, only after processing the images it was possible to realise that the processing yelded an elevaton map as seen if observed from the bottom, and not from the top as in the other cases. Therefore, in these maps the negative values indicate areas of erosion and positive values indicate areas of accretion. These values can be found in the Appendix, Figure 3.

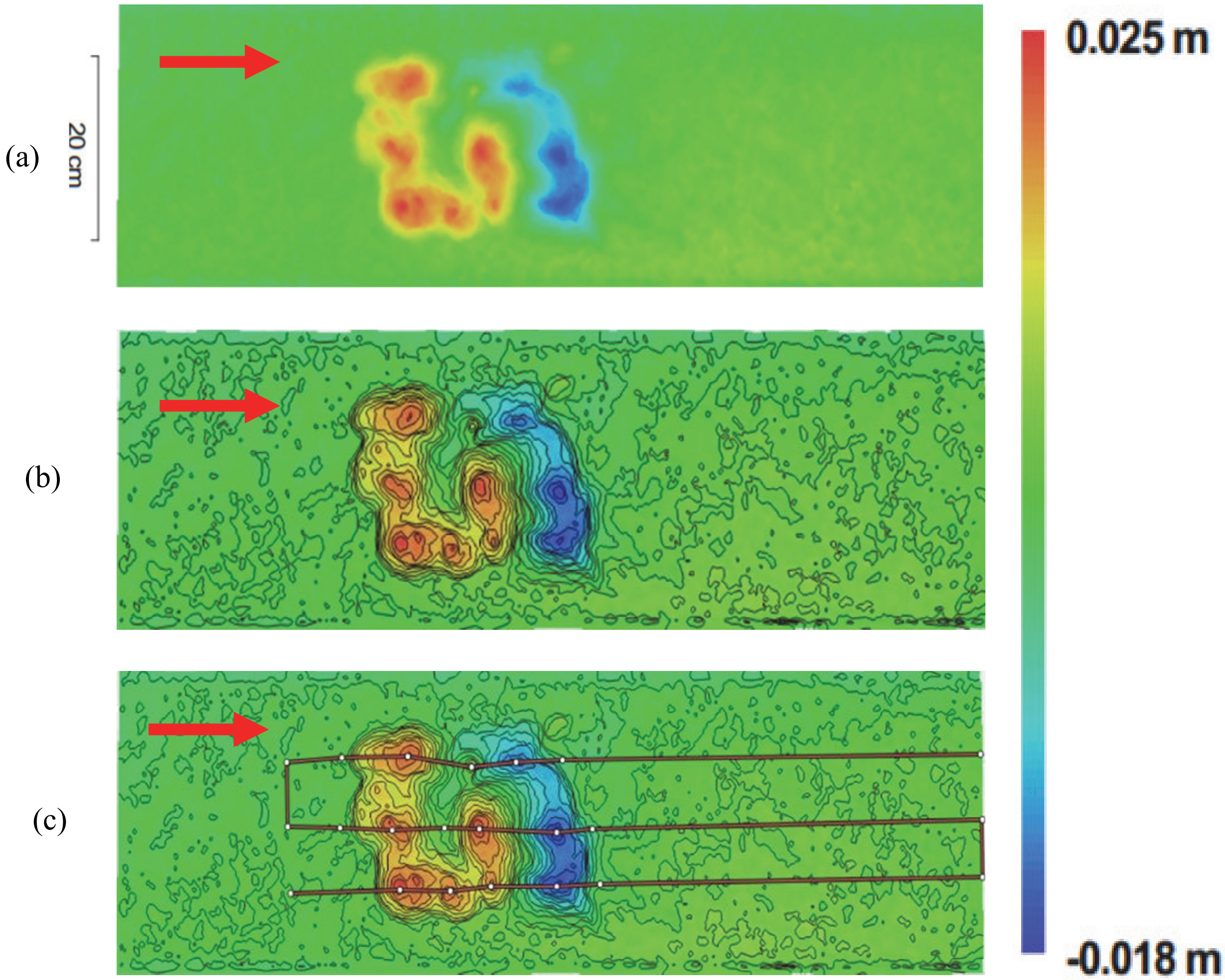

Figure 4.35: Reconstructed digital elevation model from test 4: without (a) and with contours line (b, c). Red arrow indicates direction of water flow.

The reconstructed digital elevation model was then overlaid on the orthogonal image to create the digital orthomosaic model, Figure 4.36. As before, since this image of the DEM model is viewed from the bottom plane it appeared inverted.

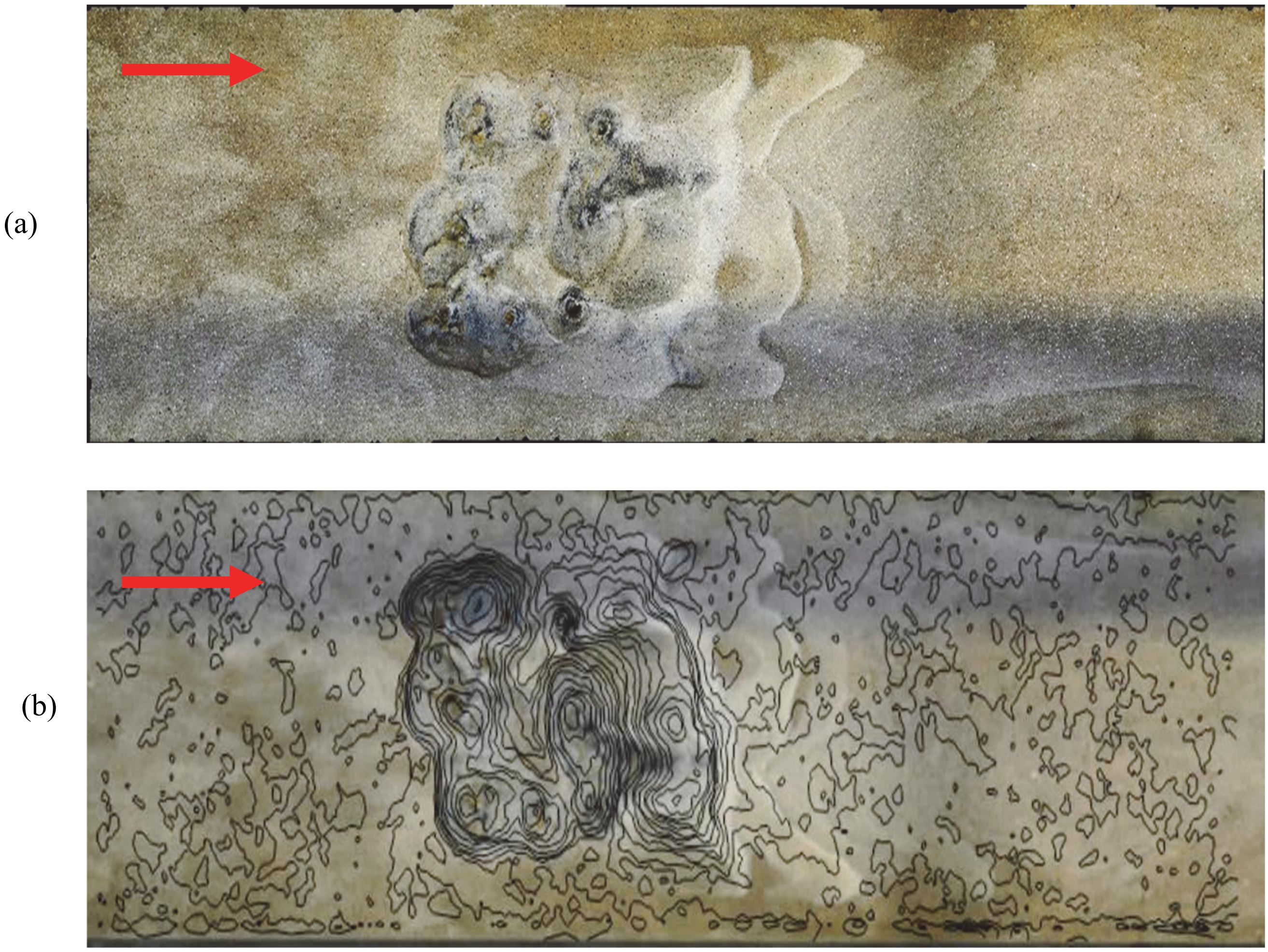

Figure 4.36: Reconstructed digital orthomosaic model from test 4: without (a) and with contours line (b). Red arrow indicates direction of water flow.

4.4.5 Test 5

Through stitching together, the individual photos taken after the completion of test 5, the following images were recreated, Figure 4.37. A reconstructed digital model, as seen from the top and side, show the erosion and scouring patterns from the test.

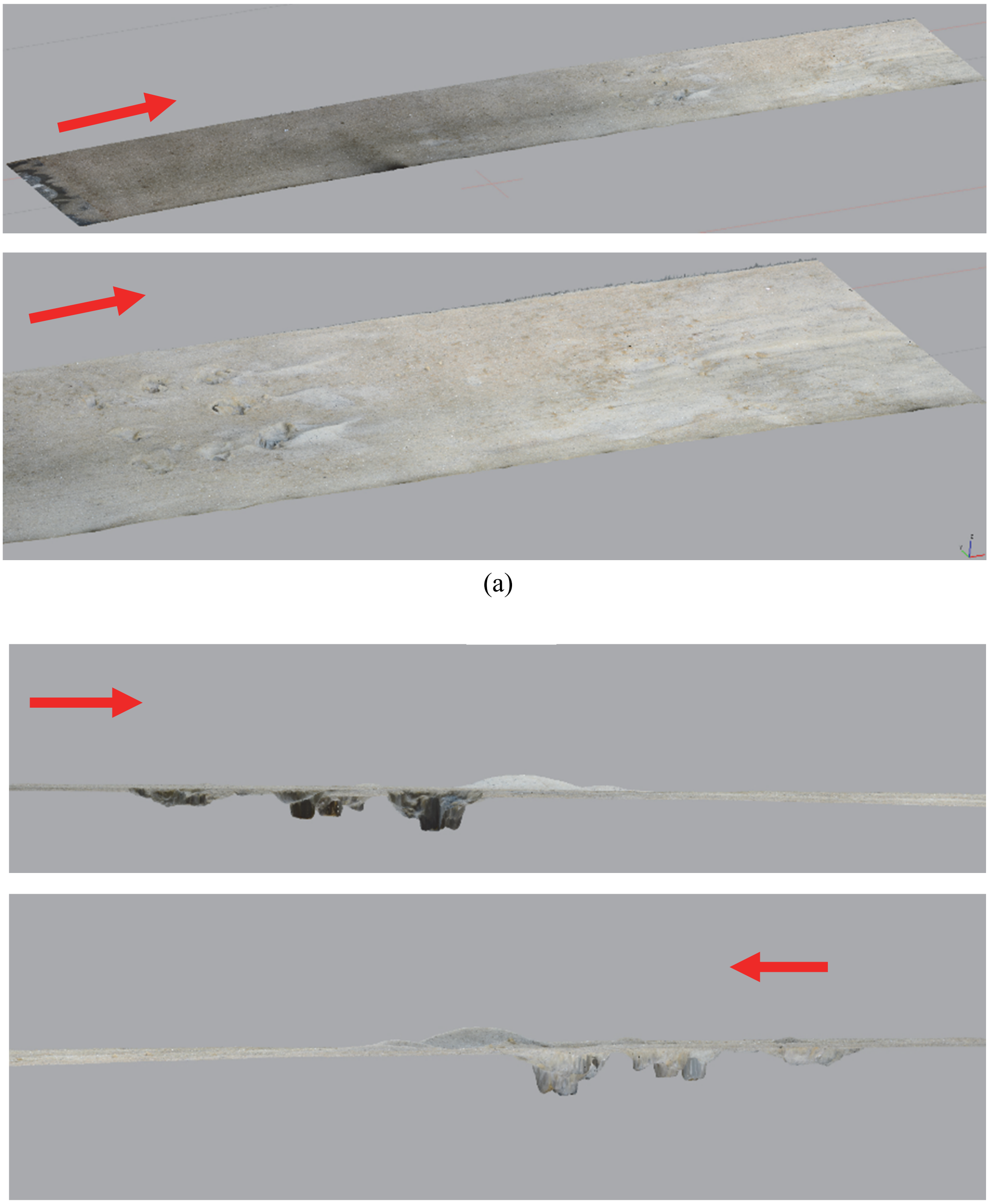
(a)

(b)

Figure 4.37: Reconstructed digital 3D model from test 5: perspective (a) and side view (b). Red arrow indicates direction of water flow.

Reconstructed digital elevation maps were then generated out of this 3D model, Figure 4.38. For test 2, the elevation varied between - 0.017 and 0.052 m. Contour lines were added to images b and c at a space of 0.002 m. Figure 4.38c shows the track line for depth measurements taken. In these maps, negative values indicate areas of erosion and positive values indicate areas of accretion. These values can be found in the Appendix, Figure 4.

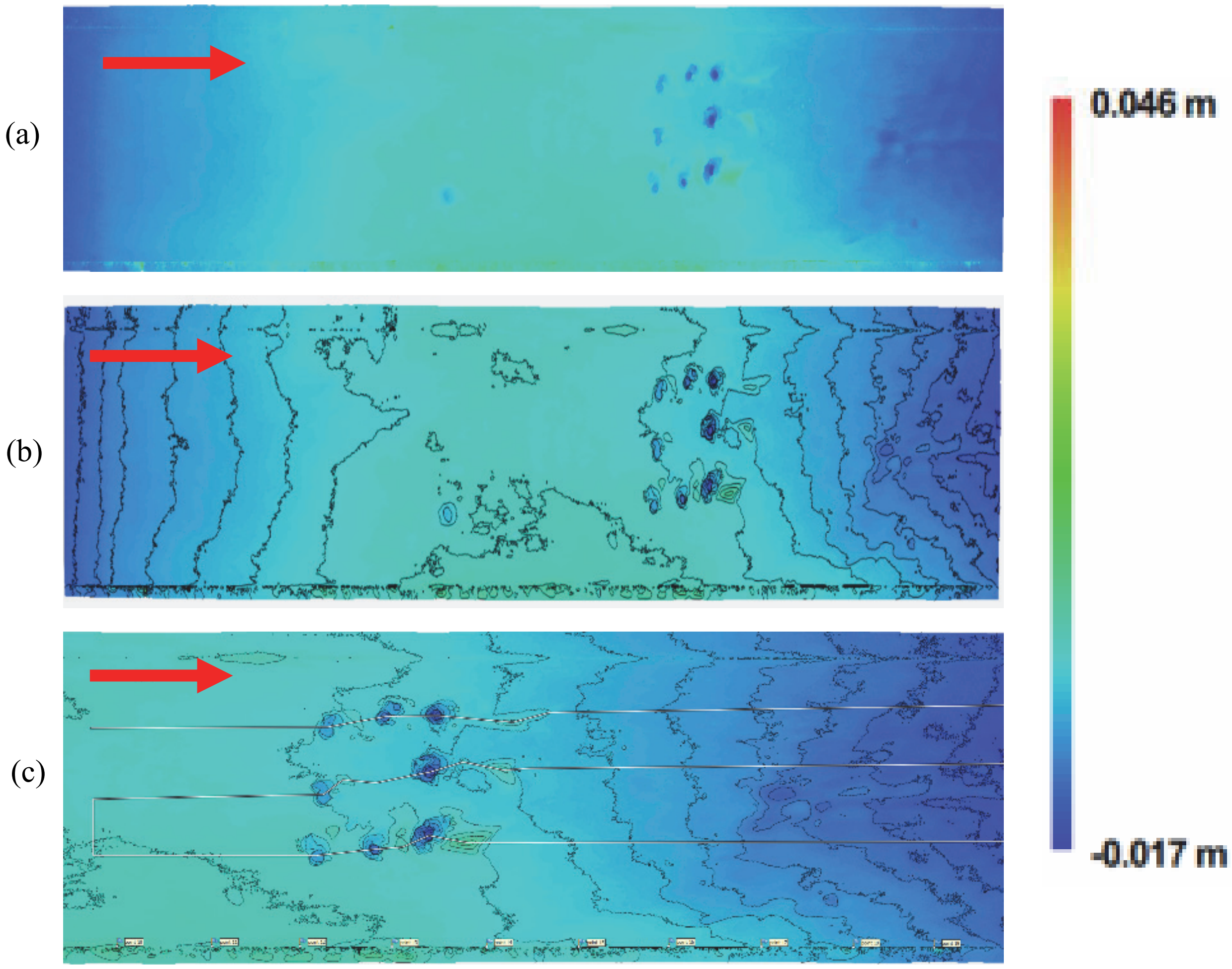

Figure 4.38: Reconstructed digital elevation model from test 5: without (a) and with contours line (b, c). Red arrow indicates direction of water flow.

The reconstructed digital elevation model was then overlaid on the orthogonal image to create the digital orthomosaic model, Figure 4.39.

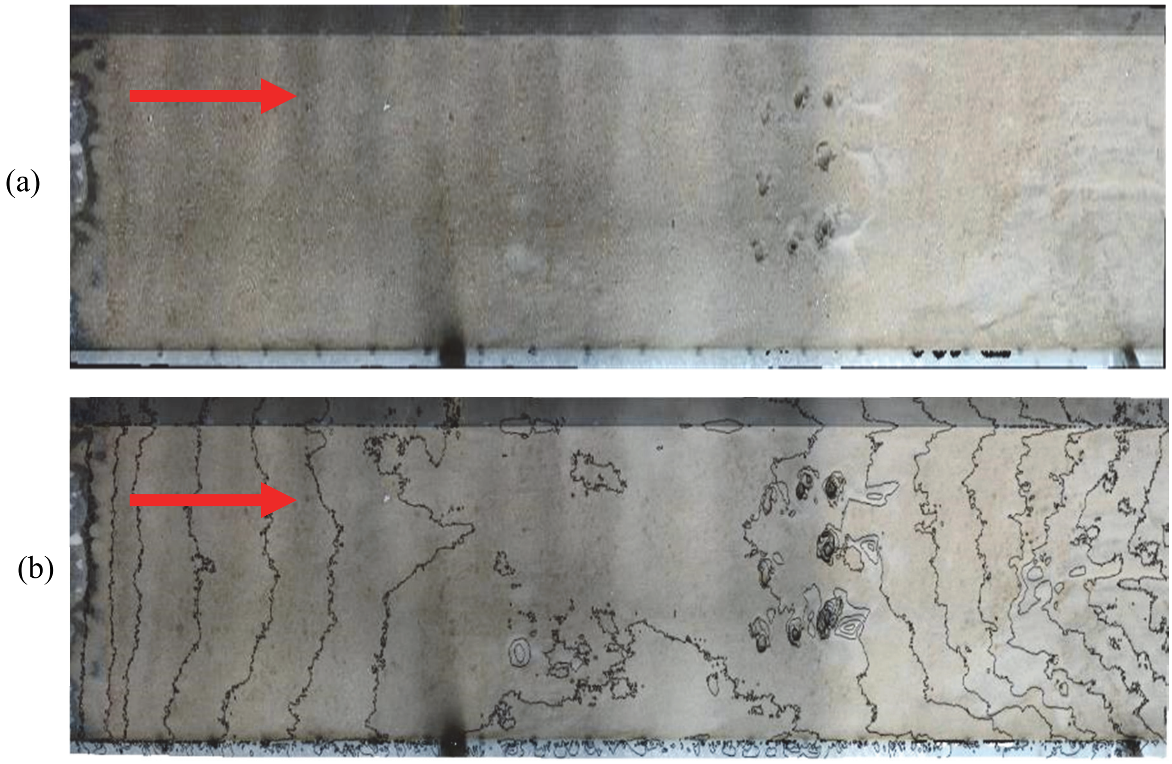

Figure 4.39: Reconstructed digital orthomosaic model from test 5: without(a) and with contours line (b). Red arrow indicates direction of water flow.

4.4.6 Test 6

Through stitching together, the individual photos taken after the completion of test 6, the following images were recreated, Figure 4.40. A reconstructed digital model, as seen from the top and side, show the erosion and scouring patterns from the test.

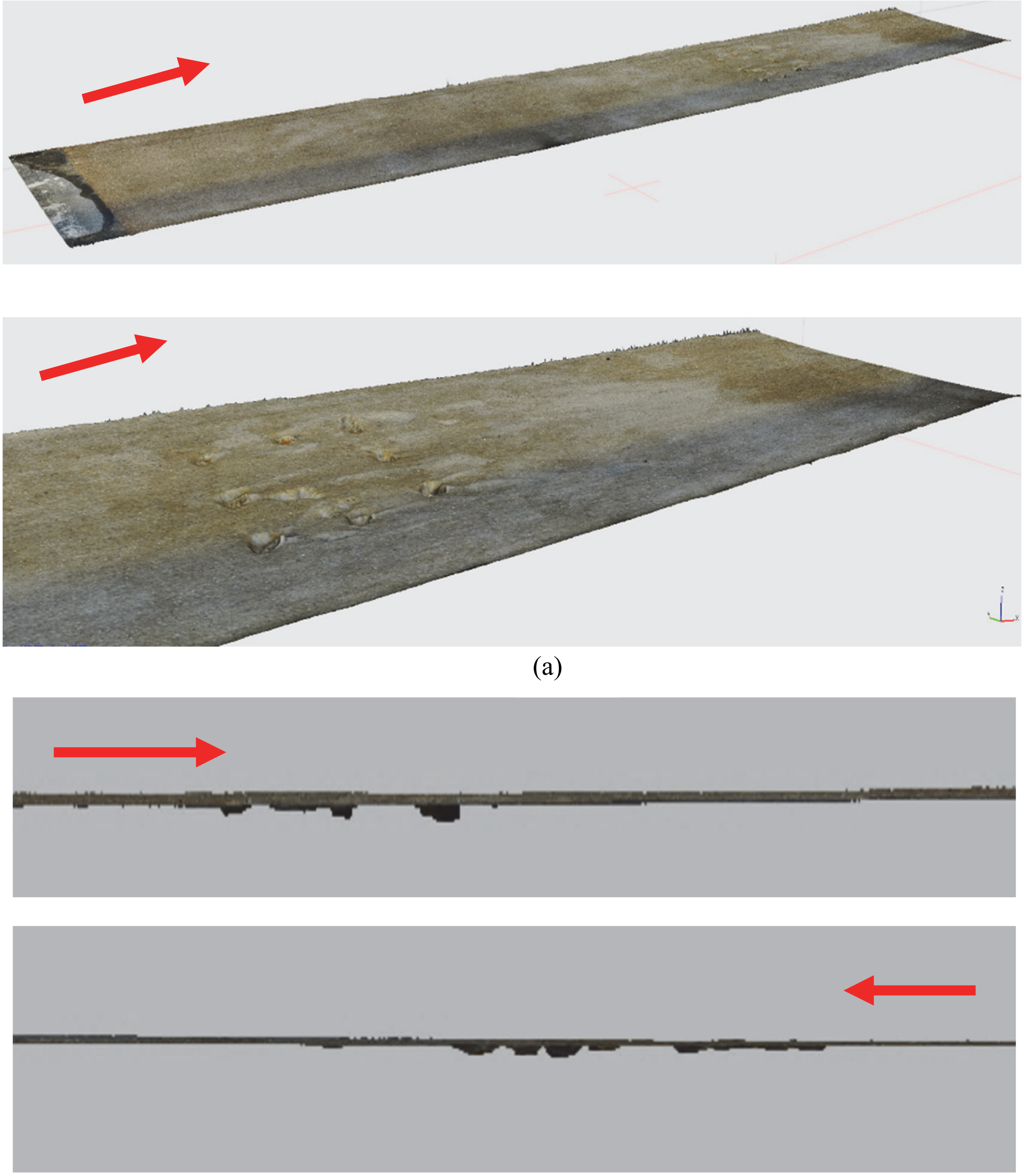

(a)

(b)

Figure 4.40: Reconstructed digital 3D model from test 6: perspective (a) and side view (b). Red arrow indicates direction of water flow.

Reconstructed digital elevation maps were then generated out of this 3D model, Figure 4.41. For test 2, the elevation varied between - 0.011 and 0.038 m. Contour lines were added to images b and c at a space of 0.002 m. Figure 4.41c shows the track line for depth measurements taken. In these maps, negative values indicate areas of erosion and positive values indicate areas of accretion. These values can be found in the Appendix, Figure 5.

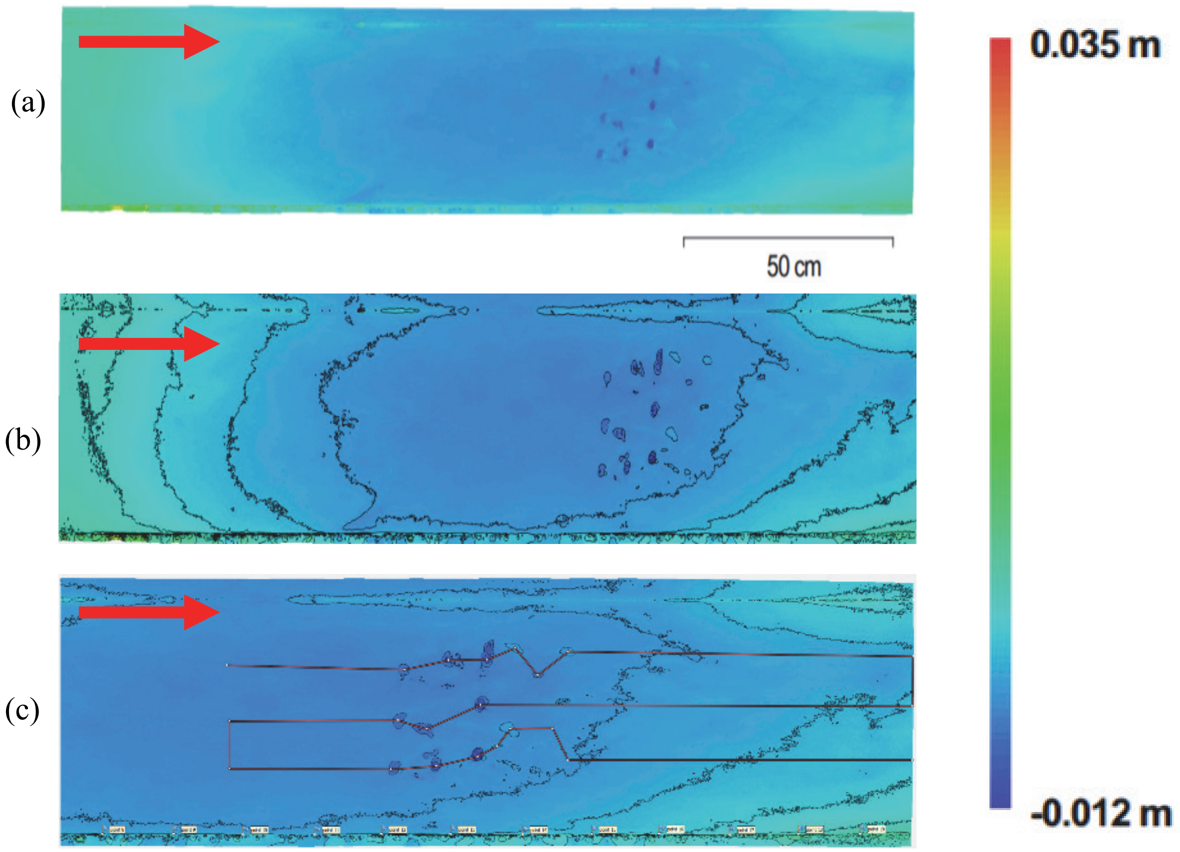

Figure 4.41: Reconstructed digital elevation model from test 6: without (a) and with contours line (b, c). Red arrow indicates direction of water flow.

The reconstructed digital elevation model was then overlaid on the orthogonal image to create the digital orthomosaic model, Figure 4.42.

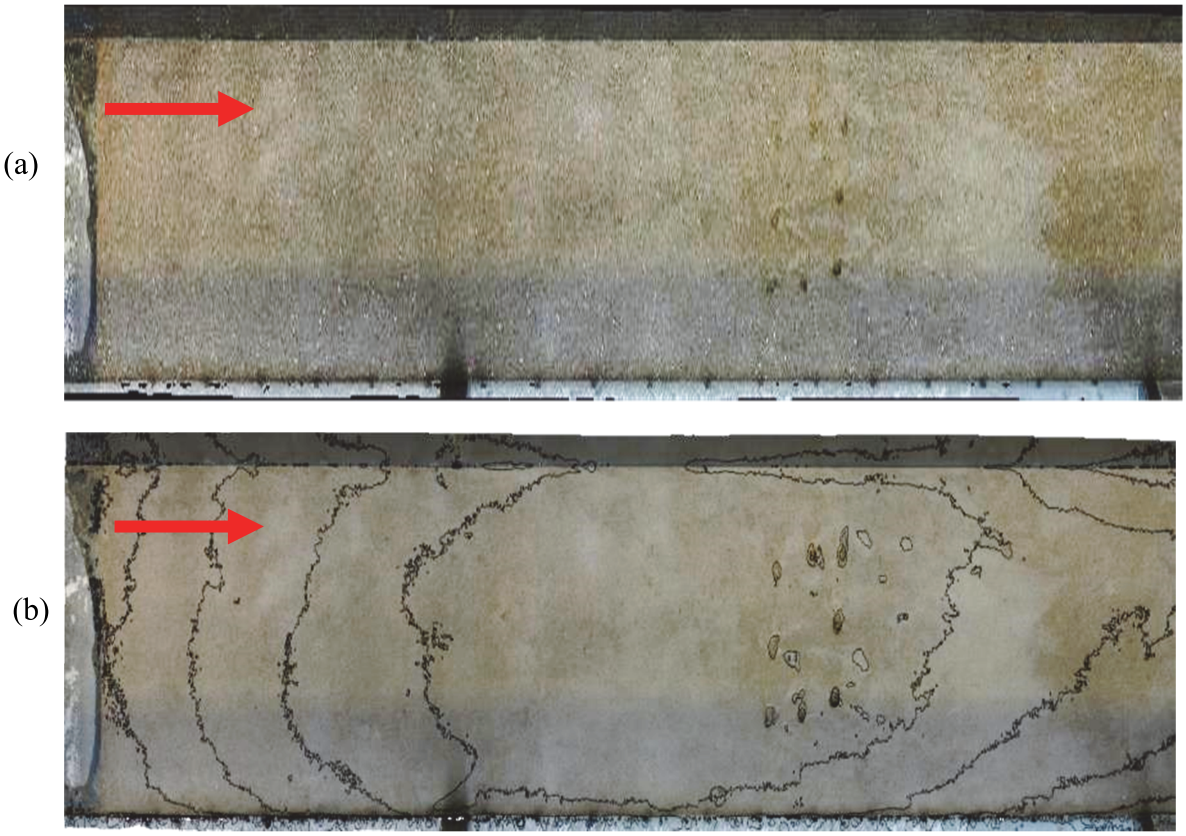

Figure 4.42: Reconstructed digital orthomosaic model from test 6: without (a) and with contour lines (b). Red arrow indicates direction of water flow.

4.4.7 Test 7

Through stitching together, the individual photos taken after the completion of test 7, the following images were recreated, Figure 4.43. A reconstructed digital model, as seen from the top and side, show the erosion and scouring patterns from the test.

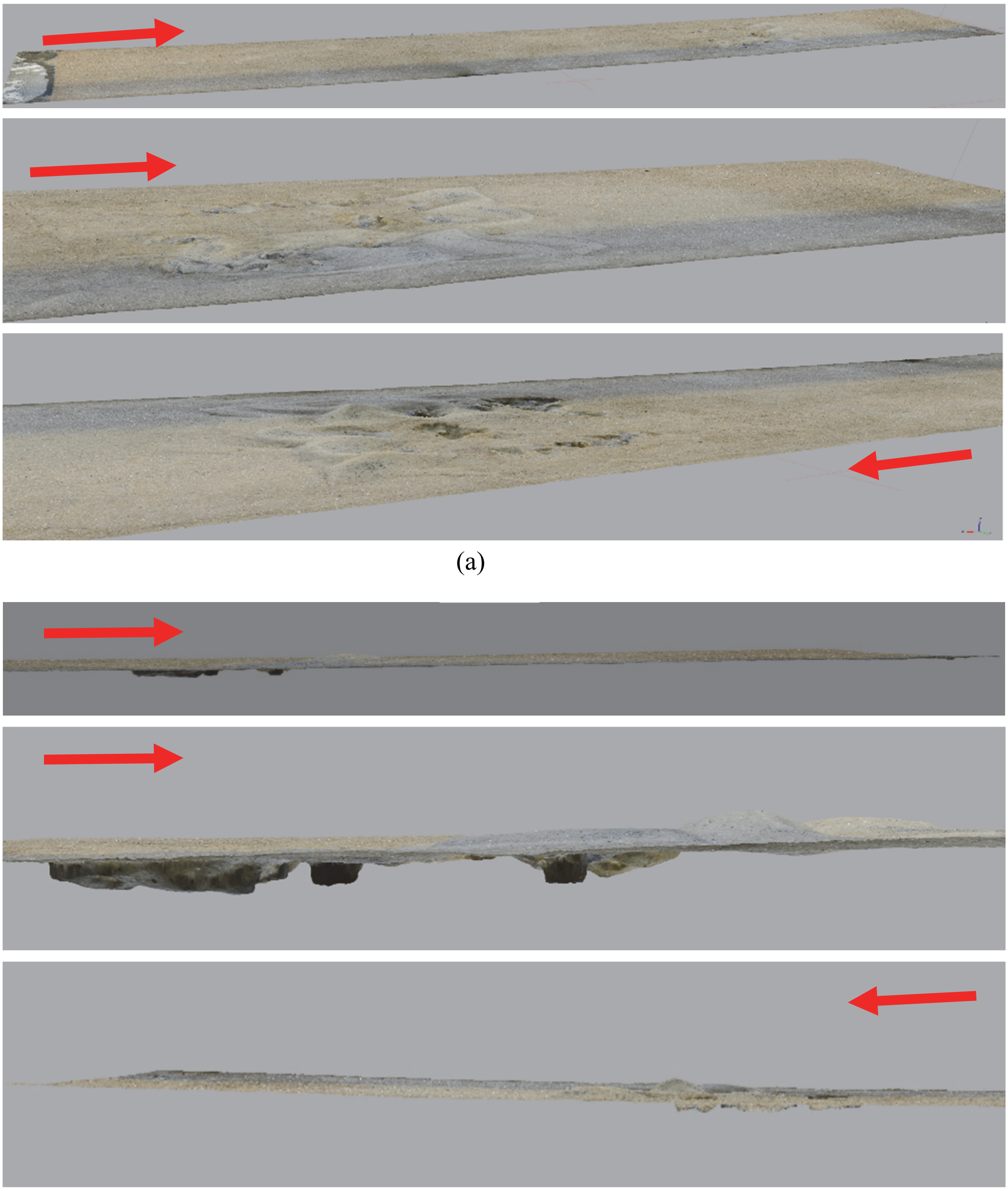

(a)

(b)

Figure 4.43: Reconstructed digital 3D model from test 7: perspective (a) and side view (b). Red arrow indicates direction of water flow.

Reconstructed digital elevation maps were then generated out of this 3D model, Figure 4.44. For test 2, the elevation varied between - 0.015 and 0.062 m. Contour lines were added to images b and c at a space of 0.002 m. Figure 4.44c shows the track line for depth measurements taken. In these maps, negative values indicate areas of erosion and positive values indicate areas of accretion. These values can be found in the Appendix, Figure 6.

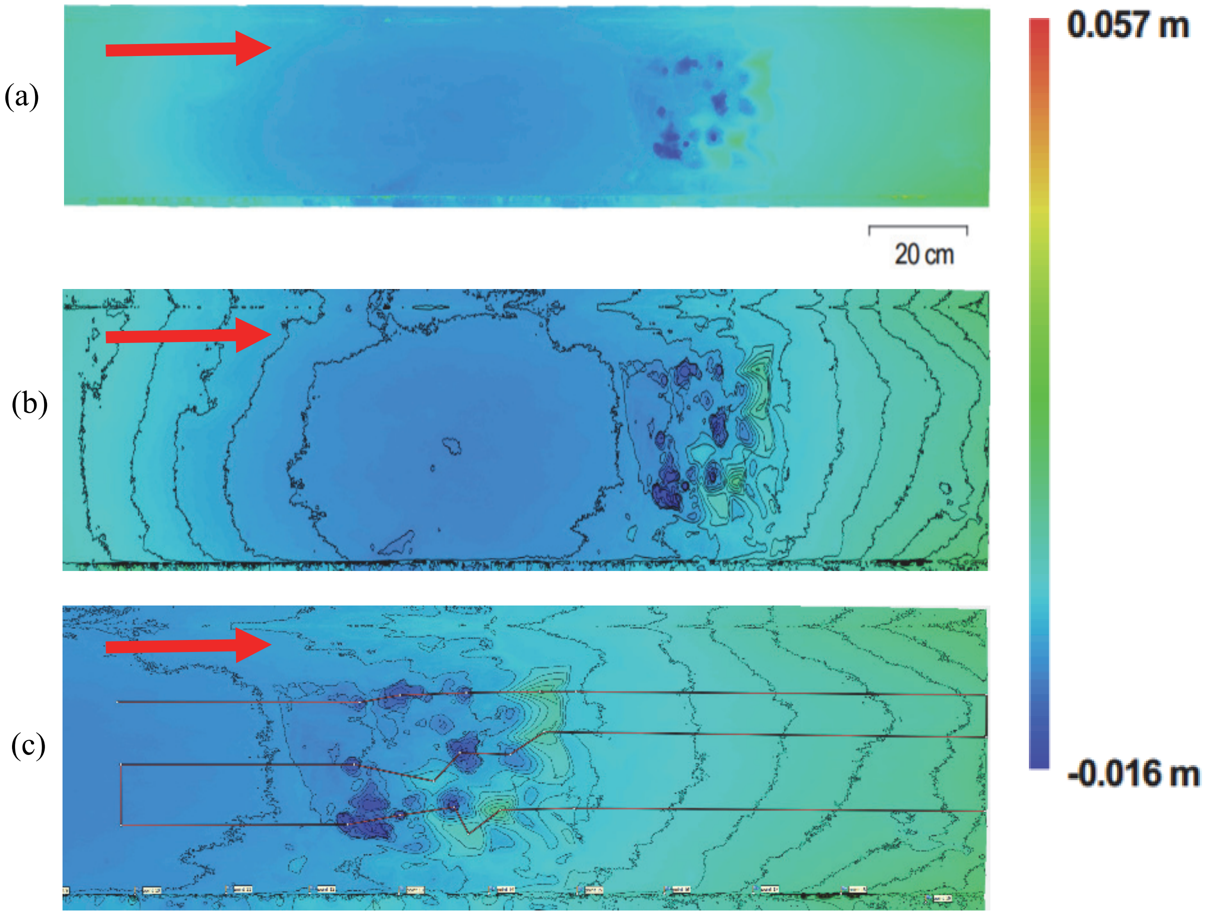

Figure 4.44: Reconstructed digital elevation model from test 7: without (a) and with contour lines (b, c). Red arrow indicates direction of water flow.

The reconstructed digital elevation model was then overlaid on the orthogonal image to create the digital orthomosaic model, Figure 4.45.

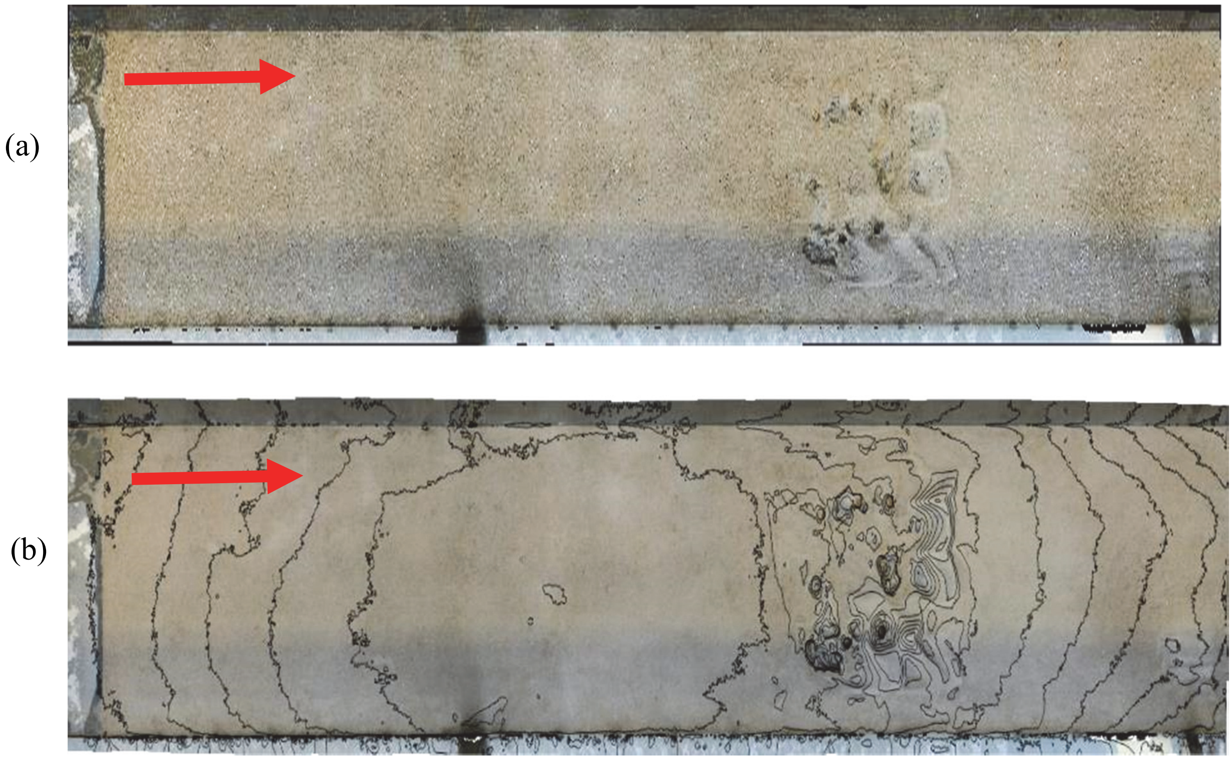

Figure 4.45: Reconstructed digital orthomosaic model from test 7: without (a) and with contour lines (b). Red arrow indicates direction of water flow.

4.4.8 Test 8

Through stitching together, the individual photos taken after the completion of test 8, the following images were recreated, Figure 4.46. A reconstructed digital model, as seen from the top and side, show the erosion and scouring patterns from the test.

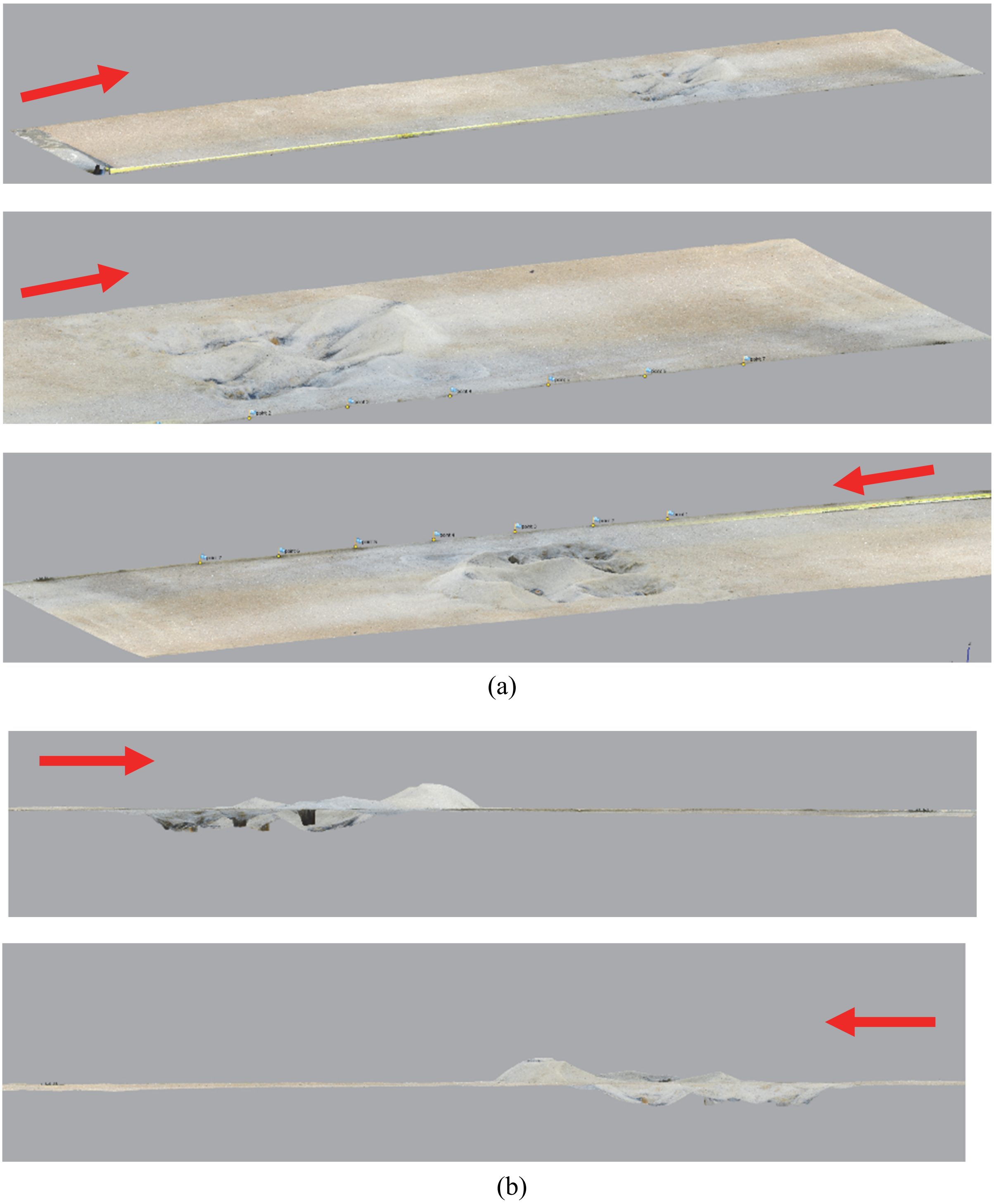

Figure 4.46: Reconstructed digital 3D model from test 8: perspective (a) and side view (b). Red arrow indicates direction of water flow.

Reconstructed digital elevation maps were then generated out of this 3D model, Figure 4.47. For test 2, the elevation varied between - 0.021 and 0.058 m. Contour lines were added if images b and c at a space of 0.002 m. Figure 4.47c shows the track line for depth measurements taken. In these maps, negative values indicate areas of erosion and positive values indicate areas of accretion. These values can be found in the Appendix, Figure 7.

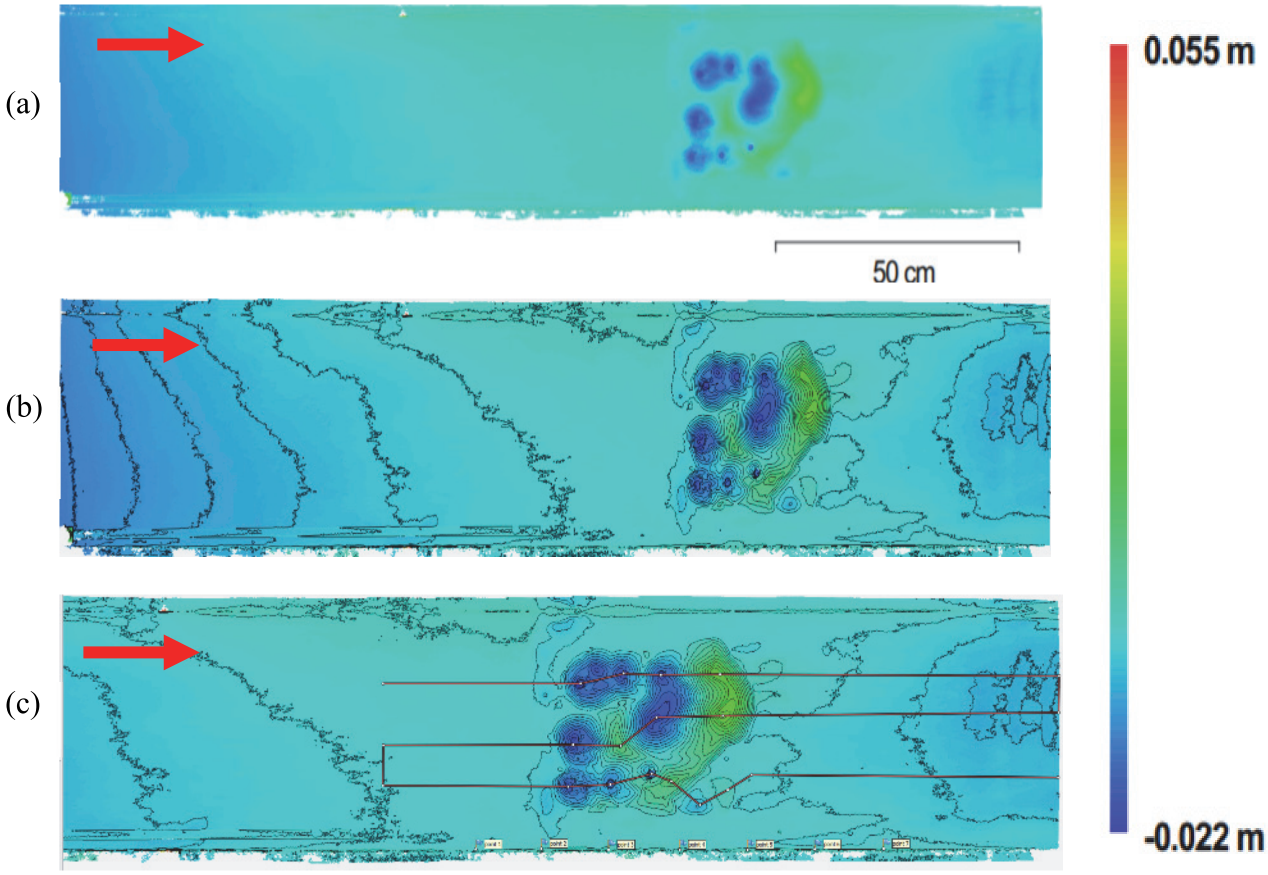

Figure 4.47: Reconstructed digital elevation model from test 8: without (a) and with contour lines (b, c). Red arrow indicates direction of water flow.

The reconstructed digital elevation model was then overlaid on the orthogonal image to create the digital orthomosaic model, Figure 4.48.

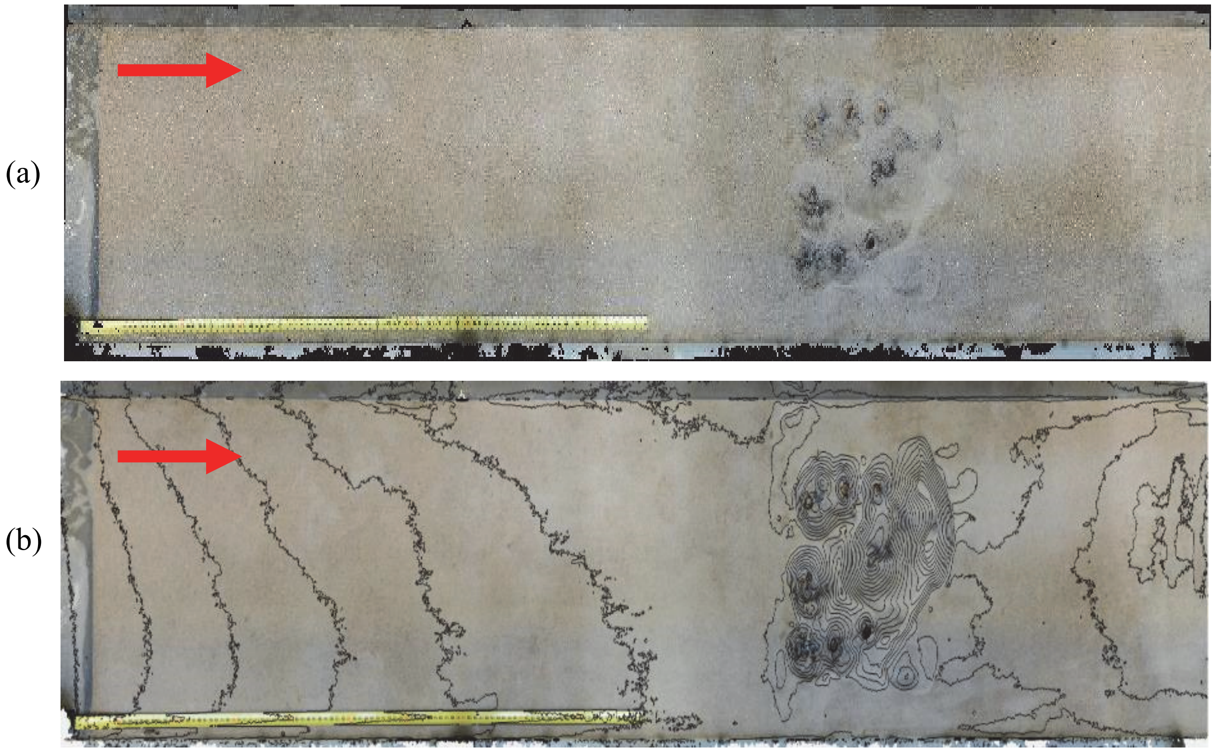

Figure 4.48: Reconstructed digital orthomosaic model from test 8: without (a) and with contour lines (b). Red arrow indicates direction of water flow.

5. Discussion

5.1 Testing Set up

Mimicking a real-world environment is very difficult in a laboratory space. Although many measures were taken in this experiment to duplicate the environment off the coast of Esposende, there were a few parameters which could have been improved or may have negatively impacted the results. This section will carefully walk through the testing set up to discuss the ways in which the facilities may have affected the results.

The testing hydraulic chamber, although large, still created boundaries closer to the PMAR than would naturally occur. The proximity of the walls may have affected the scouring and erosion patterns witnessed. Testing in a larger hydraulic chamber could be benefitioal to remove most of these possible effects and give a more realistic representation of scouring/erosion patterns.

Ideally, the grain size used during testing would be carefully selected to reflect the natural grain size associated with the area of installation. The grain size should be scaled to match the ratio of the MAR to PMAR, however this was not possible in this case. The size ratio between the MAR/PMAR is 20:1, and if an average grain size diameter off the coast of Esposende is assumed to be 0.3 mm then for testing a sand of 0.01 mm should be used (Li et al., 2009). According to the Wentworth scale, sediment with a diameter of 0.01 mm is classified as medium silt, and would have affected the transportation and settlement properties of the sediment (Wentworth, 1922). Interparticle interactions for sediment of this size would no longer represent the naturally occurring interactions for the Esposende area, and could consequently influence the results. Therefore, a sand with mean diameter of 0.328 mm was selected and used during testing. As in any experiment, there will always be a compromise. The experiment should be designed to maximize understanding of the general mechanisms which can be used to optimize the reef design given certain hydrodynamic requirements. Eventually this data will serve to calibrate numerical models which can then be extrapolated to real scale and real environments.

Equipment limitations meant that the complete vertical profile could not be collected. The area between the transducers and the measurement volume for this ADV was about 10 cm. This area served as a blind zone, where no data could be collected. In the future, if additional data is needed, either a deeper tank would be needed or a different ADV could be used to try to minimize this blind zone. In the case of this study, adequate data was collected, therefore the blind zone did not inhibit the analysis of the results. Additionally, further consideration concerning the frequency of acquisition of the ADV data may be required. In some instances, the process which is being studied, such as turbulence, is faster than the frequency of acquisition. In these cases, the measurements may be averaged or smoothed and may not accurately represent the real results.

Another potential issue from testing was that there were inconsistent sand conditions between each of the tests. The hydraulic chamber had a small valve which could be opened or closed, allowing the water to drain from the testing structure once the tests had been completed. The saturation levels of the sand affected the subsequent profiles taken during the photogrammetric surveys. In cases where the release valve was not opened, and the test area was left in water overnight, there was a negative impact on the erosion and scouring profiles. In cases of partial sand saturation, the sand seemed to settle back into a previous state, negating some of the results from testing. In cases where the sandbox was fully drained, sand remained in position overnight and could easily be photographed the next morning. In future studies, it is highly recommended to drain the sandbox prior to leaving the lab to ensure results are not altered overnight.

Two different wave generating mechanisms were used throughout testing. The first machine was only capable of producing small waves. This machine was switched out for a larger machine which was able to produce waves of desired height. Since these machines were being developed and optimized during testing, the first few tests experienced some variability in the waves. These issues were resolved such that, the final experiment of each of the eight tests was made with consistent waves. It is important to note that with lab testing, there will always be an element of compromise, such that real conditions can never be fully reproduced. The importance of lab testing is in the ability to study certain aspects that would be otherwise impossible to study in the field. In this way, a particular effect can be replicated allowing large amount of data to be collected and studied.

5.2 Data Analysis

The data collected can be categorized into 5 different scenarios based on the water conditions, the presence of the PMAR, the position of the ADV and the type of profile taken (vertical versus horizontal). For each scenario, two different flow states were used: constant flow, and constant flow with waves. In following section, each of these 5 scenarios will be thoroughly analyzed and discussed. It should be noted, that when referring to depth, measurements were taken from the sandy bottom upwards. Therefore, a depth of 5 cm represents a position 5 cm above the sandy bottom.

5.2.1 Scenario 1: Vertical Profile, Constant flow, no PMAR, position 9

In the case of constant flow, no waves and no PMAR from position 9, there were no significant fluctuations in velocities within the water column. There was a slight decrease in all velocities right before the bottom, which is expected due to the loss of energy due to friction with the sand. Velocities in the y- and z-direction were much lower (near 0) than when compared with the x- direction (~18 cm/s). Statistically speaking, the x- and z-direction data had a very low coefficient of variation (close to 0) when compared to the y-direction which had variations varying from 75% - 230% in VPA032 and 60% - 390% in VPA041. In the same case, but with the addition of waves, there was not much variation within the water column between 5 cm and 11 cm. Velocities were slightly less than in the case where waves were not present, due to energy lost due to interferences between waves. In test VPA058, below 5 cm, all flow directions experienced a significant decrease in flow velocities. This is likely due to the water's interaction with the sandy bottom. The coefficient of variation in the x- and z-directions were low, ~30% for VPA049 and ~0 for VPA058. The coefficient of variation in the y-direction was much higher, ranging from 140-230% in VPA049 and between 50-1500% for VPA058. According to the beam check conducted previously, data cannot be reliability collected within 4 cm of the bottom, therefore, the measurements at 5 cm were possible, are not reliable. Therefore, although it would be interesting to measure flow velocities in this region to estimate the limit layer of flow, with this particular equipment and testing conditions, it is not possible. These results were included to illustrate the limitations between the equipment sampling point and the boundary (sandy bottom).

To compare the results from the same position when waves are and are not present give us an idea of how the flow of water is interacting with the testing facility without the PMAR installed. When water reached a constant flow rate, velocities in all directions were maintained up and down the water column. Once waves had been introduced, these velocities experienced slight fluctuations in all directions, however, the largest change was in the y-direction near the bottom of the tank. Due to the non-symmetric geometry of the reef, and the interaction of the flow with the side walls of the flume, some transient effects may have been generated by the reef structure, which could be responsible for the variances observed. These results are not conclusive since the complete description of these processes would require higher acquisition frequencies.

5.2.2 Scenario 2: Vertical Profile, Constant flow, no PMAR, position 17

For the case of constant flow and no wave action, it was found that flow velocity did not show any drastic changes in any of the flow directions. In most cases, there was a slight decrease closer to the bottom, which correlates to the area where the coefficient of variation was relatively high due to unknown oscillations in the time series, especially in the y-direction (~300% in both cases). This is possibly due to the fact that the equipment lost accuracy once it reaches its boundary distance limit of 4 cm. However, the fact that the y-direction is experiencing much greater variance in a consistent manner may suggest that transient effects were occurring. For a more accurate description, higher acquisition frequencies would have been necessary.

When waves were present, two different cases were witnessed. Case 1, relates to tests VPA036 and VPA048, the flow velocities in all directions were fairly consistent at all depths. For both of these tests, the coefficient of variation for x- and z-directions were much smaller than when compared to y-direction. The coefficient of variation for x- and z-direction were consistent throughout the water column, at about 50%. The coefficient of variation for ydirection, on the other hand, fluctuated between 100 to 400% for VPA030 and 100 to 230% for VPA048 and VPA057. This large variance could have been a result of turbulence caused by the waves interacting with the sides of the test chamber. The results for VPA057 had slightly higher coefficient of variations when compared to the other two tests. This could have been a result of bad record quality. Additionally, during this test, the water circulating contained excess air bubbles, possibly due to temporary accumulation of air in the hydraulic pump, which accumulated quickly in the ADV acoustic sensors. This could have caused interference in the measurements. Although this only happened a few times, it may help to understand some of these outliers. Alternative measurement procedures may need to be introduced to minimize the possibility of this occurring again.

To compare the results from the same position when waves were and were not present illustrates how the flow of water interacted with the testing facility without the PMAR installed. When water had reached a constant flow rate, velocities in all directions were maintained up and down the water column. Once waves had been introduced, these velocities experienced slight fluctuations in all directions, however, the largest change was in the y-direction near the bottom of the tank. This is most likely due to its interaction with the sandy bottom.

There were no significant differences in velocities between position 17 and 9. This was an expected result as there is nothing to interfere with the water flow, except the boundary conditions. However, this allowed to confirm that transition ramp and sand bottom apparatus were not significantly disturbing the testing flow conditions. Once the PMAR is introduced, then we would expect to see changes between these two positions.

5.2.3 Scenario 3: Vertical Profile, Constant Flow, PMAR, Position 9

This scenario measured the vertical flow velocities from upstream of the PMAR. These results will provide a means of comparison with the flow velocities from downstream of the PMAR to measure the impact of the PMAR on water flow.

In the case of constant flow, without waves, x- and z-direction velocities were fairly consistent throughout the water column. The only exception to this was in test VPA071, where there was a change in x-direction flow velocities from 18 to 5 cm/s between the depths of 5 and 4 cm, which is reaching the technical limits of the ADV. All three tests experienced zdirectional flow velocities between 0 and 1 cm/s across all depths with the exception of test VPA071, which experienced negative velocities below 5 cm. These changes in the x- and zdirections, between 5 and 4 cm were not seen in the other two tests with similar parameters, therefore, this was likely the result of an unknown error and not a meaningful result to be analyzed.

The y-directional flow velocities varied between the three tests. In VPA034, there was a steady increase in velocities as distance from the bottom decreased. At a depth of 12 cm, the flow velocity was about 0.2 cm/s, whereas at 4 cm it was approaching velocities of 2.6 cm/s. In VPA045, the y-direction flow velocity maintained a fairly constant speed throughout the water column of just about 1 cm/s. Finally, VPA071 experienced a slight increase in velocities from 13 to 11 cm depth (from 0.4 to 1.1 cm/s) and then plateaued between 11 cm and 5 cm around 1.1 cm/s until finally decelerating again between 5 and 4 cm to a final velocity near 0. The differences in these three tests make it very difficult to analyze trends in flow velocities in the y-direction. The coefficient of variation for these tests were also very high in the y-direction. The coefficient of variation for test VPA045 was about 50% across all depths until reaching 5 cm depth where the coefficient of variation increased to 250% until the final measurement at 4 cm. For VPA071 the coefficient of variation was even higher between 5 and 4 cm reaching a maximum value of nearly 4000%. Due to the high coefficient of variations in this data, the y-direction flow velocities are statistically insignificant for this study and could not be analyzed. These results are influenced by fact the test is reaching the distance limit from the boundary. The higher variance for y may be a good indication of transient processes that the experimental approach does not accurately describe. This is likely considering both the non-symmetrical geometry of the reef and the interference caused by the side walls of the flume which are perhaps too close to the reef.

Next, waves were added to see the effects of a high energy environment. The results were very similar to the no wave environment, however overall velocities were slightly decreased. This decrease in overall velocities was likely the result of energy loss due to wave interactions. For example, in the case of no waves present, the x-directional flow velocities were around 18 cm/s, whereas, once the waves were added, this speed dropped to closer to 17 cm/s. The overall trends in the data were maintained, however. Velocities in all directions were fairly consistent along the water column, with a x-directional flow velocity around 17 cm/s, z-directional flow velocities very close to 0, and a y-directional flow near 1 cm/s for both tests. Again, there was an anomaly in the second test, VPA065, between the depths of 5 and 4 cm where the flow velocities in all directions rapidly decreased. This correlates to an area with high coefficients of variation, ranging from 0-150% in the x-direction and -180-100% in the ydirection. Furthermore, y-direction coefficient of variation in both tests ranged between 100180% across the entire water column, so this data might not be statistically significant.

5.2.4 Scenario 4: Vertical Profile, Constant Flow, PMAR, position 17

In this next scenario, measurements were taken from behind the PMAR, which revealed the impact of the PMAR on flow directions velocities. The obtained results suggest that flow velocity decreases with decreasing distance to the bottom due to the presence of the PMAR. In each of the three tests, flow velocities in the x-direction decreased with depth, with the largest change in velocity happening within between 12 and 8 cm depth. The y-direction in tests VPA044 and VPA070 decreased at first but returned to its previous value or gained velocity near the bottom. In the case of VPA070, the velocity at 11 cm depth was 1 cm/s whereas it was almost 2.5 cm/s at 4 cm. The coefficient of variations for y-direction values were very high, ranging from 100- 500%, making the y-directional data statistically insignificant. Velocities in the z-direction experienced negative values at the lowest depths, likely the result of turbulence created by the presence of the PMAR. It is interesting to note that in the presence of the PMAR, this is the only case where the z-direction flow surpasses ydirection flow in value. This is a good indication of turbulence resulting from the interaction of the PMAR and the water flow direction.

Similar trends were found in the data once waves were introduced. It should be noted, however, that the coefficients of variance for all directions for test VPA065 were very high below 5 cm depth, suggesting the turbulent nature of this water may be difficult to analyze statistically. Flow velocities in the y-direction also had high coefficient of variation. For VPA051, the coefficient of variation was the highest between 10 and 8 cm depth, where it ranged from 200-1300%. For VPA065, the y-direction also experienced very high coefficients of variation, however this was between the depths of 7 and 4 cm, and ranged from (-130 - 250%).

When comparing the results between the scenarios with and without waves, it was seen that without waves, velocities in all directions were much higher after the PMAR. When considering velocities in the x-direction, without waves the velocities are much higher at shallower depths and then decrease at a faster rate than in the scenario with waves. For example, in VPA070, at a depth of 11 cm the x-direction velocity was 17 cm/s. This velocity steadily decreases in the presence of the PMAR until reaching a minimum flow velocity of 11 cm/s at the depth of 4 cm. This trend can be seen in the other two tests as well.

When comparing the results from before and after the placement of the PMAR it could be seen that the presence of the PMAR adds significant turbulence to the water which affected the flow velocities in all directions. This turbulence added to the scouring and erosion patterns generated by the presence of the PMAR. Turbulence increased along the length of the PMAR which increased erosion and scouring along the backside of the PMAR (away from the direction of flow).

5.2.5 Scenario 5: Horizontal Flow Velocity Profile

The next scenario measured the horizontal flow velocities from location 9 heading downstream. Measurements were taken over a length of 75 cm from a depth of 10 cm from the bottom. In these tests, steady flow was used without the addition of waves. These measurements were taken during two tests, VPA062 and VPA069.

In both cases, x-directional velocities decreased as distance from point 9 increased. Therefore, the effect seems real, but was not possible to fully document, possibly due to low acquisition frequencies. In the case of VPA062, this decreased from about 15 cm/s to 5 cm/s whereas in test VPA069, the change in velocities was much smaller, from about 11 cm/s to 8 cm/s. This decrease in velocity is likely the result of energy loss due to friction along the sandy bottom and interaction with the sides of the tank. The coefficients of variation for both tests was very low in the x-direction, meaning this data is statistically significant and could be used in the analysis.

Similarly, y-direction flow velocities showed overall decreasing speeds with an increase in distance from point 9. VPA062 showed greater overall speeds, with y-direction flow velocities decreasing from 3 - 2 cm/s, whereas, VPA069 showed a decrease from 1 - 0 cm/s. Note that the decrease in both cases was around 1 cm/s over the length of the test. For both tests, data collected between 0 and 65 cm for VPA062 and between 0 and 50 cm for VPA069 had very low coefficients of variation. However, after these points, the coefficients of variances became much higher, making the data from the far end of the testing area less statistically significant for analysis.

Z-direction flow velocities showed slightly increasing velocities over distance, the opposite of what was seen in the x- and y- directions. For both tests, the z-direction velocity started off around 0 and slowly increased to around 1 cm/s, hitting a maximum value between 50 and 60 cm from position 9. This increase in velocity could be the result of constructive interference between the walls and sandy bottom adding to an overall increase in energy in the z- direction. The coefficients of variation for both tests was very low in the z-direction, meaning this data is statistically significant and could be used in the analysis.

5.3 Photogrammetric Surveys

During the photogrammetric surveys, each photo was taken by hand. After the first test, a railing system was introduced to allow the camera to be moved across the top of the testing chamber. For the first test, this railing was not used, and an inadequate number of photos were taken after testing. Due to this, it was not possible to recreate the digital elevation model, which is why this portion is missing from the results section.

Slight variations in placement and angles of the camera equipment can contribute to noise in the digital models. This noise could be minimized if the camera position was fixed throughout testing. All efforts were made to minimize these variations, but as with anything done manually, it is possible these errors occurred. Although each of the models created had resolution of less than one millimeter, it could be possible in the future to continue to improve these techniques to minimize noise in the final models.

From comparing each of these Digital Elevation Models, the results of leaving the valve closed overnight and allowing the sand to remain fully saturated, can be seen. Test 5 is an example with minimal sediment transportation around the PMAR. The formation of the dunes typically resulting from deposition of sediments downstream of the structure cannot be verified. This is because the sand was too saturated and was not able to maintain its structure. Similar results were seen in Test 6 and 7, but not in Test 8 where the valve was open and the sand was able to become dryer overnight. In Test 8, the final dune structures could clearly be seen, even when photographed the next day.

From these models, although slight variations exist between them all, one overall trend was quite clear. There is significantly more erosion and scouring near the downstream portion of the PMAR. Overall, sediment is transported from the front of the PMAR and deposited downstream, slowly rotating the PMAR in the direction of the waves. This creates two concerns when installing this PMAR. First, is whether an excessive amount of sediment would be transported, causing the PMAR to sink enough to negate the beneficial effects of its installation. Second, the possibility of the PMAR overturning, potentially damaging the structure or flora/fauna surrounding it. One possible solution would be to use a similar concept as the 2015 Pukyong National University study and install a baseplate or geogrids on which the PMAR structure could be built (Ha et al, 2015). This would minimize or eliminate erosion and scouring from within the structure, and lessen the possibility of overturning.

Additionally, analyzing the Digital Elevation Models illustrates the effects of the waves when compared to the results without waves. Figure 5.1 represents the final results in cases with and without waves. As stated previous, in Tests 5, 6 and 7 the drain valve was closed, allowing the sand to remain fully saturated overnight which affected the fidelity of the sand structures, final results photographed were less than when the test was completed. Even with the sand leveling out due to saturation, test completed with waves experienced greatest amount of sand transportation. For this comparison, Test 1 was not included because a model could not be created, and Test 2 was removed because it used a smaller wave amplitude than the other three tests.

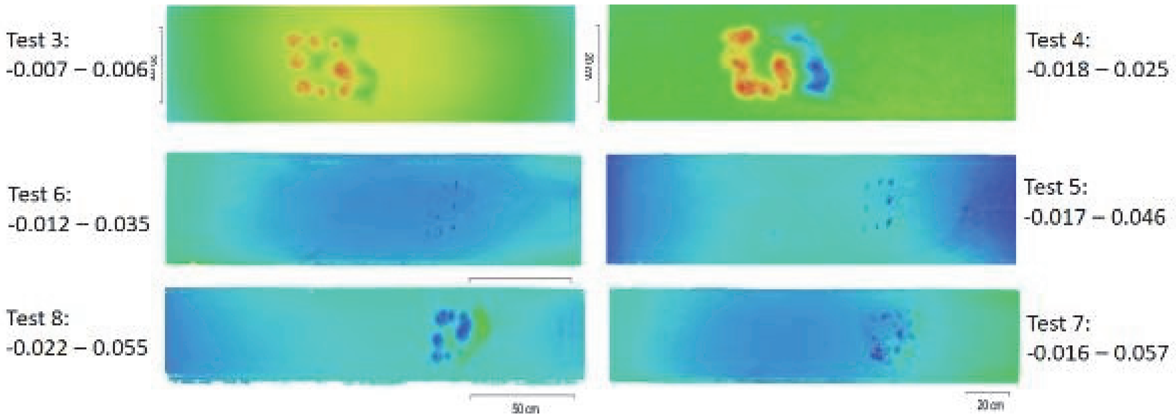

Figure 5.1: Comparison between final results of tests without (left) and with waves (right) present

Next, a comparison between the final results with the smaller wave amplitudes can be made against the tests with larger wave amplitudes. In Test 2, a wave amplitude of 2.8 cm was used and in Tests 4, 5 and 7 a wave amplitude of 6.3 cm was used. It has been demonstrated that increased wave amplitude generate more energy which translates to greater sand transportation within the system. In Test 2, the PMAR experienced significant sand erosion near the front of the structure and very little sand deposition within the testing area. In the tests with greater wave energy, Tests 4, 5 and 7, the testing area experienced far less erosion and much more sand deposition around the PMAR. Figure 5.2 represents the comparison between these tests.

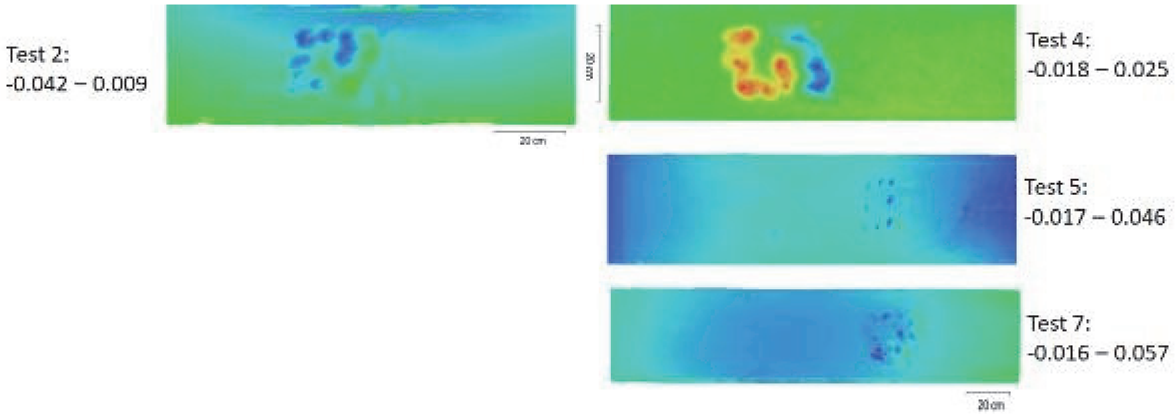

Figure 5.2: Comparison between final results of tests smaller wave amplitude (left) and larger wave amplitude (right)

In these tests, nearly all of the flow was coming along a single axis (x-direction). In a natural environment this will likely not be the case. Currents experienced by the MAR once installed could be coming from multiple directions varying in space and time. In areas which experience significant tidal changes, it is possible that the dominating direction of flow could vary by up to 180° within a tidal cycle. Therefore, it is important that the PMAR and MAR are constructed and tested such that it can withstand these currents from any direction.

6. Conclusions

Using an unconventional geometrical design, the PMAR was intended to generate unusual current patterns which would be beneficial for several habitat factors, such as water recirculation, which can positively influence organisms' interactions with the structure. Using a computationally driven design can be useful to optimize this and other aspects, besides the classical and traditional calibration of numerical models, or the quantification values such as: roughness effects or hydrodynamic drag forces.

Once the design was finalized, a scaled 3D printed prototype was manufactured, assembled and used for hydraulic flume testing. Throughout the testing, an ADV was used to quantify the vertical and horizontal water flow velocities both upstream and downstream from the PMAR. This allowed the interactions between the PMAR and water flow to quantified.

Photogrammetric surveys taken after completion of the tests allowed for detailed orthomosaic photos to be generated which aided in the analysis of overall sediment transportation. Ensuring sufficient quantity and quality of photos taken was critical in the fidelity of the final model generated. Furthermore, sand saturation levels upon completion of the test were critical in preserving the final results. When the sand remained saturated overnight, the sediment began to level out, decreasing the apparent erosion or deposition.

Tests which were conducted using constant flow experienced higher overall flow velocities in all directions. Tests which were conducted using constant flow and waves experienced an increase in energy which led to a decrease in velocities and an increase in sand transportation. In every case, the PMAR experienced sand erosion around the front of the structure and sand deposition near the back end of the structure. This led to a slight sinking of the PMAR within the sand with a slight rotation in the direction of flow. It would be of interest to repeat these procedures with a structural addition, which could minimize these effects, such as a geogrid or bottom plate.

When the full-sized MAR is installed off the coast, an analysis of typical wave velocities must be conducted to ensure MAR will not either sink too deep or topple over in high energy conditions. Furthermore, actual physical parameters of the area of installation should be used during testing to verify structural stability of the design is maintained.

7. Future Work

One way to mitigate the sinking of the PMAR and stabilize it against overturning would be to add a baseplate. This baseplate could help redistribute the load stresses and increase the stability of the PMAR in high energy environments. Additionally, the presence of a baseplate would not eliminate the erosion or deposition of sediments, but could help keep the PMAR level. This would become increasingly important as additional modules are added to the PMAR, increasing its height.

Implementing a sophisticated structural health monitoring (SHM) system would help maintain confidence in the structural integrity of the design after implementation. This SHM technology is currently deployed on a variety of semi-submersible platforms such as wind farms and oil platforms. Complications are introduced once this system is installed aboard fully submerged systems. Once the system is fully submerged, functions such as GPS positioning and leak detection are no longer applicable. Solving these issues will become a major initiative to be included on the SHM of the MAR (Maslov et al, 2018). There are many factors which will need to be considered, which include, but are not limited to, surface ocean waves, currents, tidal movement, shore erosion, and vortex-induced vibrations. To conduct monitoring a combination of Natural Frequency Response Monitoring (NFRM) and strain monitoring approaches could be used (Pereira et al, 2017). To implement the NFRM monitoring, a multi-axial accelerometer could be used to measure the response of these various periodic and constant environmental fluctuations as it impacts the structure as a whole. Furthermore, by installing strain transducers on the MAR, additional monitoring can be conducted at critical points along the structure's frame (Pereira et al, 2017).

Under the OMARE project, the Littoral North Natural Park will be extensively characterized. Through this project, detailed bathymetry, mapping of habitats, identification of the location of human activities, and the measurement of physical variables (such as temperature, salinity and chlorophyll concentrations) will be compiled. This information will feed a database system that is intended to allow the mapping of the area according to the European Union Nature Information System (EUNIS). With this information, a decision framework concerning the optimal geometry, materials, and placement position used for the construction and installation of the MAR should ideally consider all the information previously mentioned. Using a geospatial approach, the decision process could be aided by building models which use several layers of information simultaneously. This model would identify potential areas which serve as the best area for installation. In this context, geostatistics is a very appealing approach to deal with all the information that will be collected, as well as, to serve as a solid support to the decision models to be developed.

Furthermore, once these physical parameters are understood, additional testing could be conducted to model the PMAR with more realistic environmental conditions. The MAR is intended to consist of multiple units linked together. Further testing which includes multiple units could provide important insight into how the MAR will perform once completed. Issues concerning how the MAR are linked, or twisting forces which may occur between units must be carefully considered and tested prior to deployment.

8. References

Bianchimani, O. 2017. “Artificial Reefs.” Artificial Reef REXCOR in Marseilles, CNRS LSIS, Images & Models Team, www.lsis.org/groplan/article/art_Cortiou.html.

Bicudo, P. and Horta, A., 2009. Integrating Surfing in the Socio-economic and Morphology and Coastal Dynamic Impacts of the Environmental Evaluation of Coastal Projects. Journal of Coastal Research, SI 56 (Proceedings of the 10th International Coastal Symposium), pg – pg. Lisbon, Portugal, ISBN

Bohnsack, J.A., 1989. “Are high densities of fishes at artificial reefs the result of habitat limitation or behavioral preference?” Bulletin of Marine Science. 44, 631–45.

Bohnsack, J.A., Harper, D.E., McClellan, D.B., Hulsbeck, M., 1994. “Effects of reef size on colonization and assemblage structure of fishes at artificial reefs off southeastern Florida, USA.” Bulletin of Marine Science. 55, 796–823.

Chabert, J., Engeldinger, P. 1956. “Study of scour around bridge piers. Laboratoire National d'Hydraulique 6”. Quai Watier, Chatou, France.

Wentworth, C. K. 1922. "A Scale of Grade and Class Terms for Clastic Sediments," The Journal of Geology 30, no. 5, 377-392.

Cresson, P, Ruitton, S., Harmelin-Vivien, M. 2014. “Artificial Reefs Do Increase Secondary Biomass Production: Mechanisms Evidenced by Stable Isotopes.” Marine Ecology Progress Series, vol. 509, Aug. 2014, pp. 15– 26., doi:10.3354/meps10866.

Dezen-Kempter, E., Soibelman, L., Chen, M., and Müller Filho, A. V. 2015. “Escaneamento 3d a laser, fotogrametria e modelagem da informação da construção para gestão e operação de edificações históricas.” Gestão & Tecnologia de Projectos, 10(2):113–124.

Dimmock K. 2009. “Comfort in adventure: the role of comfort and negotiation in recreational scuba diving”. Doctor of Philosophy, Southern Cross University, Lismore, NSW.

EEA. 2018. “Welcome to EUNIS, the European Nature Information System.” EUNIS Welcome to EUNIS Database, European Environmental Agency. eunis.eea.europa.eu/index.jsp.

Fabi, G., Scarcella, G., Spagnolo, A., Bortone, S.A., Charbonnel, E., Goutayer, J. J., Haddad, N., Lök, A., and Trommelen, M. 2015. “Practical Guidelines for the use of Artificial Reefs in the Mediterranean and the Black Sea.” General Fisheries Commission for the Mediterranean. No. 96. Rome, FAO 2015.

González-Rivero, M., Harborne, A.R., Herrera-Reveles, A., Bozec, Y.-M., Rogers, A., Friedman, A., Ganase, A., and Hoegh-Guldberg, O. 2017. “Linking Fishes to Multiple Metrics of Coral Reef Structural Complexity Using Three-Dimensional Technology.” Scientific Reports, vol. 7, 25 Oct. 2017, doi:10.1038/s41598-017-14272-5.

Granja, H. M., Pinho, J. L. S., Silva, A. P. 2015. “Pebble beaches of NW portuguese coast: genesis and short-term morphodynamics”. VII Congresso Nacional de Geomorfologia, pp. 91-97, 978-989-96462-6-1, 2015 (Portuguese).

Geospatial Services. 2018. “Photogrammetry and Remote Sensing.” SBL Knowledge Services Ltd., 21 Feb. 2018, blog.sblcorp.com/photogrammetry-and-remote-sensing/.

Google Maps. 2017. “Map of the North Littoral Natural Park”. Retrieved December 2017.

Ha, Y. S., Yun, D. H., Singh Pradhan, A. M., Pradhan, B., and Kim, Y. T. 2015. “Study on the settlement reduction of artificial reef”. The 2015 World Congress on Advances of Structural Engineering and Mechanics. Incheon, Korea. August 25-29, 2015.

Harris, L.E., 2003. “Artificial reef structures for shoreline stabilization and habitat enhancement”. 3rd International Surfing Reef Symposium, ASR, Ltd., Raglan, New Zealand.

Harris, L. E. 2009. “Artificial Reefs for Ecosystem Restoration and Coastal Erosion Protection with Aquaculture and Recreational Amenities.” Reef Journal, vol. 1, no. 1, pp. 235–246.

Hawkins, J.P., Roberts, C.M., Kooistra, D., Buchan, K., White, S. 2005. “Sustainability of scuba diving tourism on coral reefs of Saba”. Coastal Management. 33, 373-387.

IPCC, 2014. “Climate Change 2014: Synthesis Report. Contribution of Working Groups I, II and III to the Fifth Assessment Report of the Intergovernmental Panel on Climate Change [Core Writing Team, R.K. Pachauri and L.A. Meyer (eds.)]”. IPCC, Geneva, Switzerland.

Jackson, L., Corbett, B., Tomlinson, R., McGrath, J. and Stuart, G. 2007. Narrowneck Reef: review of seven years of monitoring. Shore & Beach Vol. 75, No. 4, Fall 2007, 1-13.

Johnson-Sapp, K. 2018. “A Tale of Two Reefs: Quantifying the Complexity of Artificial Reefs and Natural Reefs Utilizing Structure-from-Motion 3D Modeling”. Duke University, 2018.

Kimura, H., Ingsrisawang, V. and Ban, M. 1994. “A Study on Local Scour of Cylindrical Artificial Fish Reefs. Fisheries Engineering”. Vol.31 No.1, pp.33-40, 1994

Kirkbride-Smith, A.E., Wheeler, P.M., Johnson, M.L. 2013. “The Relationship between Diver Experience Levels and Perceptions of Attractiveness of Artificial Reefs - Examination of a Potential Management Tool”. PLoS ONE 8(7): e68899. doi:10.1371/journal.pone.0068899

Li, B., Granja, H.M., Farrell, E.J., Ellis J.T., and Sherman, D.J., 2009. “Aeolian saltation at Esposende beach”. Journal of Coastal Symposium), 327-331. Lisbon, Portugal, ISSN 07490258.

Liu, H.S.; Ma, X. & Zhang, S.Y., et al. 2009. “Validation and comparison between wind tunnel experiments and numerical simulation of flow field around artificial reefs”. Vol.16, No.3, pp. 365-371

Liu, Y.; Dong, G.; Zhao, Y.; Guan, D. and Li , Y. 2011. “The Investigation of the Hydrodynamics of an Artificial Reef, Aquaculture and the Environment”. Barbara Sladonja, IntechOpen, DOI: 10.5772/30064.

Maslov, D, Pereira, E, Miranda, T, Valente, I, Cruz, F., Pinheiro, M. 2018. “Innovative monitoring strategies for multifunctional artificial reefs”. OCEAN Conference; 2018, October 22-25. Charleston, USA, 2018.

Mull, J. 2014. “Pipe Dreams and Artificial Reefs.” SURFER Magazine, SURFER Magazine, 27 June 2014, www.surfer.com/features/pipe-dreams-artificial-reef/.

NEXT-Sea. 2018. “Creating Tomorrow's Smart Coast”. NEXT-Sea, 2018, nextsea.org/.

NOAA. 2017. “Corals.” NOAA's National Ocean Service, 6 July 2017, oceanservice.noaa.gov/education/kits/corals/coral07_importance.html.

OMARE. 2018. “The Marine Observatory of Esposende.” OMARE, Municipality of Esposende, 2018, www.omare.pt/.

Pattiaratchi, C. “Sixth International Conference on Coastal and Port Engineering in Developing Countries.” *Performance of an Artificial Surfing Reef: Cable Station, Western Australia*, 2003.

Polak O., Shashar N. 2012. “Can a small artificial reef reduce diving pressure from a natural coral reef? Lessons learned from Eilat, Red Sea”. Ocean and Coastal Management. 55, 94-100.

Polovina J., Sakai I., 1989. “Impacts on Artificial Reefs on Fishery Production in Shimamaki Japan”. Bulletin of Marine Science, 44(2), 997-1003.

Reef Resilience Network. 2018. “Overfishing and Destructive Fishing Threats.” Reef Resilience, The Nature Conservancy, 26 Jan. 2018.

Richardson, E.V. and Davis, S.R. 2001. “Evaluating scour at bridges. 4th Edition, Federal Highway Administration Hydraulic Engineering Circular No. 18”, FHWA NHI 01-001.

SBL. 2016. “A Brief Introduction to Photogrammetry and Remote Sensing ~ GIS Lounge.” GIS Lounge, GIS Lounge, 19 Dec. 2016, www.gislounge.com/a-brief-introduction-tophotogrammetry-and-remote-sensing/

Sungthong, S., 1988. “Evaluation of artificial reef installed in Rayong, Thailand, 1978-1987. In: Report of the Workshop on Artificial Reefs Development and Management”, 13-18 September 1988, Penang, Malaysia. ASEAN, Manila, pp. 135-148.

Turismo de Portugal. 2018. “Bem Vindo Ao Turismo De Portugal.” *Turismo De Portugal*, Portugal 2020, Compete 2020, European Union, www.turismodeportugal.pt/pt/Paginas/homepage.aspx.

Visit Esposende. 2018. “Visit Esposende.” Esposende Municipality, www.visitesposende.com/en.

Yaakob, O, Ahmed, Y.M., Adnan, F.A., Kong Koh, K. 2016. "Hydrodynamic Design of New Type of Artificial Reefs", Applied Mechanics and Materials, Vol. 819, pp. 406-419.

Appendix

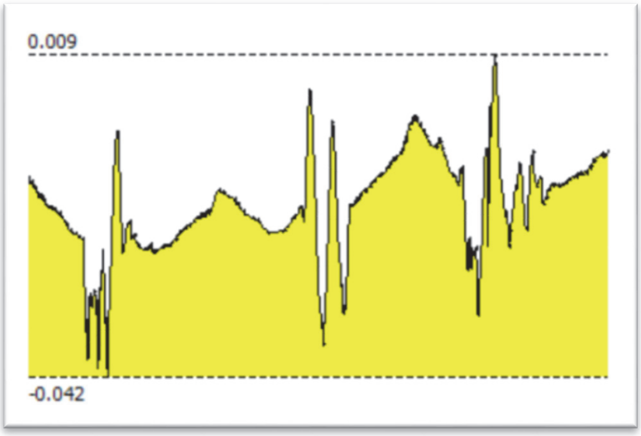

Figure 1: Reconstructed Digital Elevation Model depth data from Test 2

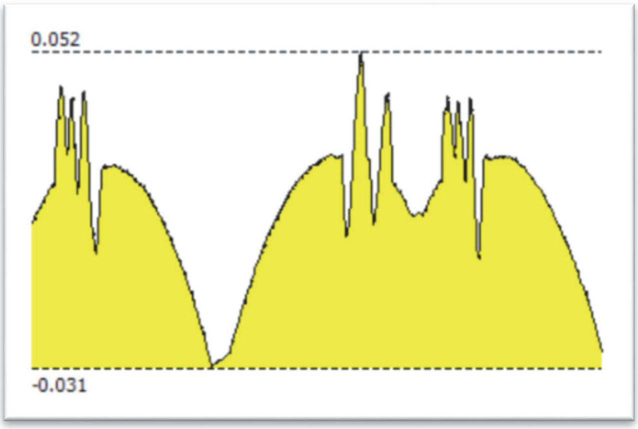

Figure 2: Reconstructed Digital Elevation Model depth data from Test 3

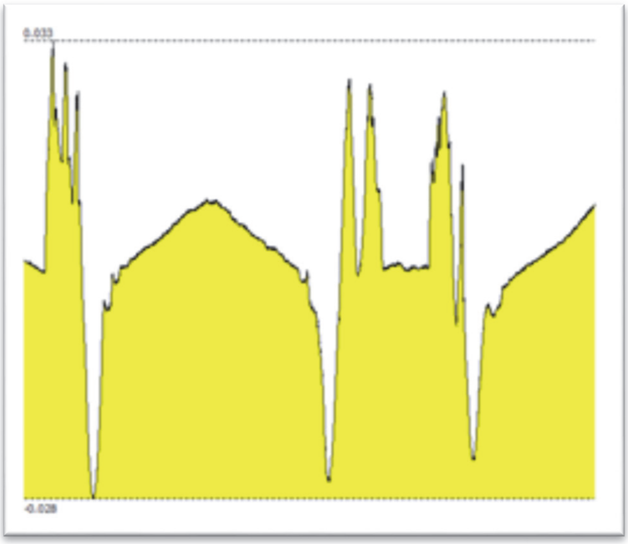

Figure 3: Reconstructed Digital Elevation Model depth data from Test 4

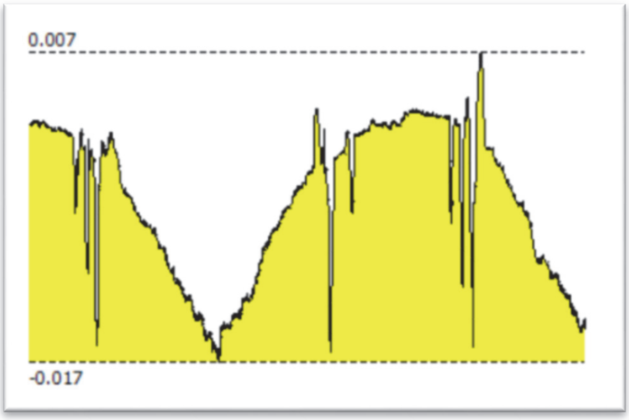

Figure 4: Reconstructed Digital Elevation Model depth data from Test 5

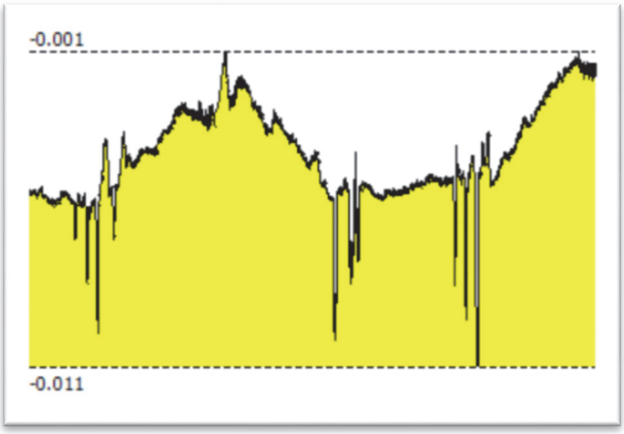

Figure 5: Reconstructed Digital Elevation Model depth data from Test 6

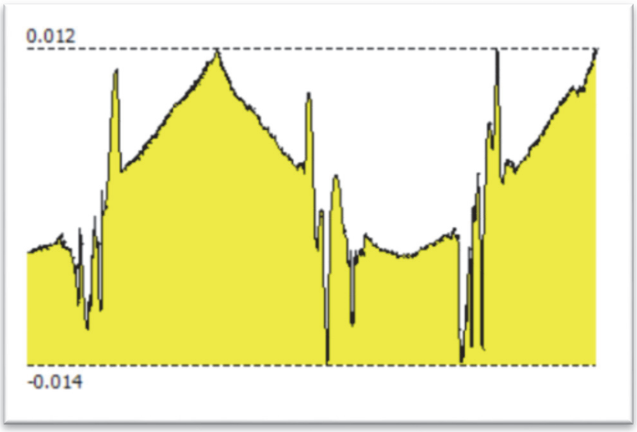

Figure 6: Reconstructed Digital Elevation Model depth data from Test 7

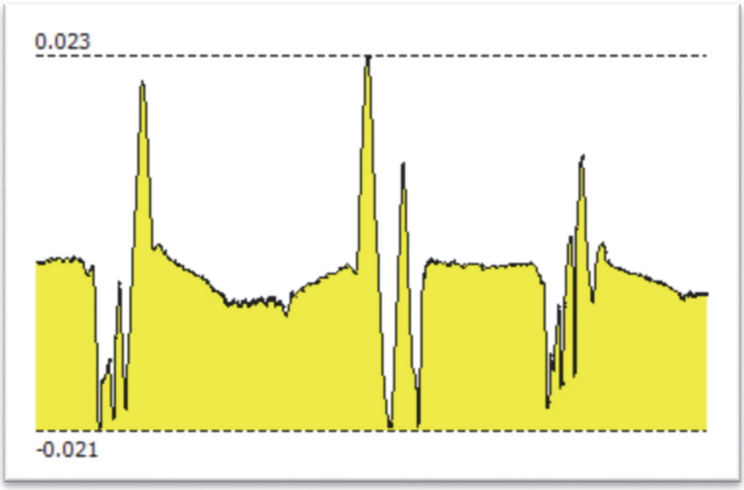

Figure 7: Reconstructed Digital Elevation Model depth data from Test 8